國立交通大學

電子物理研究所

博士論文

鐵—鎳—鎵合金材料的鐵磁共振與磁彈性質研究

Ferromagnetic resonance and magneto-elastic properties of (FeNi)$_{81}$Ga$_{19}$ alloys

研 究 生:劉奇青

指導教授:任盛源　教授

莊振益　教授

中華民國 102年 10月

鐵—鎳—鎵合金材料的鐵磁共振與磁彈性質研究

Ferromagnetic resonance and magneto-elastic properties of

$(FeNi)_{81}Ga_{19}$ alloys

研 究 生:劉奇青　　　　　　Student : Chi-Ching Liu

指導教授:任盛源　教授　　　Advisor: Shien-Uang Jen

　　　　　莊振益　教授　　　Advisor: Jenh-Yih Juang

國立交通大學

電子物理研究所

博士論文

A Dissertation
Submitted to Department of Electrophysics
College of Science
National Chiao-Tung University
in Partial Fulfillment of Requirements
for the Degree of Doctor of Philosophy
in
Electrophysics
October 2013
Hsinchu, Taiwan

中華民國 102年 10月

鐵─鎳─鎵合金材料的鐵磁共振與磁彈性質研究
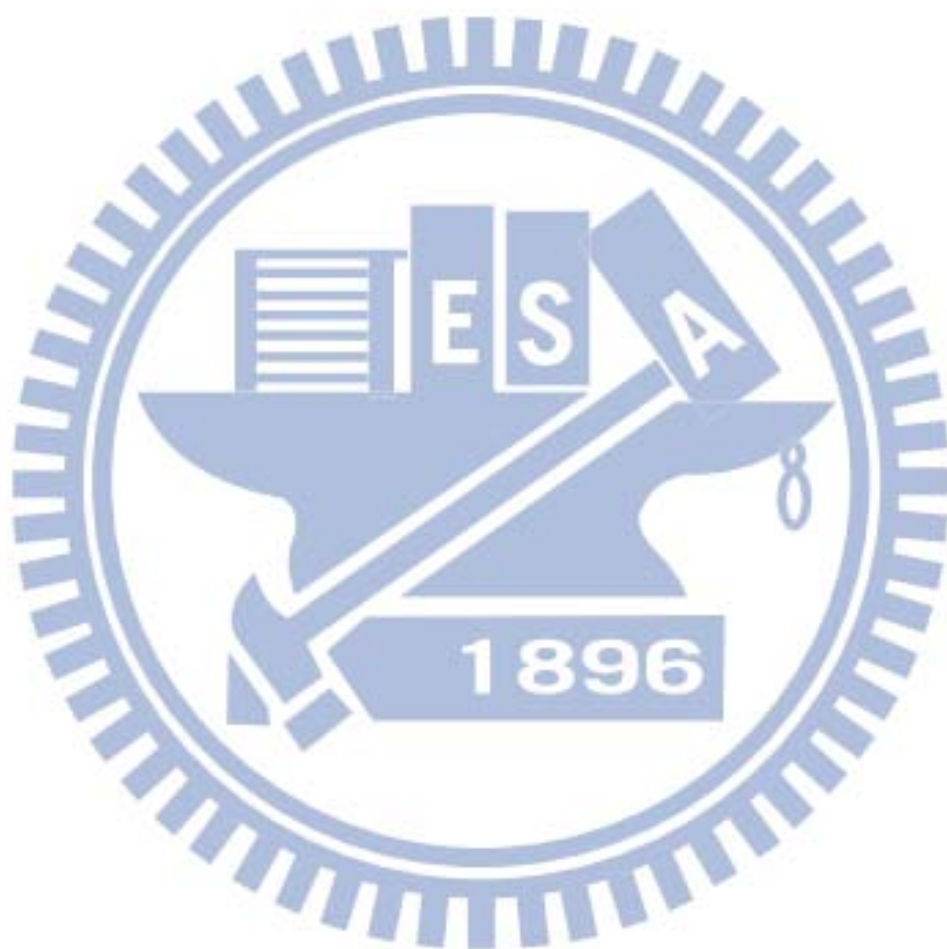
研 究 生:劉奇青　　　　　　　　指導教授:任盛源　教授

莊振益　教授

國立交通大學

電子物理研究所

中文摘要：

　　本實驗計畫為，鐵─鎳─鎵合金材料鐵磁共振與磁彈性質的研究。其中，在膜材的研究方面，我們是利用磁控濺鍍在基板上沉積成薄膜，我們分別沉積系列合金$Fe_{81-x}Ni_xGa_{19}$於矽基板上，和沉積系列合金$Fe_{81-y}Ni_yGa_{19}$於玻璃基板上，其中x、y為 0 到 26。我們已經做的量測主要為：(1)磁滯伸縮的量測、(2)易軸、難軸的磁滯曲線、(3)鐵磁共振的實驗。鐵磁共振在 9.6GHz 的交變磁場下執行，透過Kittle模型我們可以得到自然共振頻率，再透過磁滯曲線的資訊我們可以得到Gilbert阻尼係數。在薄膜的實驗中，我們得到幾個材料的特性:(1)在系列合金中,磁異向場隨鎳的原子百分比增加而降低、(2)自然共振頻率隨鎳的增加而降低、(3) Gilbert阻尼係數亦隨鎳的原子百分比增加而降低、(4)磁致伸縮的峰值出現在鎳原子百分比為 22 的時候。其中，特性(1)、(2)和(3)皆因為鎳元素取代鐵元素時降低其合金的磁性，因而降低了磁異向能量，磁異向場亦隨之降低，進而牽動自然共振頻率與Gilbert阻尼係數。特性(4)系因鎳的添加而改變了薄膜的晶相，進而提升薄

膜的磁致伸縮。至此，我們發現$Fe_{59}Ni_{22}Ga_{19}$在玻璃上有很優良的磁彈性質並可以在微波中應用。

Yager、Galt和Merritt指出鐵磁共振的半高寬與磁異向場大小有關，其實驗證明磁異向場越大，則鐵磁共振半高寬越寬，而在系列和金中增加鎳原子百分比可有效降低磁異向場，進而得以降低Gilbert阻尼係數。另外，由XRD的數據顯示，系列合金中鎳原子百分比的增加可有效抑制$D0_{19}$ 相與$L1_2$ 相的生成，證據顯示，甚至在鎳原子百分比達到 22 百分比時，合金薄膜中僅存在A2 相，$D0_{19}$ 相與 $L1_2$ 相其磁伸縮值皆為負值，不利合金薄膜飽和磁伸縮最佳化，從實驗數據中我們也得到鎳原子百分比達到 22 百分比的系列合金，有最佳化的飽和磁致伸縮值。

另外，此篇論文也針對$Fe_{81-z}Ni_zGa_{19}$系列合金薄帶做一系列的探討，其中z為 0 到 24。薄帶樣品是由快速冷淬法所製備而成，由XRD數據顯示，材料的晶格常數與鎳成分的添加有對應關係。由磁滯曲線的觀察，當合金薄帶添加鎳以後，磁異向性能量降至零，變成等向性質的磁性材料，卻也分別降低與提高飽和磁化量和矯頑磁力。從磁彈性質的研究中，我們發現楊氏係數隨鎳原子百分比的增加而降低，並由ΔE效應，使觀察到於系列合金中添加元素鎳的所產優勢，這優勢更進而影響磁致伸縮的大小，我們發現在鎳佔原子百分比為 7 時，擁有最大的磁致伸縮量。於此結果我們認為$Fe_{74}Ni_7Ga_{19}$合金薄帶有很優良的磁彈性質並可製成元件加以應用。

於鐵—鎵合金中添加鎳元素可以有下降低其的磁異向性，在薄帶研究中，甚至發現鎳元素的添入更可使材料變成等向性，而正是對軟磁材料的應用層面相當有利的一個條件。

Ferromagnetic resonance and magneto-elastic properties of $(FeNi)_{81}Ga_{19}$ alloys

Student : Chi-Ching Liu

Advisor: Prof. Shien-Uang Jen
Prof. Jenh-Yih Juang

Department of Electrophysics
National Chiao-Tung University

Abstract:

$Fe_{81-x}Ni_xGa_{19}$/Si(100) and $Fe_{81-y}Ni_yGa_{19}$/glass films, where x or y = 0 - 26, were made by the magnetron sputtering method. We have performed three kinds of experiments on these films:

[i] the saturation magnetostriction (λ_S) measurement; [ii] the easy-axis and hard-axis magnetic hysteresis loop measurements; [iii] the ferromagnetic resonance (FMR) experiment to find the resonance field (H_R) with an X-band cavity tuned at f_R = 9.6 GHz. The natural resonance frequency, f_{FMR}, of the Kittel mode at zero external field (H = 0) was then obtained and used to calculate the Gilbert damping constant.

The main findings of this study are summarized:

[i] H_K decreases, as x or y increases; [ii] f_{FMR} decreases, as x or y increases; [iii] α decreases from 0.052 to 0.020 and then increases from 0.020 to 0.050, as x increases, and α decreases from 0.060 to 0.013, as y increases; [iv] λ_S reaches maximum when x = 22. The reason of the [i], [ii] and [iii] are described below: as addition Ni replaces Fe at.% in alloys magnetism in rich-Fe alloys is reduced. As a result, the magnetic anisotropy energy causes the H_K to decrease, and, therefore, f_{FMR} and α also decrease. The reason of [iv]: as addition Ni into $Fe_{81}Ga_{19}$ alloy films enhances the A2 phase, which is good for λ_S in the alloys.

Thus, we conclude that the $Fe_{59}Ni_{22}Ga_{19}$/glass film should be suitable for the magneto-electric microwave device applications.

Yager, Galt, and Merritt pointed out that ΔH is related to H_K. Besides, we find the addition of Ni into $Fe_{81}Ga_{19}$ alloy films destabilize the $D0_{19}$ phase and $L1_2$ phase. Briefly speaking, when y = 22 at.%Ni, there is only one single A2 phase. That centralized the H_R and narrow ΔH in the alloys. In Eq. (2), α of the FeNiGa alloy is calculated from ΔH; α decreases, as ΔH decreases. On the other hand, the $Fe_{81}Ga_{19}$ film with the $D0_{19}$ phase and $L1_2$ phase are detrimental to saturation magnetostriction, so we get magnetostriction constants in the FeNiGa ternary alloys higher than those of the $Fe_{81}Ga_{19}$ binary alloys.

Another series of $Fe_{81-z}Ni_zGa_{19}$ ribbons, where z = 0 - 24, were made by the rapidly quenching method. The X-ray diffraction patterns showed that these ribbons change the lattices constants which depend on number of z. From hysteresis loops information, the ribbons become isotropic in magnetic anisotropy, M_s decreases from 170 emu/g to 116 emu/g, and H_c inceases from 4.8 Oe to 11.7 Oe, as Ni is added in. Young's modulus (E_s) at magnetization saturation and ΔE effect were estimated from the strain curve. We discovered that as z increases, $\Delta E/E_0$ increases. The most important result is that λ reaches maximum when z = 7 at.%Ni. We conclude that the $Fe_{74}Ni_7Ga_{19}$ ribbon should be most suitable for the magneto-electric device application.

The addition of Ni into $Fe_{81}Ga_{19}$ alloys refined the magnetic anisotropy energy which let the H_K decreases, as Ni content increases. Even in the series $Fe_{81-z}Ni_zGa_{19}$ ribbons, there becomes isotropic magnetic anisotropy energy.
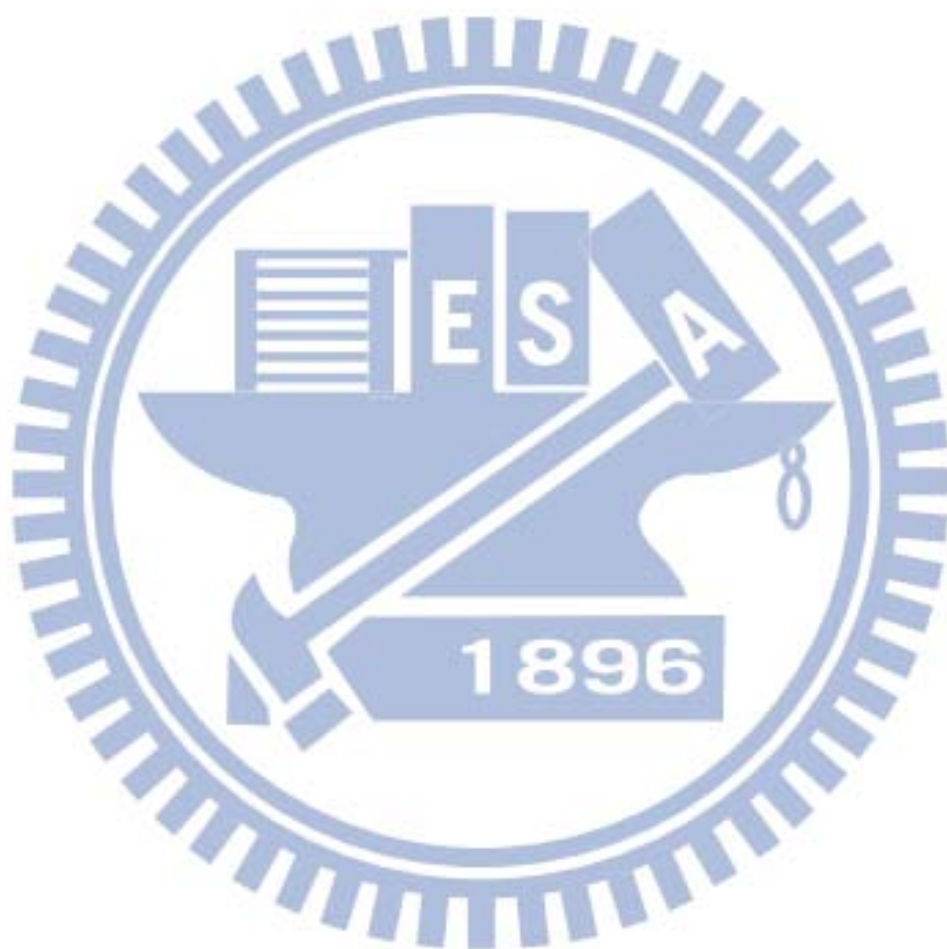
誌謝

　　首先要感謝，中央研究院物理所　任盛源老師對學生的費心，無論是研究上或是生活上，老師總是傳承經驗，並且不吝惜的給予指導；更一步步在實驗中訓練學生對實驗的敏銳度及嚴謹的態度，這將會是學生一輩子受用不盡的寶藏。此外也要特別感謝，交通大學電子物理系　莊振益老師對學生的指導，總是能見微知著的給予學生建議，適時的引導方向，更讓學生明瞭細節的重要性，相信這將會是將來能夠推動學生能百尺竿頭更進一步的動力。

　　再來要感謝交大的原銘、家宏、培元、韋呈、皓葦學長及中研院的宗霖學長，總是能在課業上給予幫助，並在研究中提出一些獨到的見解，使本人有更多元的視野。也要感謝交大的同儕雁夫、君緯，記得修課時，一起寫作業、一起熬夜念書、一起找出答案的日子，後來也常常在本人的研究中提出意見，更能激發很多思考的新方向。除了學業上的幫助，也要謝謝學長、同學及學弟妹在課餘時間所提供的歡樂，總是能讓本人在疲憊之後能重新打起精神繼續前進。

　　最後要感謝我的家人，尤其是父親劉元森先生與母親李碧釵女士，在不算短的學生生涯裡，提供不虞匱乏的生活，從不用為了日子而煩惱，這份養育的恩情是求學過程中最大的助力。並感謝我的妹妹玕玫，在成長的過

程中與我的互相省思，使我能更確定自己要走的路，更要感謝從不曾怨懟我仍未負擔家計，不給我這方面的壓力，使我能沒有顧慮的完成學業。當然，還要感謝一路上相互扶持，幫我加油打氣的朋友，有你們真好。

Contents

Figure and Table Lists

1. Introduction

1.4 Magneto-Electric Microwave Device

The desirable properties for soft magnetic materials are high permeability (μ) and low loss. The hysteresis loss is the most important loss in ferromagnetic substances at low driving frequencies. This phenomenon, known as the Barkhausen effect, was discovered in 1919. This effect is the strongest on the steepest part of the magnetic hysteresis curve and is evident for sudden and discontinuous changes in magnetization. The curve is shown in Fig. 1.1, where the magnification factor applied to one portion of the curve is of the order of 10^9. However, in the high frequency case the hysteresis loss becomes less important. Due to the domain wall displacement, which is the main origin of the hysteresis, is mostly damped in this range and is replaced by the rotation magnetization. There is one example shown in Fig. 1.2. The total loss per cycle (Pt) increases with frequency, as expected, but not linearly. (The measurements cannot be carried to higher frequencies, because the skin effect prevents the sample from being fully magnetized.) There is also a substantial discrepancy between the measured eddy-current loss and calculated classically. The difference between these two losses is called the anomalous loss, and may be as large as or even larger than the calculated eddy-current loss. It appears only because the classical calculation of eddy-current loss ignores the presence of domain and domain wall motion, and is therefore under-estimated. Hence, it is reasonable to compare the observed loss with the calculated classical loss and

find their difference as the anomalous loss. When the domain structure of the material is taken into account, the calculated eddy-current loss may exceed the classical loss, and the difference between the two is larger the larger the domain size. The difficulty is that the details of the domain structure and of the domain wall motion are not known in an actual sample, so that calculations can only be made for assumed and simplified models. Thus, the next important loss for ferromagnetic metals and alloys is the eddy current loss. Since a power loss of this type increases in proportion to the square of the frequency, it plays an important role in the high frequency, usually the radio frequency, range[1-3]. Moreover, if the frequency is increased further into the microwave range, one will encounter the ferromagnetic resonance (FMR) phenomenon. General speaking, the magneto-electric device is used in microwave which need to reduce the eddy current loss first. So that, reduce the Gilbert damping parameter (α) in the magnetic materials which is the motivation in this study.

In this study, we wish to find soft magnetic materials, which may be used in a tunable magneto-electric microwave device[4] or other rf/microwave magnetic devices. In these devices, the basic requirements for the soft ferromagnetic films are that low coercivity (H_C), high saturation magnetization ($4\pi M_S$), high saturation magnetostriction (λ_S), high rotational permeability (μ_r), high limiting (or natural resonance) frequency (f_{FMR}), and low Gilbert damping parameter (α).
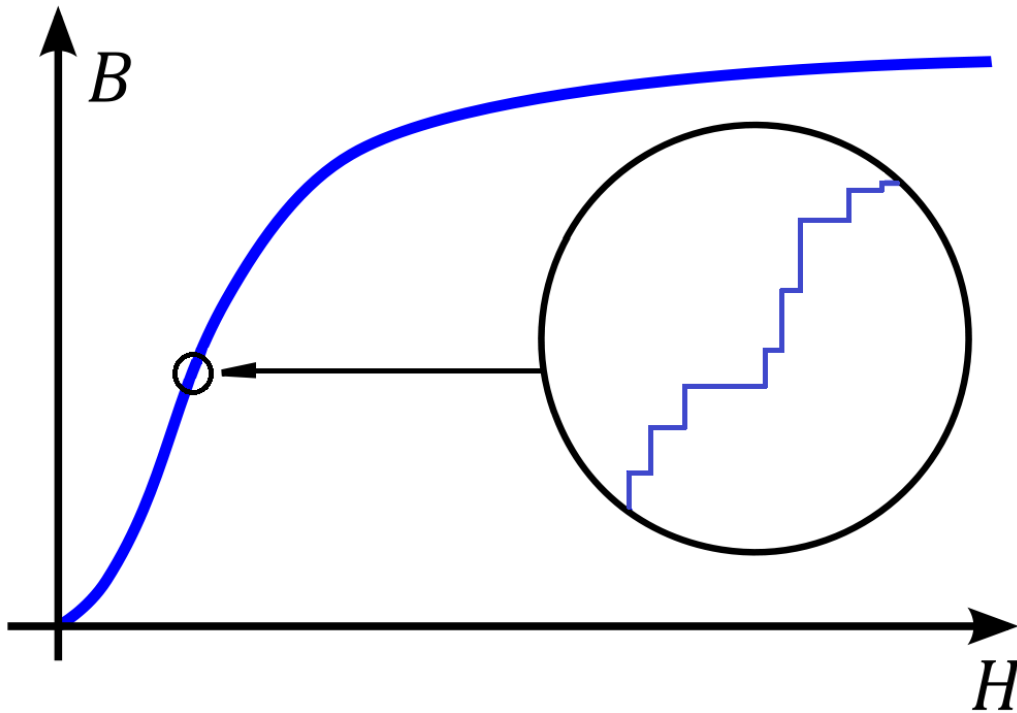
Fig. 1.1 shows the schematic illustration of the Barkhausen effect.
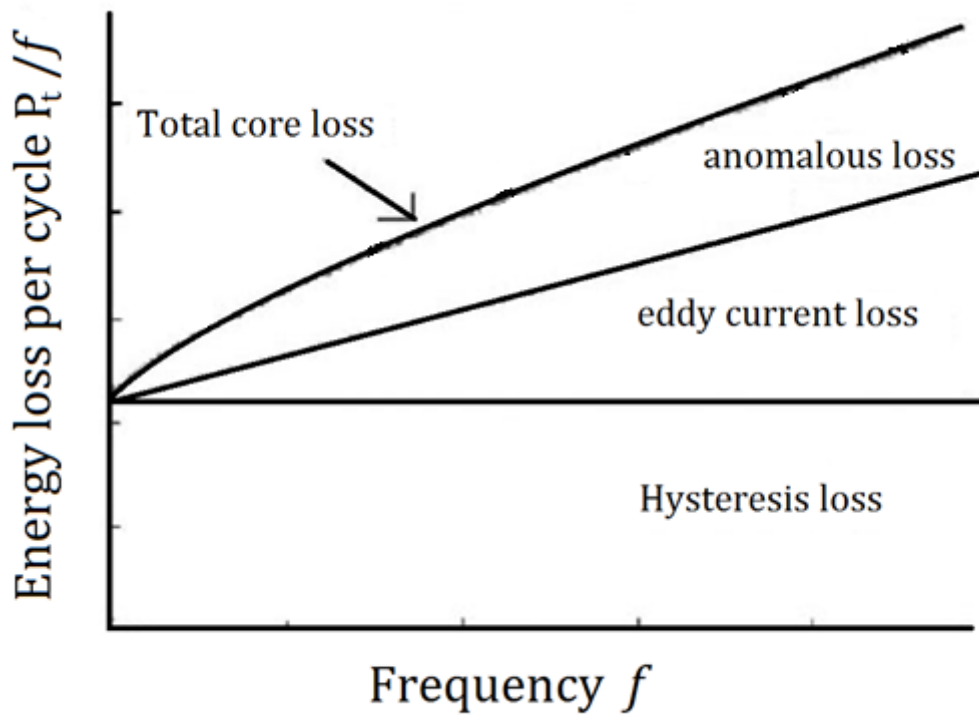
Fig. 1.2 Conventional types of in transformer cores.

1.2 Fundamental Properties of Fe-Ga alloys

From many researching literatures especially Ref. [4], we find that the Fe-Ga alloys seem to be good soft magnetic materials which could be used for the device applications mentioned above. For example, the Fe-Ga alloys are low coercivity soft magnetic materials with low saturation or anisotropy field (H_S), about 100 Oe for single crystals (SC) and about 50 Oe for poly-crystals (PC)[5, 6], high saturation magnetization, about 18 kG[5], high saturation magnetostriction shown in Fig. 1.3, about 200 ~ 400 ppm for SC and about 40 ~ 100 ppm for PC sample[7, 8]. Note that although the FeGa single crystal has large λ_S value, which is favorable in terms of magneto-electric coupling, its ferromagnetic resonance line-width (ΔH), about 450 ~ 600 Oe[9] at X band, is however yet too large for tuning efficiency. In other words, α of a FeGa single-crystal film is too large. In reaching of Ref. [4], Lou and Insignares added of B atoms into the FeGaB alloys leads to refined grain size and/or a more disordered lattice, and the XRD patterns are shown in Fig. 1.4. Moreover, from a device application point of view, it is usually more laborious to grow a single-crystal than a polycrystalline film. Thus, in this study we shall concentrate on the polycrystalline film case only. Besides, it has been found that incorporation of about 12% of the metalloid element, such as boron (B) or carbon (C), into the $Fe_{81}Ga_{19}$ alloy would improve λ_S[10 - 12]. Note, however, there is a discrepancy between $\lambda_S \approx 70$ ppm for the $(FeGa)_{88}B_{12}$ film and $\lambda_S \approx 45$ ppm for the as-quenched $(FeGa)_{88}B_{12}$ bulk[4, 10].
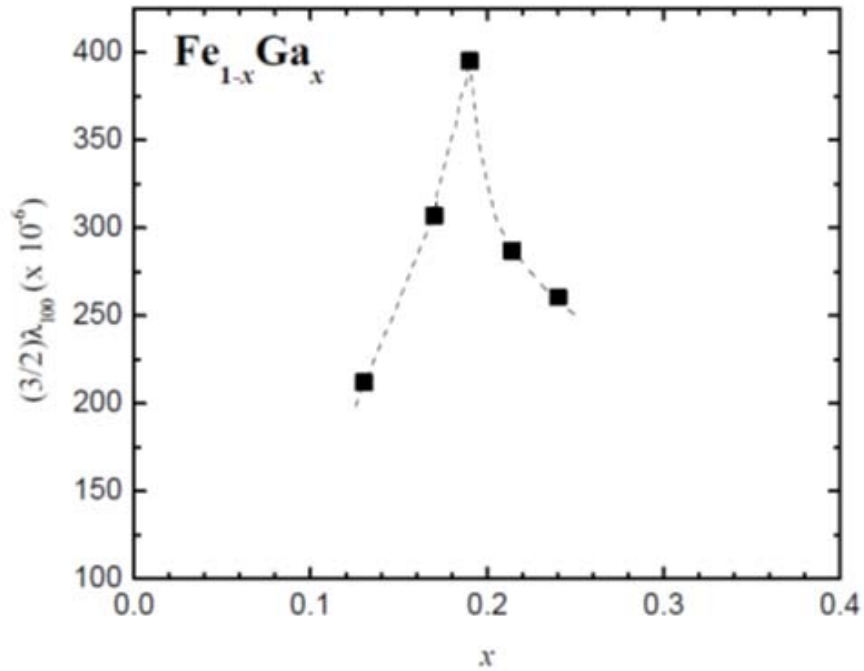
Fig. 1.3 Room temperature magnetostriction of $Fe_{1-x}Ga_x$ alloys quenched into water from $800^{\circ}C$[7].
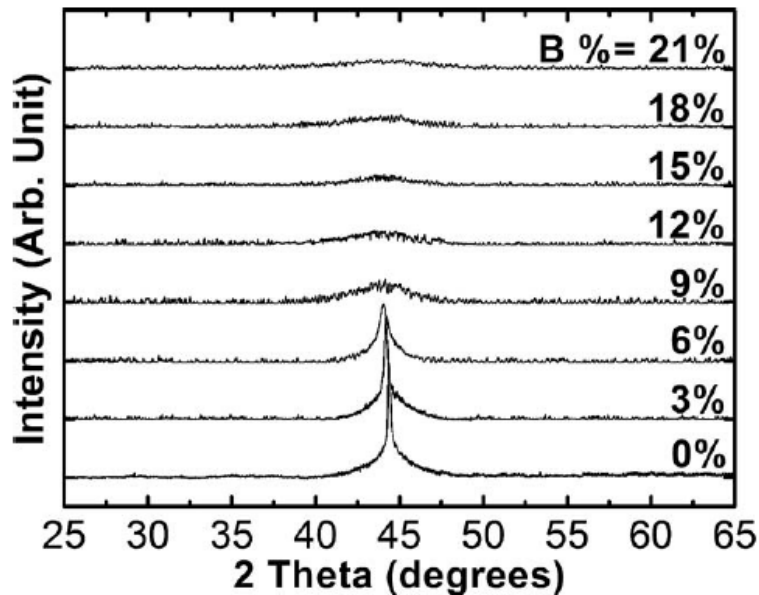
Fig. 1.4 The XRD patterns for FeGaB films with different B contents.

1.3 Motivation

In this study, we chose one series of the $Fe_{81-x}Ni_xGa_{19}$/Si(100) and another one series of the $Fe_{81-y}Ni_yGa_{19}$/glass films, where x or y ranges from 0 to 26%, and other series of magnetic metallic ribbons, $Fe_{81-z}Ni_zGa_{19}$ with z = 0, 3, 7, 13, and 24. The TEM photos are shown in Fig. 1.5 from Ref. [13], Bormio-Nunes and Sato Turtelli added nickel (Ni) element into the FeGa alloys leading to refined grain size and/or a more disordered lattice. Besides, it has been found that incorporation of the nickel (Ni) element, into the $Fe_{85}Ga_{15}$ alloy would improve magnetostriction, as shown in Fig. 1.6 and Fig. 1.7.

Hopefully, we can get the combinations of the following favorable features, such as low H_C or H_S, high $4\pi M_S$, high λ_S, from one of these FeNiGa ribbons and/or films for magneto-electric device. On the other hand, we want get the high μ_r, low ΔH or α, from one of these FeNiGa films for magneto-electric microwave device.[13 – 15]
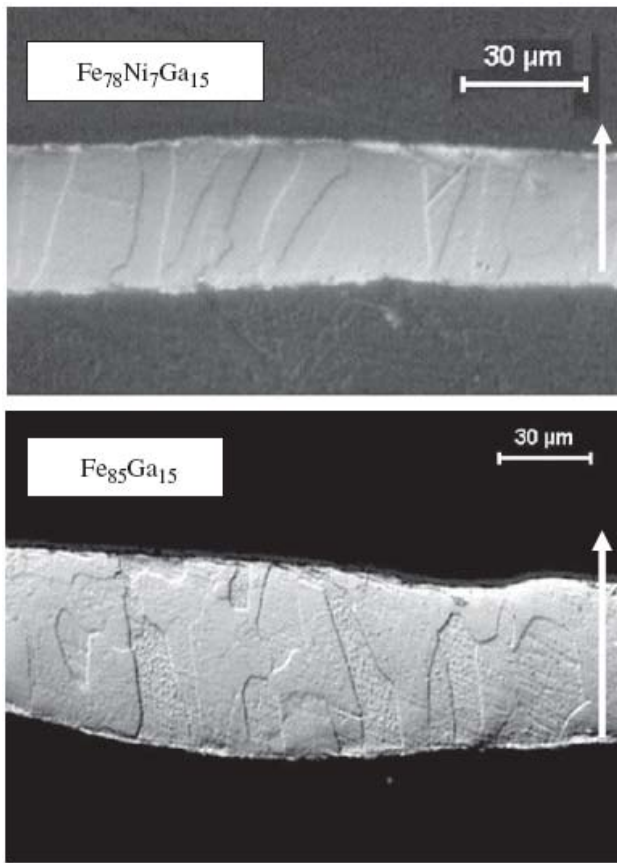
Fig.1.5 The cross-section TEM photos for $Fe_{85}Ga_{15}$ and $Fe_{78}Ni_7Ga_{15}$ ribbons[13].
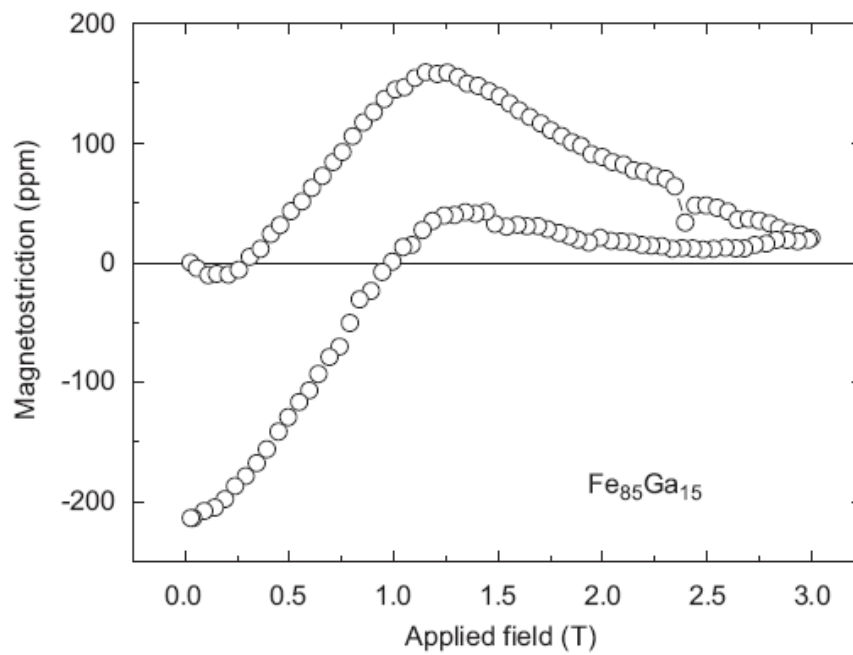
Fig. 1.6 Magnetostriction measured on stacked $Fe_{85}Ga_{15}$ ribbon, applying the field parallel to the ribbon thickness[13].
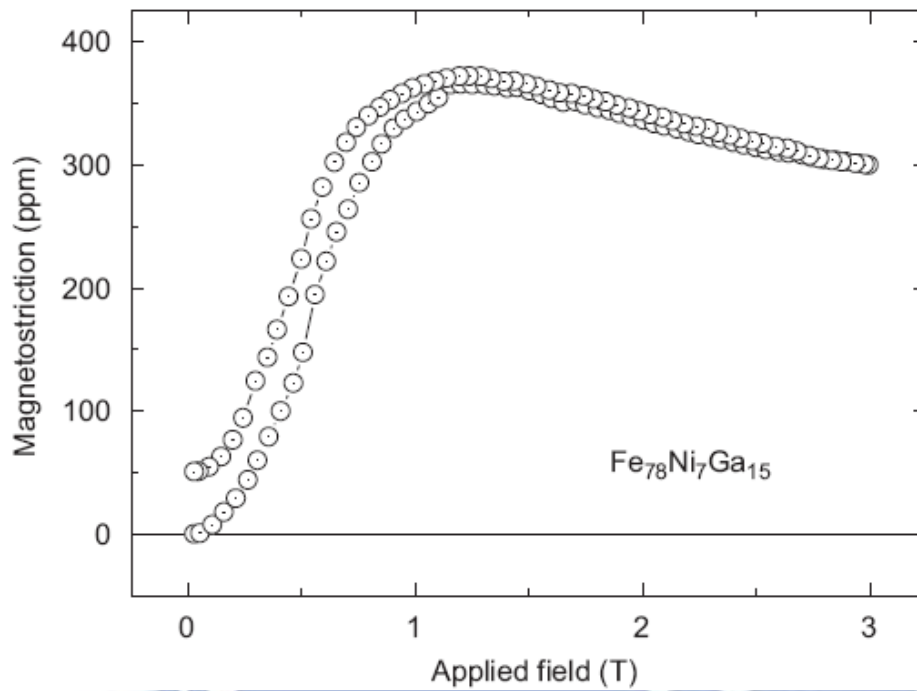
Fig. 1.7 Magnetostriction measured on stacked ribbons of $Fe_{78}Ni_7Ga_{15}$ applying the field parallel to the ribbon thickness[13].
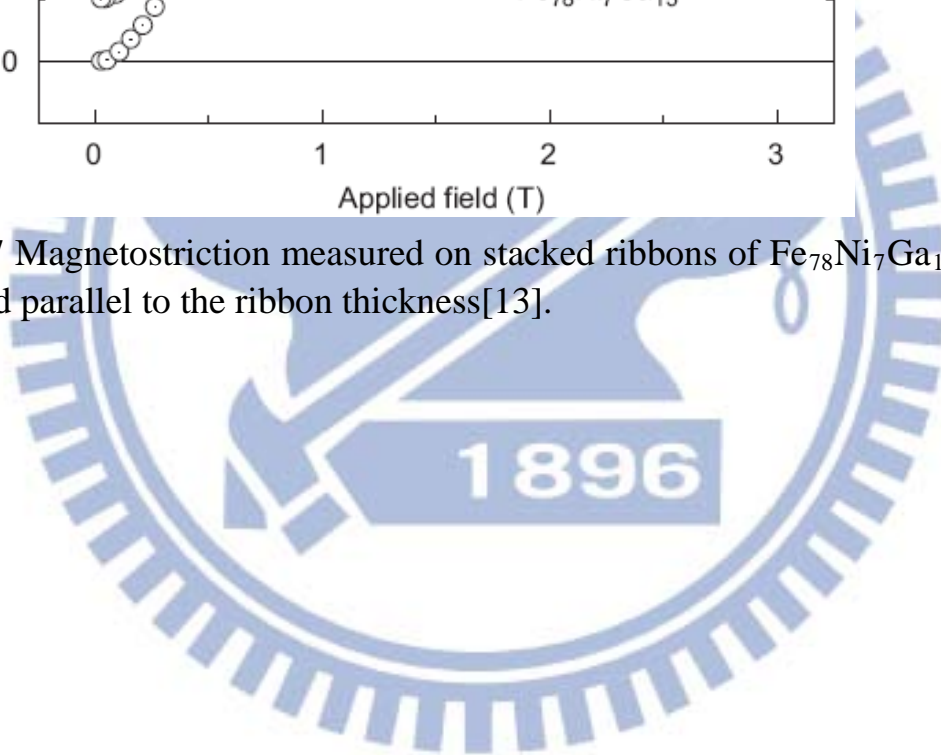
2. Brief review of magnetism and relevant effects

2.1 Magnetism

The first writings of magnetism appeared with a kind of mineral called magnetite (Fe_3O_4), which has been claimed that the Chinese used it in compasses sometime before 2500 B.C., but the precise date still remained unknown[3, 16].

The discovery of two regions named magnetic poles, or sometimes just "poles," which attracted a piece of iron more strongly than the rest of the magnetite, this discovery was made by P. Peregrines about 1269 A.D. Sometime later, Coulomb (1736-1806) found that there were two types of poles, now called positive or north poles, and negative or south poles. There is always with magnets and felt the mysterious forces of attraction and repulsion between two magnetic poles[3, 16]. The mysterious forces of attraction and repulsion between the two magnetic poles can be felt. This force of attraction and repulsion is proportional to the product of the strength of the poles and inversely proportional to square of the distance between them. This is Coulomb's law, which can be written mathematically as,

$$\vec{F} = k\frac{p_1 p_2}{r^2}\vec{r}_0 \qquad (2.1)$$

where $\vec{F}$ is the force, p_1 and p_2 the pole strengths, r the distance between the poles, and $\vec{r}_0$ one unit vector directed along r. The constant of proportionality k that occurs permits a definition of pole strength, and the proportionality constant k is equal 1 in the cgs-emu unit.

When a magnetic pole creates a magnetic field around it, and this field will then produces a force on second pole nearby. Experiment shows that this force is directly proportional to the product of the pole strength and field strength or field strength or field intensity $\vec{H}$,

$$\vec{F} = kp\vec{H}. \qquad (2.2)$$

The equation 2.2 then defines $\vec{H}$, a field of unit strength is one which exerts a force 1 dyne on a unit pole. A field of unit strength has an intensity of one oersted (Oe).

Besides, a magnet with poles of strength p located near each end and separated by distance l. Suppose the magnet is placed at an angle θ to a uniform field H (Fig. 2.1). Then a torque acts on the magnet, tending to turn it parallel to the field. The moment of this torque is

$$(pHsin\theta)\left(\frac{l}{2}\right) + (pHsin\theta)\left(\frac{l}{2}\right) = pHlsin\theta \qquad (2.3)$$

When $H=1$ Oe and $\theta=90^{o}$, the moment is given by

$$m = pl \qquad (2.4)$$

where *m* is the magnetic moment of the magnet. It is the moment of torque exerted on the magnet when it is at right angles to a uniform field of 1 Oe[2, 3, 16].

Consider a piece of iron is subjected to a magnetic field, it becomes magnetized, and the level of its magnetism depends on the strength of the field. We therefore need a quantity to describe the degree to which a body is magnetized. The application of an external magnetic field causes both an alignment of the magnetic moments of the spinning electrons and an induced magnetic moment due to a change in the orbital motion of electrons In order to obtain a formula for determining the quantitative change in the magnetic flux density caused by the presence of a magnetic material, we let $\vec{m}_k$ be the magnetic moment of an atom. If there are n atoms per unit volume, we define a magnetization vector, $\vec{M}$, as

$$\vec{M} = \lim_{\Delta v \to 0} \frac{\sum_{k=1}^{n\Delta v} \vec{m}_k}{\Delta v} \qquad (2.5)$$

Where Δv is the volume and n is the number of Δv[2, 16].

The magnetic properties of a material are characterized not only by the magnitude and sign of $\vec{M}$ but also by the way in which $\vec{M}$ varies with $\vec{H}$. The scalar ratio of these two quantities is called the susceptibility χ :

$$\chi = \frac{M}{H} \qquad (2.6)$$

Now they can be roughly classified into three main groups in accordance with their χ values[3, 16, 17].

(1) Diamagnetic, if χ is a very small negative number.

Electrons which constitute a close shell in an atom usually have their spin and orbital moments oriented so that the atom as a whole has no net moment. Thus the monoatomic rare gases He, Ne, Ar, etc., which have closed-shell electronic structures, are all diamagnetic. The macroscopic effect of this is equivalent to that of a negative magnetization that can be described by a negative magnetic susceptibility. The effect is usually very small, and χ for most known diamagnetic materials is in the order of -10^{-5}. (i.e., Cu, Hg, Ag)

(2) Paramagnetic, if χ is a very small positive number.

Arises mainly from the magnetic dipole moments of the spinning electrons. The alignment forces, acting upon molecular dipoles by the applied field, are counteracted by the deranging effects of thermal agitation. Unlike diamagnetism, which is essentially independent of temperature, the paramagnetic effect is temperature dependent, being stronger at lower temperatures where there is less thermal collision. (i.e., Na, Al)

(3) Ferromagnetic, if χ is a large positive number.

The magnetization of ferromagnetic materials can be many orders of magnitude larger than that of paramagnetic substances. Ferromagnetism can be explained in terms of magnetized domains. I will show more detail in the next section.

Besides, engineers are usually concerned only with ferromagnetic materials and need to know the total flux density $\vec{B}$ produced by a given field, then engineers become the definition in mks system. In addition, engineers are usually only concerned with ferromagnetic materials and the total flux density $\vec{B}$ produced by a given field. The mks system is generally used as the unit system in engineering application. They often find the $\vec{B}$, $\vec{H}$ curve, also called a magnetization curve, more useful than the $\vec{M}$, $\vec{H}$ curve. The ratio of B to H is called the permeability μ:

$$\mu = \frac{B}{H} \qquad \left(\frac{H}{m}, in\ mks\ system\right) \qquad (2.7)$$

When the magnetic properties of the medium are linear and isotropic, the magnetization is directly proportional to the magnetic field intensity:

$$\vec{B} = \mu\vec{H}$$

$$= \mu_0(1 + \chi)\vec{H}$$

$$= \mu_0\vec{H} + \vec{M} \qquad (2.8)$$

Where μ_0 is the permeability of free space is chosen to be

$$\mu_0 = 4\pi \times 10^{-7} \qquad \left(\frac{H}{m}\right). \qquad (2.9)$$

Where the proportionality constant k is equal to $4\pi/\mu_0$ in the mks system in

equation (2.1)
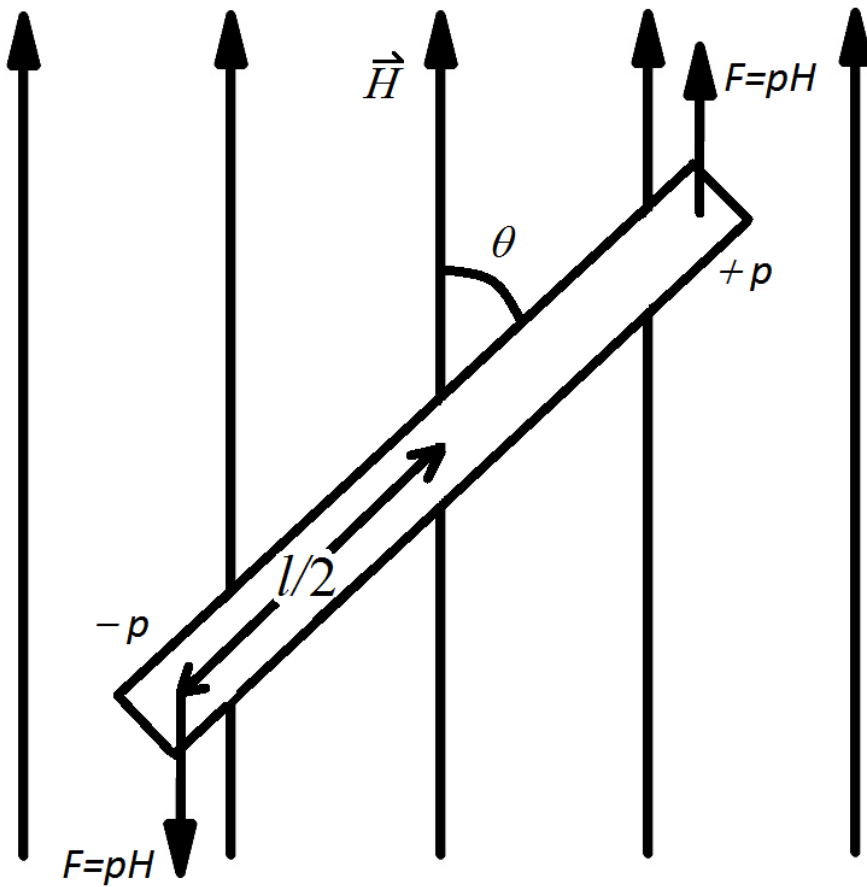
Fig. 2.1 Bar magnet in a uniform field[3].

2.2 Ferromagnet

According to the models of magnetized domains, which have been experimentally confirmed, a ferromagnetic material (such as Co, Ni, and Fe) is composed of many small domains, their linear dimensions ranging from a few microns to about 1 mm. These domains, each contain about 1015 or 1016 atoms, are fully magnetized in the sense that they contain aligned magnetic dipoles resulting from spinning electrons even in the absence of an applied magnetic field. Quantum theory asserts that strong coupling forces exist between the magnetic dipole moments of the atoms in a domain, holding the dipole moments in parallel. Between adjacent domains there is a transition region about 100 atoms thick called a domain wall. In a demagnetized state the magnetic moments of the adjacent domains in a ferromagnetic material have different directions, as exemplified in Fig. 2.2 by the polycrystalline specimen model shown[2, 3, 16, 17]. There were two different real examples shown in Fig. 2.3 and Fig. 2.4, which were observed domain structure by two techniques involved. In overall term overall, the random nature of the orientations in the various domains results in no net magnetization.

When an external magnetic field is applied to a ferromagnetic material, the walls of those domains having magnetic moments aligned with the applied field and which move in such a way as to make the volumes of those domains grow at the expense of other domains. As a result, magnetic flux density is increased. For weak applied fields, domain-wall movements are longer/ long acting reversible, and domain rotation toward the direction of the applied field will occur. For example, the M-H plane for $Fe_{86}V_{14}$ film is shown in Fig. 2.5, if an

applied field is reduced to zero at point P_1, the M-H relationship will not follow the red curve P_2P_1O, but will go down from P_2 to P_2', along the lines of the broken curve in the figure. This phenomenon of magnetization lagging behind the field producing it is called hysteresis. As the applied field becomes even much stronger (past P_1 to P_2), domain-wall motion and domain rotation will cause essentially a total alignment of the microscopic magnetic moments with the applied field, at which point the magnetic material is said to have reached saturation M_s. The curve OP_1P_2 on the M-H plane is called the virgin magnetization curve.

If the applied magnetic field is reduced to zero from the value at P_2, the magnetic magnetization does not reduce to zero but assumes the value at M_r. This value is called the residual or remanent magnetization (10 kOe =1 T) and is dependent on maximum applied field intensity. The existence of a remanent magnetization in a ferromagnetic material makes permanent magnets possible.

To make the magnetic magnetization of a specimen zero, it is necessary to apply magnetic field intensity H_c in the opposite direction. This required H_c; the coercive force; but a more appropriate name is coercive field intensity (in Oe). Like M_r, H_c also depends on the maximum value of the applied intensity.
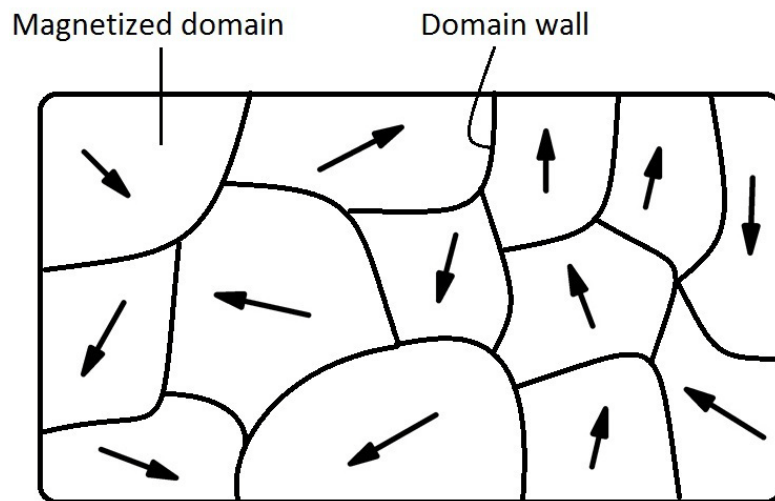
Fig. 2.2 Domain structure of a polycrystalline specimen model[17].
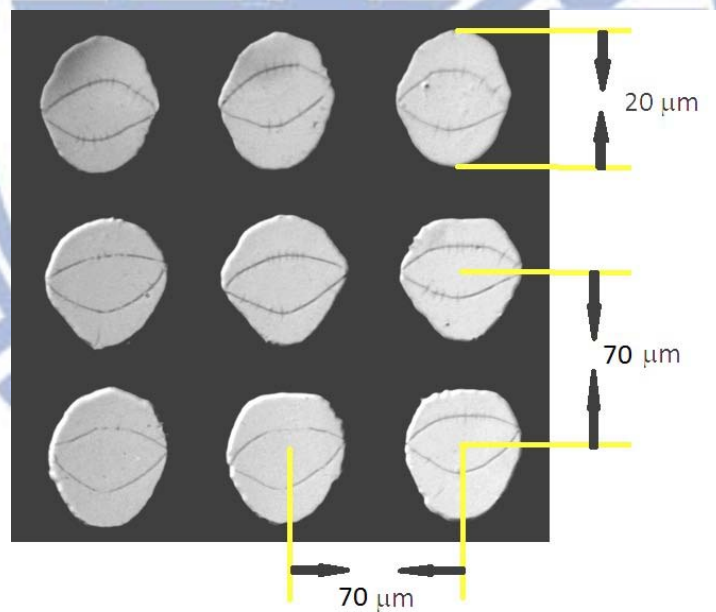
Fig. 2.3 The Bitter method image, which was taken in a zero field and at room temperature, of the $Fe_{81}Ni_{19}$ array films in a completely demagnetized state.
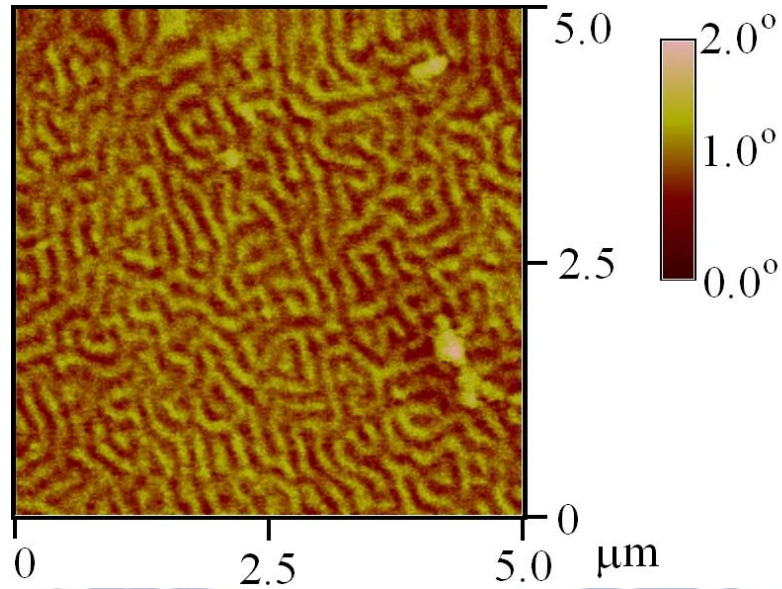
Fig. 2.4 The Magnetic Force Microscopy (MFM) image, which was taken in a zero field and at room temperature, of the $La_{0.7}Sr_{0.3}MnO_3$ (LSMO) films in a completely demagnetized state.
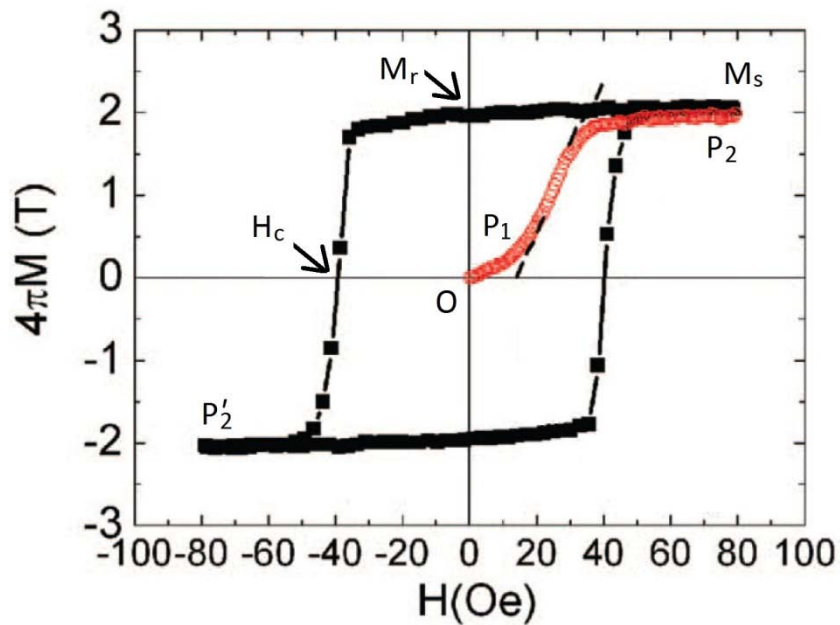
Fig. 2.5 The virgin magnetization (in red circles) and the major hysteresis (in black squares) curves of the $Fe_{86}V_{14}$ film. $4\pi M$ is the magnetization of the film[18].

2.2.1 Soft magnetic materials and Hard magnetic materials

Ferromagnetic materials for use in electric generators, motors, and transformers should have a large magnetization for a very small applied field. As the applied magnetic field intensity varies periodically between $\pm$ H_{max}, the hysteresis loop is traced once per cycle. The area of the hysteresis loop corresponds to energy loss (hysteresis loss) per unit volume per cycle. Hysteresis loss is the energy lost in the form of heat in overcoming the friction encountered during domain-wall motion and domain rotation. Ferromagnetic materials, which have tall narrow hysteresis loops with small loop areas, are referred to as "soft" materials, there is shown in Fig. 2.6 red curve; they are usually well-annealed materials with very few dislocations and impurities so that the domain walls can move easily.

Good permanent magnets, on the other hand, should show a high resistance to demagnetization. This requires that they are made with materials that have large coercive field intensities H_c and hence wider hysteresis curve, like the blue curve in Fig. 2.6. These materials are referred to as "hard" ferromagnetic materials. The coercive field intensity of hard ferromagnetic materials can be 500 Oe or more, whereas that for soft materials is usually 50 Oe or less[2, 3, 16].
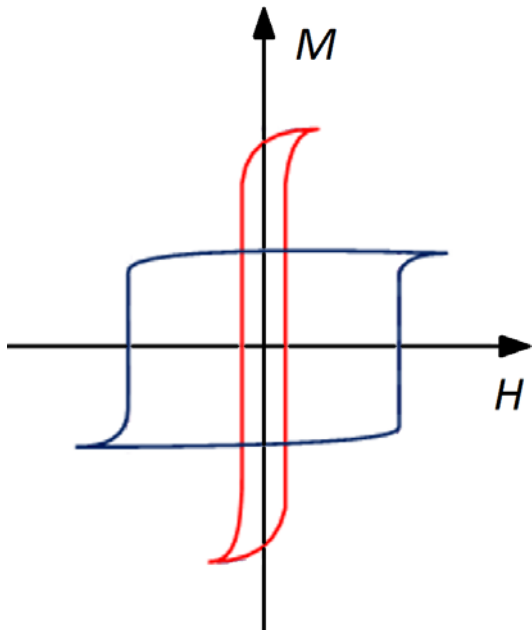
Fig. 2.6 This figure is the soft ferromagnetic material hysteresis (in red circles) and the hard ferromagnetic material hysteresis (in blue squares) curves.

2.2.2 Curie temperature

As previously indicated, ferromagnetism is the result of strong coupling effects between the magnetic dipole moments of the atoms in a domain. When the temperature of a ferromagnetic material is raised to such an extent that the thermal energy exceeds the coupling energy, the magnetized domains become disorganized. Above this critical temperature, known as the Curie temperature (T_c); a ferromagnetic material behaves like a paramagnetic substance. Hence, when a permanent magnet is heated above its curie temperature, it loses its magnetization. The Curie temperature of most ferromagnetic materials lies between a few hundred to a thousand degrees Celsius, that of iron being 770°C[2, 3].

2.3 Magnetic anisotropy

The magnetization changes from zero to the saturation value, which the value of M_s itself will be regarded simply as a constant of the material. If we understand the several factors that affect the shape of the M, H curve, we will then understand why some materials are magnetically soft and others are magnetically hard.

One factor which may strongly affect the shape of the M, H curve, or the shape of the hysteresis loop, is magnetic anisotropy. This term simply means that the magnetic properties depend on the direction in which they are measured. This general subject is of considerable practical interest, because anisotropy is exploited in the design of most magnetic materials of commercial importance. A thorough knowledge of anisotropy is thus important for an understanding of these magnetic materials[2, 3].

There are several kinds of anisotropy such as crystal anisotropy, shape anisotropy, stress anisotropy, and induced anisotropy.

2.3.1 Crystal anisotropy

The existence of crystalline anisotropy may be demonstrated by the magnetization curves of single-crystal specimens. By magnetization curve we mean the component of magnetization in direction of applied field M, plotted as a function of the applied field[16]. Magnetization curves for single crystals of iron, nickel, and cobalt for various orientations of the applied field with respect to the crystal axis for room temperature are shown in Fig. 2.7, Fig. 2.8, and Fig. 2.9. It is clear that much smaller fields are required to magnetize the crystals to

saturation along which the magnetization tends to lie are called easy axis (EA); the axis along which it is most difficult to produce saturation are called hard axis (HA).
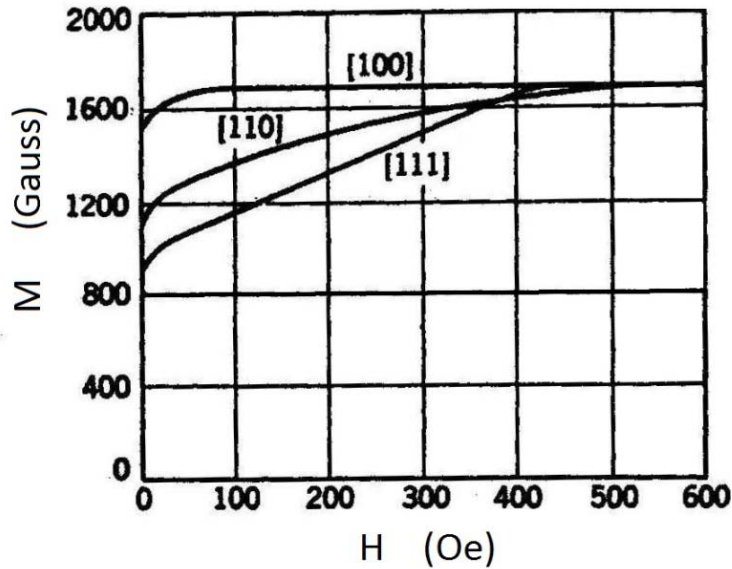
Fig. 2.7 Magnetization curves of single-crystal of iron[16].
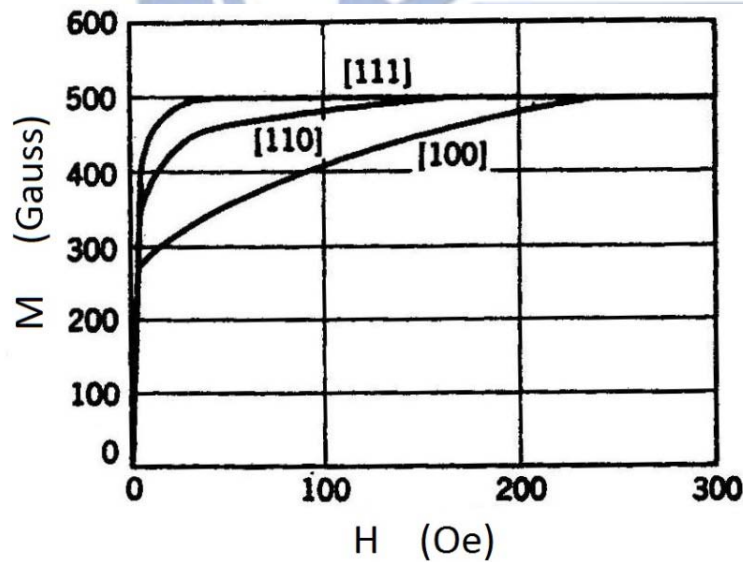
Fig. 2.8 Magnetization curves of single-crystal of nickel[16].
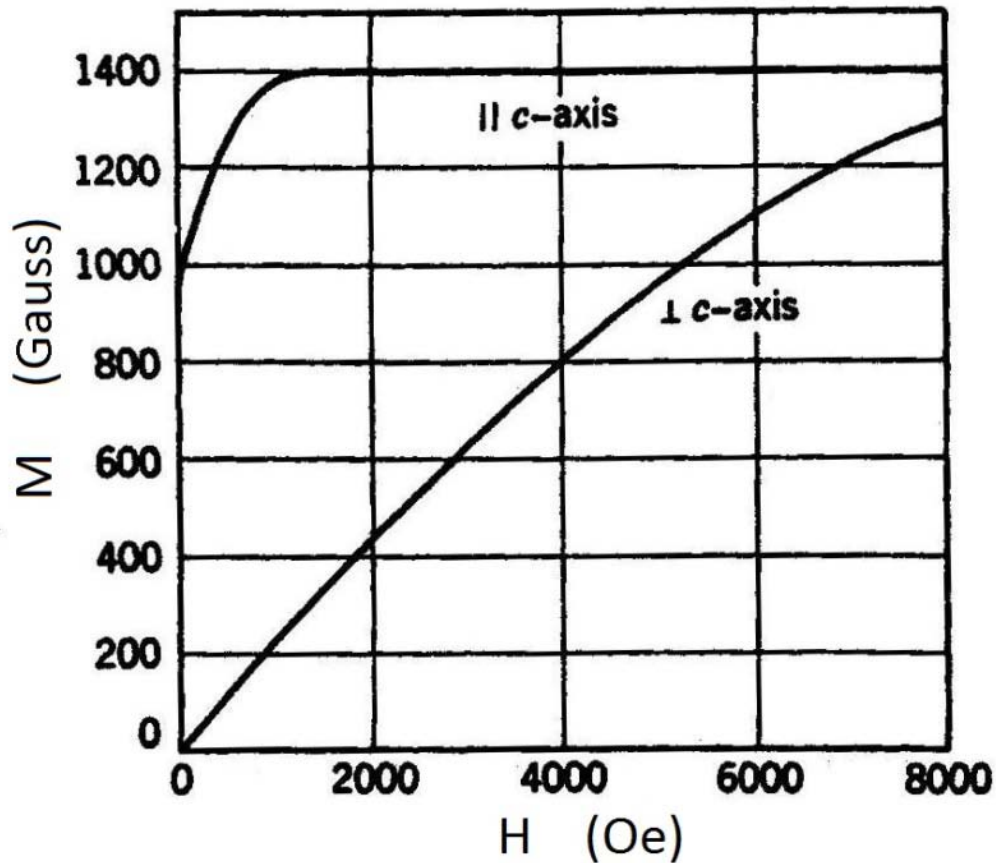
Fig. 2.9 Magnetization curves of single-crystal of cobalt[16].

2.3.2 Shape anisotropy

Consider a polycrystalline specimen having no preferred orientation of its grains, and therefore no net crystal anisotropy. If it is spherical in shape, the same applied field will magnetize it to the same extent in any direction. But if it is nonspherical, it will be easier to magnetize it along a long axis than along axis. The reason for this is the demagnetizing field along a short axis is stronger than along a long axis. The applied field along a short axis then has to be stronger to produce the same true field inside the specimen. Thus shape alone can be a source of magnetic anisotropy.

2.3.3 Stress anisotropy

The main reason for stress anisotropy is the inverse magnetostrictive effect, which will be discussed in section 2.4.   Simply put, there exists an inverse effect which causes such properties as permeability and the size and shape of the hysteresis loop to be strongly dependent on stress in many materials. Magnetostriction therefore has many practical consequences, and a great deal of research has accordingly been devoted to it[2, 3, 16].

2.3.4 Induced anisotropy

Various other anisotropies may be induced in certain materials, chiefly solid solutions, by appropriate treatments.   These induced anisotropies are of interest both to the physicist, for the light they throw on basic magnetic phenomena, and to the technologist, who may exploit them in the design of magnetic materials for specific applications[2, 3, 16].

The following treatments can induce magnetic anisotropy:

(1) Magnetic annealing:

This mean heat treatment in a magnetic field, sometimes called a

thermomagnetic treatment.   This treatment can induce anisotropy in

certain alloys.

(2) Stress annealing:

This means heat treatment of a material that is simultaneously

subjected to an applied stress.

(3) Plastic deformation:

This can cause anisotropy both in solid solutions and in pure metals,

but by quite different mechanisms.

(4) Magnetic irradiation:

This means irradiation with high-energy particles of a sample in a magnetic field.

2.4 Magnetostriction[2, 3]

When a ferromagnetic substance is exposed to a magnetic field, its dimensions change. This effect is called magnetostriction. It was discovered in 1842 by James Joule, who showed that an iron rod increased in length when it was magnetized lengthwise by a weak field. The fractional change in length $\Delta l/l$ is simply a strain, and, to distinguish it from the ε caused by an applied stress, we give the magnetically induced strain a special symbol λ[2, 3]:

$$\lambda = \frac{\Delta l}{l} \qquad (2.10)$$

The value of λ measured at magnetic saturation is called the saturation magnetostriction λ_s, and, when the word "magnetostriction" is used without qualification, λ_s is usually meant. Magnetostriction occurs in all pure substances. However, even in strongly magnetic substances, the effect is usually small: λ_s is typically of the order of 10^{-5}[3].

The longitudinal, sometimes called Joule, magnetostriction just described is not the only magnetostrictive effect. Others include the magnetically induced torsion or bending of a rod. These effects, which are really only special cases of the longitudinal effect, will not be described here.

The value of the saturation longitudinal magnetostriction λ_s can be positive, negative, or, in some alloys at some temperature, zero. The value of λ depends on the extent of magnetization and hence on the applied field, and Fig. 2.10 shows how λ typically varies with $\vec{H}$ for a substance with positive

magnetostriction. As mentioned in the preceding, the process of magnetization occurs by two mechanisms, domain-wall motion and domain rotation. For example, the magnetostriction of an iron crystal dependence on magnetic field in the [100] direction is shown in Fig. 2.11.

Between the demagnetized state and saturation, the volume of a specimen remains very nearly constant. This means that there will be a transverse magnetostriction λ_t very nearly equal to one-half the longitudinal magnetostriction and opposite in sign, or

$$\lambda_t = -\frac{1}{2}\lambda \qquad (2.11)$$

When technical saturation is reached at any given temperature, in the sense that the specimen has been converted into a single domain magnetized in direction of field, further increase in field cause a small further strain. This causes a slow change in λ with H called forced magnetostriction, and the logarithmic scale of H in Fig. 2.10 roughly indicates the fields required for this effect to become appreciable. It is caused by the increase in the degree of spin order which very high fields can produce[3].

The longitudinal, forced-magnetostriction strain λ shown in Fig. 2.10 is a consequence of a small volume change, of the order of $\Delta V/V = 10^{-10}$ per Oe, occurring at fields beyond saturation and called volume magnetostriction. It causes an equal expansion or contraction in all directions. Forced magnetostriction is a very small effect and has no bearing on the behavior of practical magnetic materials in ordinary fields[2, 3].
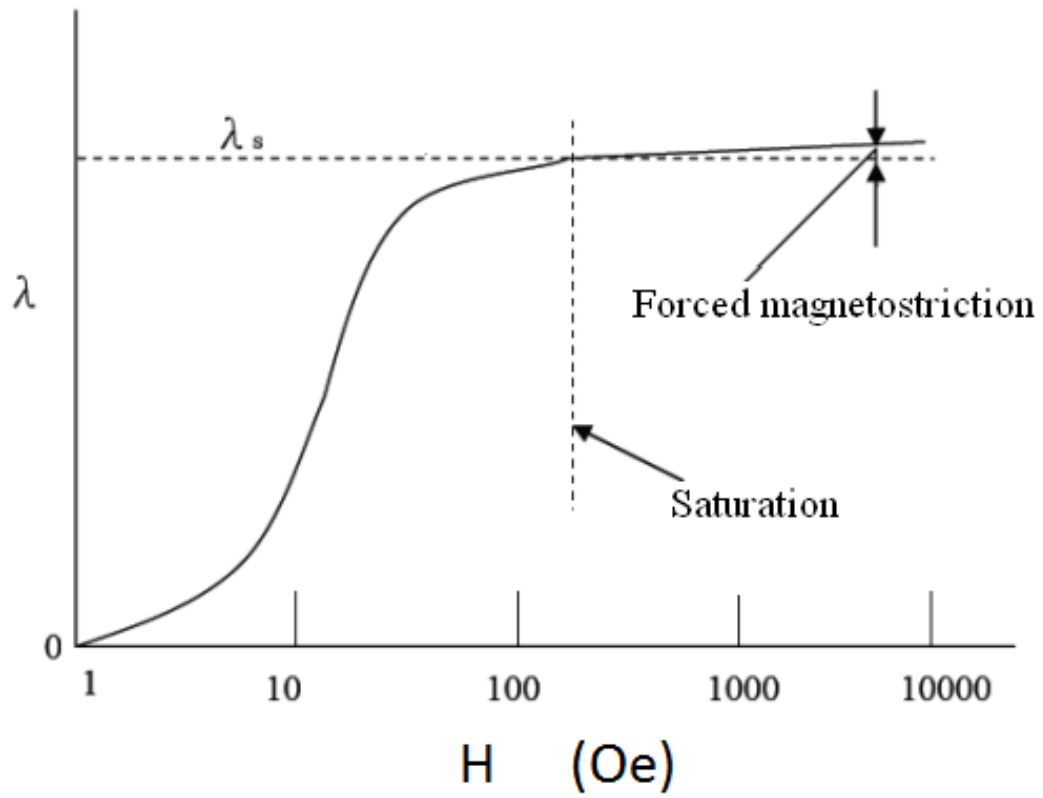
Fig. 2.10 shows dependence of magnetostriction on magnetic field[2].
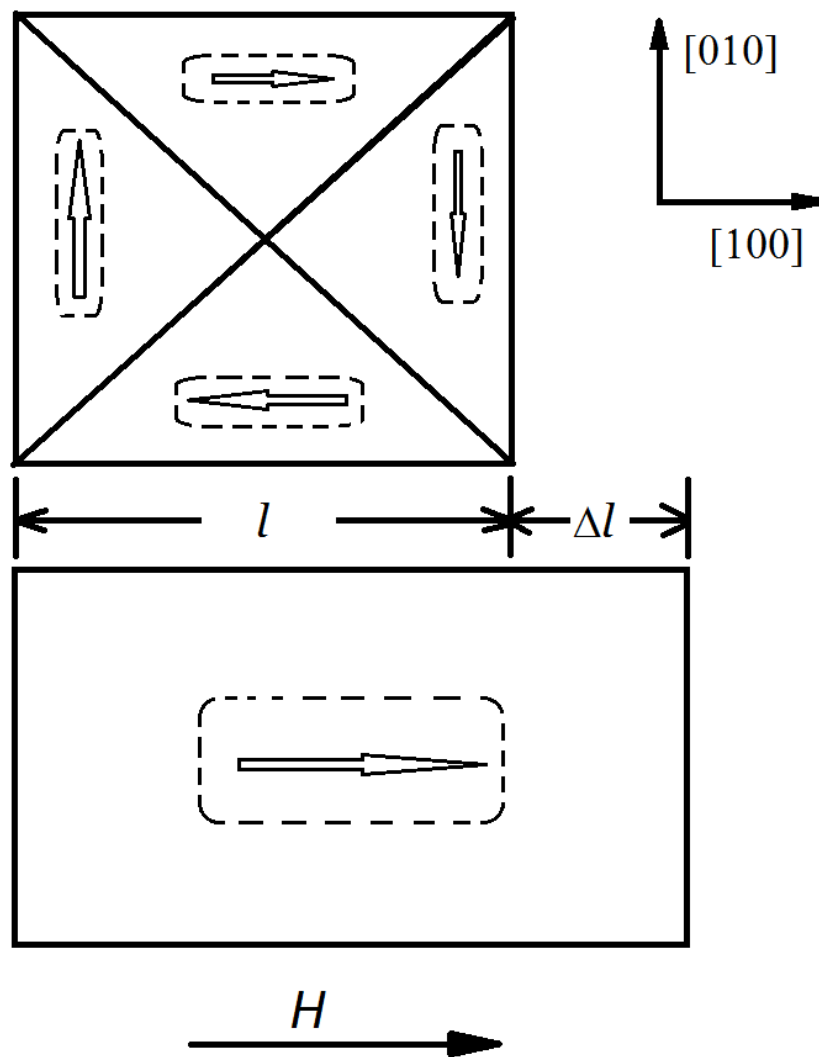
Fig. 2.11 indicates magnetostriction of an iron crystal in the [100] direction[3].

2.4.1 Measure λ on bulk or ribbon

The measurement of longitudinal magnetostriction is straightforward but not trivial, especially over a range of temperatures. While early investigators used mechanical and optical levers to magnify the magnetostrictive strain to an observable magnitude, today this measurement on bulk or ribbon samples is commonly made with an electrical-resistance strain gage cemented to the specimen. The gage is made from an alloy wire or foil grid, embedded in a

thin paper or polymer sheet, which is cemented to the sample. When the sample changes shape, so does the grid, and the change in shape also causes a change in the electrical resistance of the gage. With ordinary gages, the fractional change in resistance is about twice the elastic strain. This is typically a small resistance change, but one fairly easily measured with a bridge circuit, either ac or dc[3].
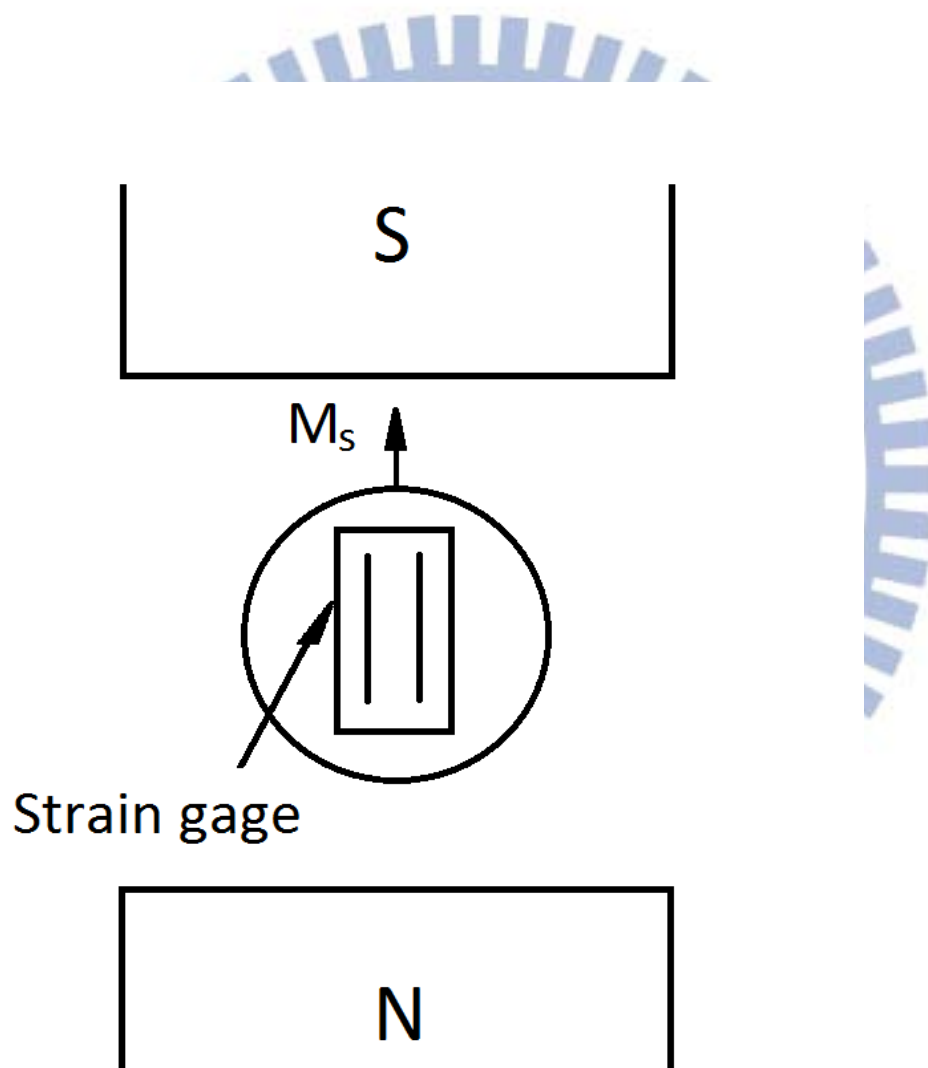
Fig. 2.12 Magnetostriction measurement on a sample (bulk or ribbon) using a strain gage[3].

2.4.2 Measure λ on thin film

Thin film samples present special challenges in the measurement of magnetostriction, since the films are almost always bonded to a nonmagnetic substrate.　If the substrate is thin enough, a change in dimension of the film may produce a measurable curvature in the substrate, from which the magnetostrictive strain can be deduced.　Another approach is to apply a known stress to the sample and measure the resulting change in magnetic anisotropy. This method demonstrates the concept of the stress anisotropy.
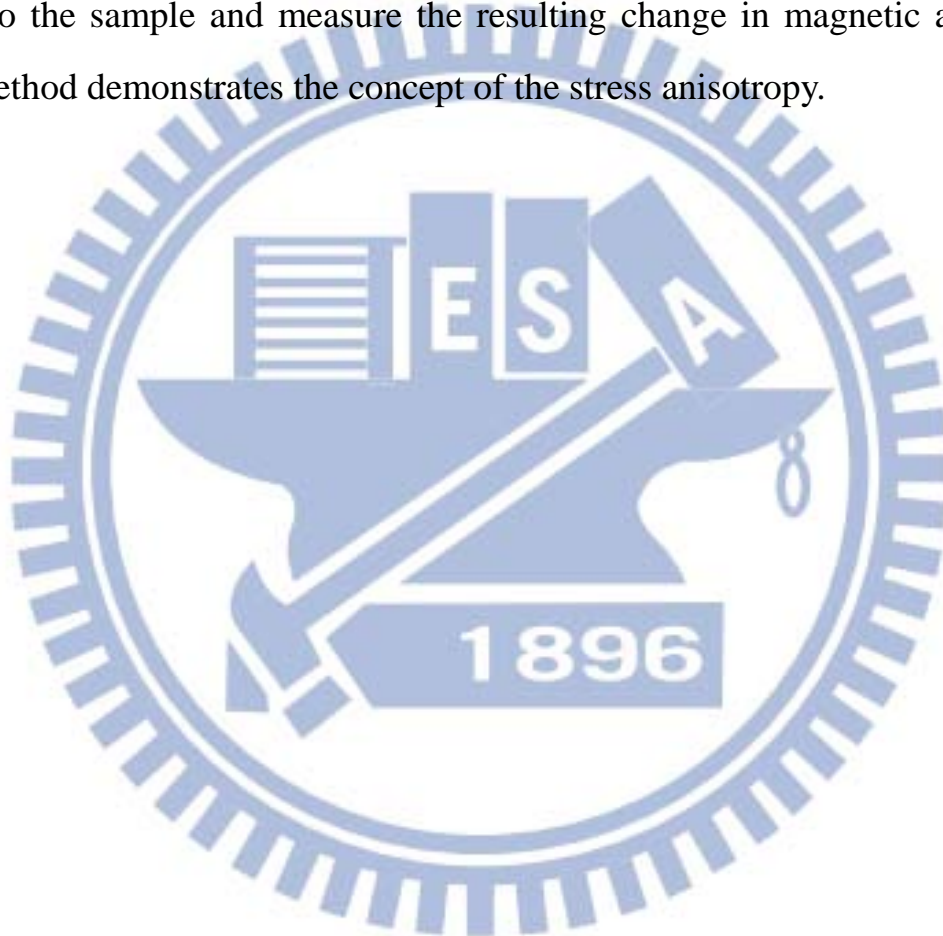
2.5 Ferromagnetic Resonance

Spin resonance in ferromagnetic metals, called simply ferromagnetic resonance, is complicated by eddy-current effects. At frequencies of about 10^{10} Hz, eddy-current shielding of the interior of the specimen is so nearly complete that the depth of penetration of the alternating field is only about 100 nm or 300 atom diameters. (Skin effect will be discussed in next section.) The specimen is therefore usually composed of powder particles of about this diameter, or of a thin film.

If the applied field is not large enough to saturate a ferromagnetic sample, resonance phenomena may still occur. Various nonuniform resonance modes may arise, by which different parts of the sample are magnetized in slightly different directions, each oscillating in resonance. There can also be domain wall resonance associated with small-scale oscillatory motion of domain walls. Many of these phenomena are discussed by C. Kittel[2, 16].

Energy losses at resonance frequencies, by which the oscillatory motion of the electron spins is converted to heat in the sample, determine the width of the resonance peak, the peaks in insulating samples can be very narrow: less than 1 Oe. In metals the peaks may be 1000 times broader[16]. The energy losses also control the speed with which a ferromagnetic material can reverse its direction of magnetization.

If there are no losses at all, or zero damping in the usual terminology, then the magnetization only precesses around the applied field and never becomes parallel to the field. And if damping is very large, the magnetization approaches the field direction very slowly, and switching time is hopelessly slow.

An intermediate level of losses, called critical damping, leads to the fastest switching[2, 16].

Curiously, the form of the equation that describes the damping is not obvious. If the damping is small compared to the precession, a formulation called the Landau-Lifshitz equation was proposed as early as 1935[3, 16]:

$$\frac{\partial \vec{M}}{\partial t} = -\gamma(\vec{M} \times \vec{H}) - \lambda \frac{\vec{M} \times (\vec{M} \times \vec{H})}{M^2} \qquad (2.12)$$

The first term is the precession motion, and the second term is the damping, with λ as an adjustable damping parameter. The constant $\gamma = ge/2m_ec$, where e and m_e are the charge and mass of electron, c is the velocity of light, and g is the g-factor (=2 for electron spin), respectively.

An alternative damping term was proposed by Gilbert, namely

$$-\frac{\alpha}{M}\left(\vec{M} \times \frac{d\vec{M}}{dt}\right), \qquad \text{where} \quad \alpha = \frac{\vec{M} \times (\vec{M} \times \vec{H})}{M^2}$$

Ref. [16] shows that the Landau-Lifshitz equation can be written in the form

$$\frac{\partial \vec{M}}{\partial t} = -\gamma(\vec{M} \times \vec{H}) + \frac{\alpha}{M}\left(\vec{M} \times \frac{d\vec{M}}{dt}\right) + \gamma\alpha^2(\vec{M} \times \vec{H}). \qquad (2.13)$$

If α is small, the term is negligible and equation 2.13 becomes the Gilbert equation. The full form of equation 2.13 can be called Landau-Lifshitz-Gilbert equation (LLG equation), as

$$\frac{\partial \vec{M}}{\partial t} = -\gamma(\vec{M} \times \vec{H}) + \frac{\alpha}{M}\left(\vec{M} \times \frac{d\vec{M}}{dt}\right) \qquad (2.14)$$

2.6 Skin effect

In high-frequency applications, the current in a good conductor tends to shift to the surface of the conductor, resulting in an uneven current distribution in the inner conductor and thereby changing the value of the internal inductances.   In the extreme case, the current may essentially concentrate in the "skin" of the inner conductor as a surface current, and the internal self-inductance is reduced to zero.

Then a high-frequency electromagnetic wave is attenuated very rapidly as it propagates in a good conductor.   The distance δ through which the amplitude of traveling plane wave decreases by factor of e^{-1} (= 0.368) is called the skin depth of a conductor[17]:

$$\delta = (\frac{\rho}{\pi \mu f})^{1/2} \qquad (2.15)$$

Where ρ is resistivity, f is microwave frequency, μ is permeability.

At microwave frequencies, the skin depth of penetration of a good conductor is so small that fields and currents can be confined in a very thin layer of the conductor surface.   For example, at 10 GHz it is a very small distance 0.66 μm for copper[17].

3. Experiments

3.1 Process

3.1.1 Samples for film
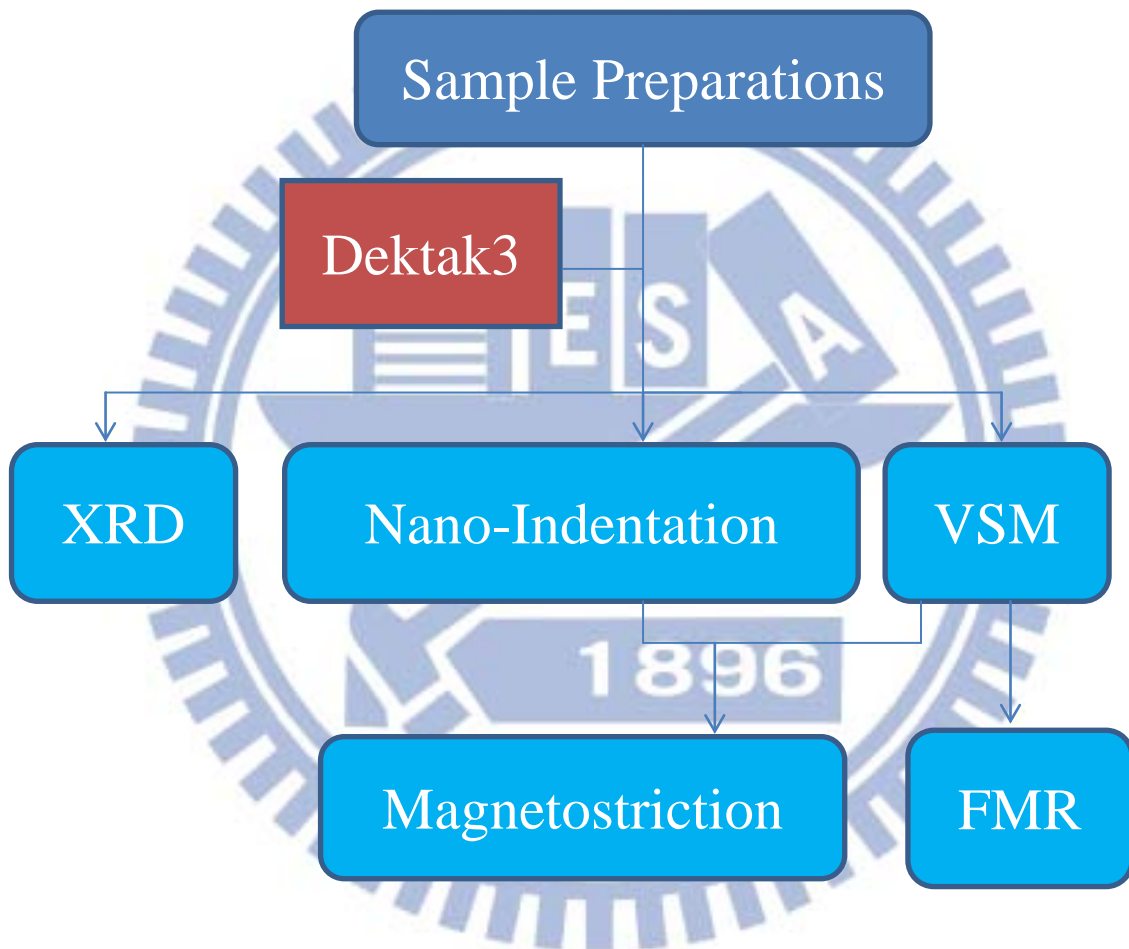
This is the flow chart of the experimental process.   We checked the film thickness by Dektak3.   The film's structure was shown in the X-ray diffraction data.   The Young's modulus of each film was obtained from the nano-indentation system.   The magnetization hysteresis was measured by VSM system.   Our main experiments are the magnetostriction hysteresis and FMR measurements.

3.1.2 Samples for ribbon
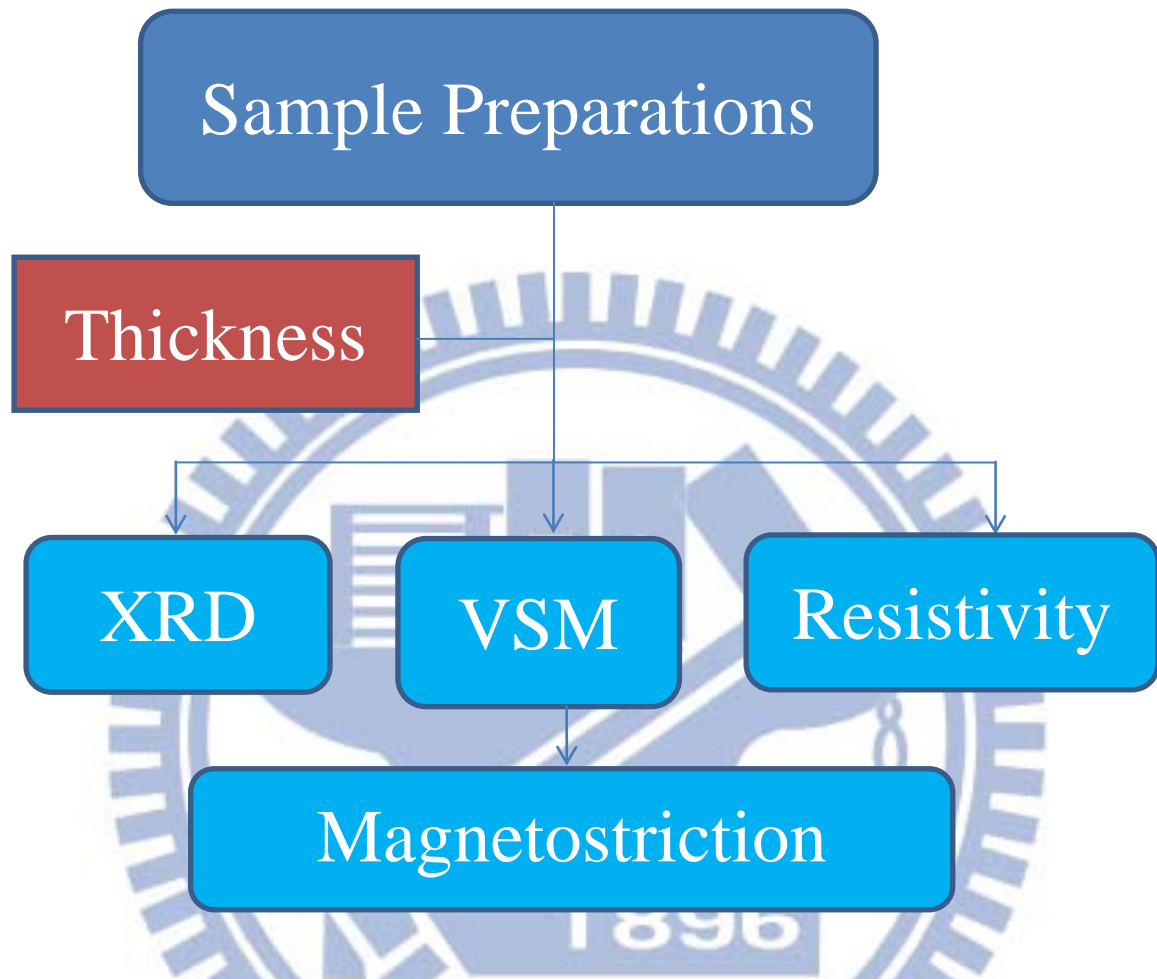
This is the flow chart of the experimental process. We checked the ribbon thickness by vernier. The ribbon's structure was shown in the X-ray diffraction data. The resistivity of each film was obtained from the van der Pauw method. The magnetization hysteresis was measured by VSM system. Our main experiments are the magnetostriction hysteresis measurements.

3.2 DC magnetron sputtering method

DC magnetron sputtering is a physical rather than a chemical or thermal process in making films in making films. Permanent magnets are used in the sputtering gun in order to shorten the ionization mfp for the displaced atoms that fly randomly inside the vacuum chamber. Then atoms are physically ejected from a target material by high-energy gas ions, usually argon ions[19, 20]. The arrangement is shown in Fig. 3.1. It is necessary to create plasma of ionized gas in the deposition chamber. The presence of stable plasma, created by the gas atoms, is a necessary[3].

The advantages of dc magnetron sputtering are[21]:

1. Multicomponent films can be deposited.
2. Refractor materials can be deposited.
3. Insulating films can be deposited.
4. Good film adhesion is assured.
5. Low-temperature epitaxy is possible.
6. Thickness uniformity over lager planar areas can be obtained.

The disadvantages are:

The source material must be available in sheet form.

+2 to 5 kV

Substrate

Target atoms

Ar ions

Argon gas

Air

Target

S	N	S
N	S	N

gun
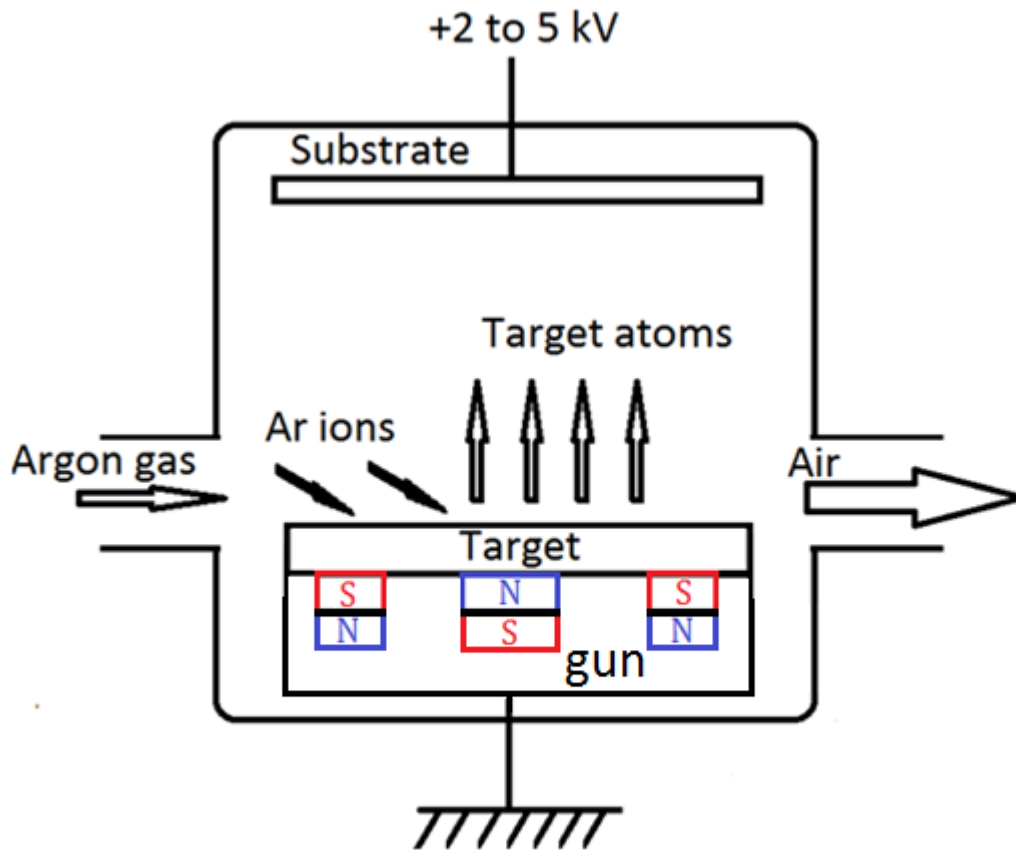
Fig. 3.1 Thin film prepared by dc magnetron sputtering.

3.2.1 Process conditions

A series of magnetic thin films, $Fe_{81-x}Ni_xGa_{19}/Si(100)$ and $Fe_{81-y}Ni_yGa_{19}/glass$ films, with x, y = 0, 4, 7, 11, 17, 22,and 26 at. % Ni, were deposited films by alloy targets and the dc magnetron sputtering method. The dc magnetron sputtering system is shown in Fig. 3.2, and the working conditions are listed as following:

1. The working gas (99.999% argon) pressure was 5 mTorr.

2. The sputtering power were 80W

3. The deposition temperature (TS) was at room temperature (RT).

4. The film thickness was 1000 Å.
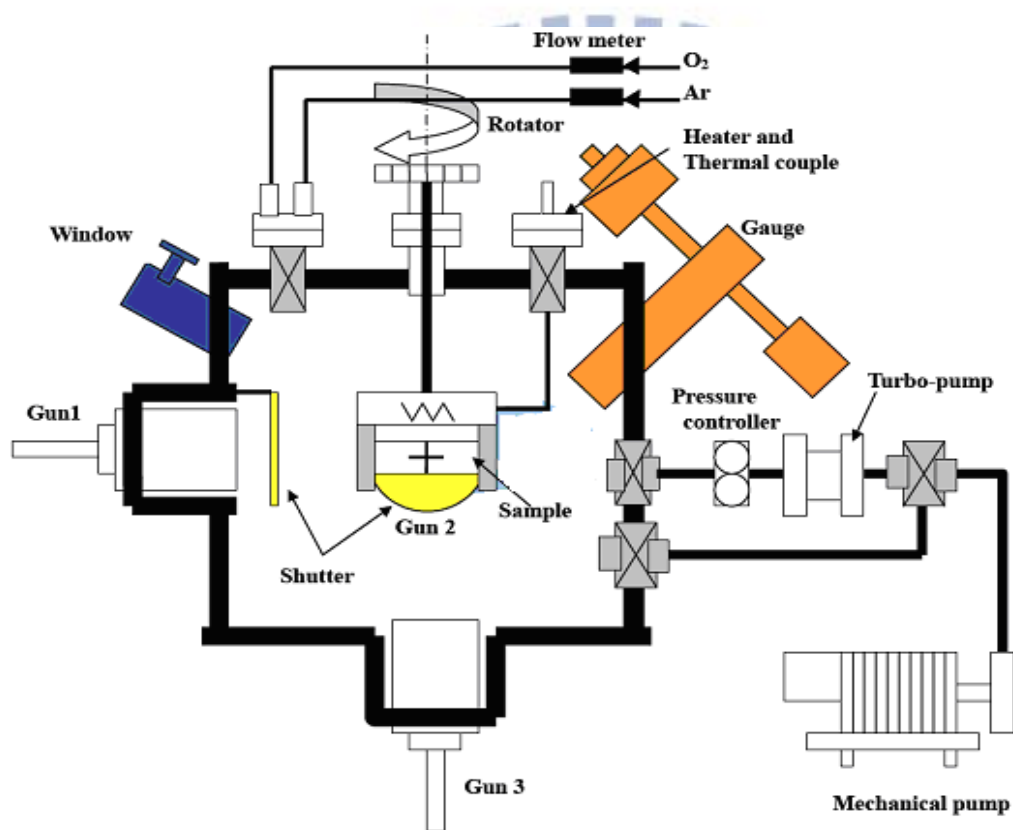
Fig. 3.2 shows schematics of the Sputtering system.

3.3 Rapid quenching melt-spun method

A series of magnetic metallic ribbons, $Fe_{81-z}Ni_zGa_{19}$ with $z = 0$, 3, 7, 13, and 24, were made by the rapid quenching melt-spun method in a low vacuum chamber, the arrangement is shown in Fig. 3.3[3, 22]. The surface velocity of the rotating copper wheel was about 15m/s. The average thickness (t) of the ribbon is about 0.03 mm and the width (w) is about 4mm, which is shown in Fig. 3.4.
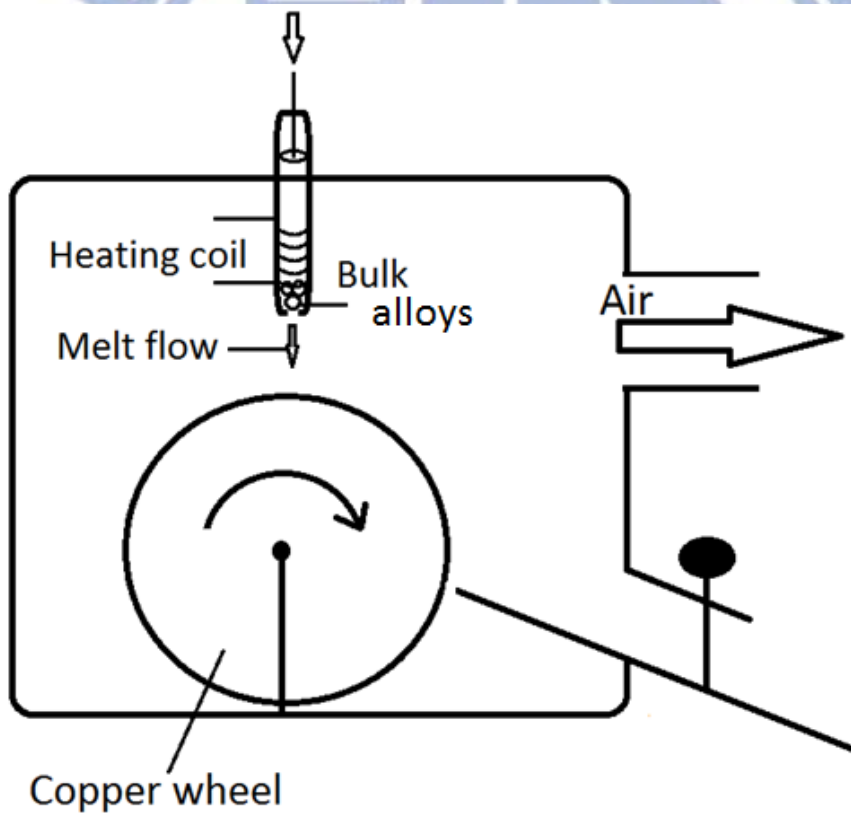
Fig. 3.3 Ribbons preparation by rapid quenching melt-spun.

Fig. 3.4 The samples of ribbon are made by the rapid quenching melt-spun method.
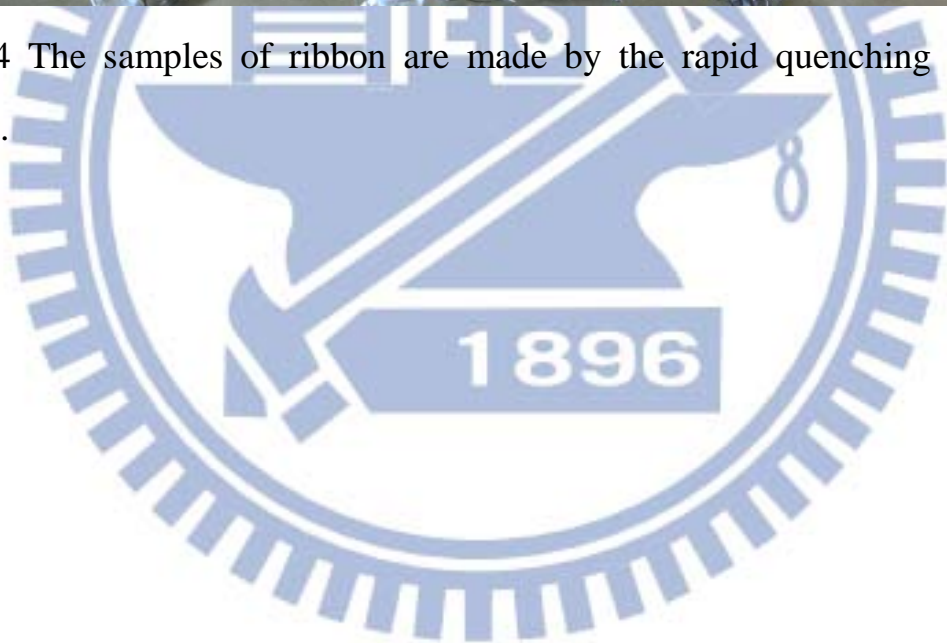
3.4 The Dektak[3] system

The Dektak[3] system is a high precision measuring system which accurately measures surface texture, shown in the Fig. 3.5. Table 3.1 is the technical specifications for Dektak[3] system.

3.4.1 Principle of operation

There is the mobile diamond-tipped stylus on Dektak[3] to measure the surface texture of the sample. The high precision stage moves a sample beneath the stylus according to a programmed scan length and speed. The stylus on the stage is mechanically coupled to the core of a linear variable differential transformer (LVDT). As the stage moves the stylus on the sample, the stylus rides over the sample surface. The stylus is translated vertically on the surface variations. The information with electrical signals depending on the stylus movement is produced as the core position of the LVDT changes respectively. An analog signal proportional to the position change is produced by the LVDT, which in turn is conditioned and converted to a digital format through a high precision, integrating analog to digital converter. The results of the digitized signals from a single scan are stored in computer memory for display, manipulation, and measurement, the process figure is shown in Fig. 3.6[23].

ILLUMINATION SWITCH

ROTARY STAGE

X THUMBWHEEL

ROUGH LEVELING

FOCUS KNOB

ZOOM OPTICS

FINE FOCUS

Y THUMBWHEEL
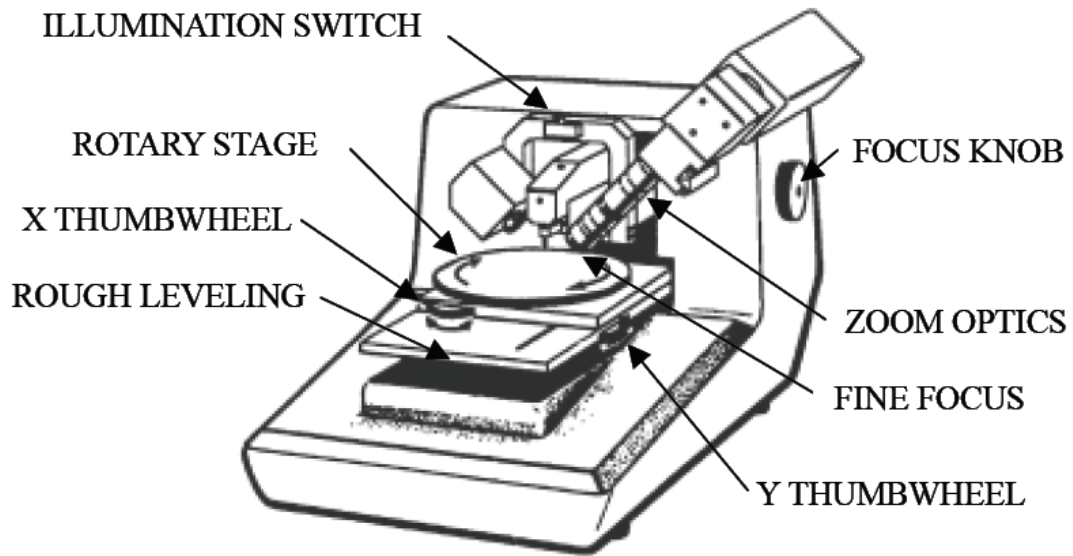
Fig. 3.5 shows Dektak[3] system[23].

Table 3.1 Technical specifications[23]

Vertical data resolution	5 Å maximum
Vertical range	65.5 μm maximum
Scan length range	50 μm to 30 mm
Stylus tip radius	12.5 μm standard
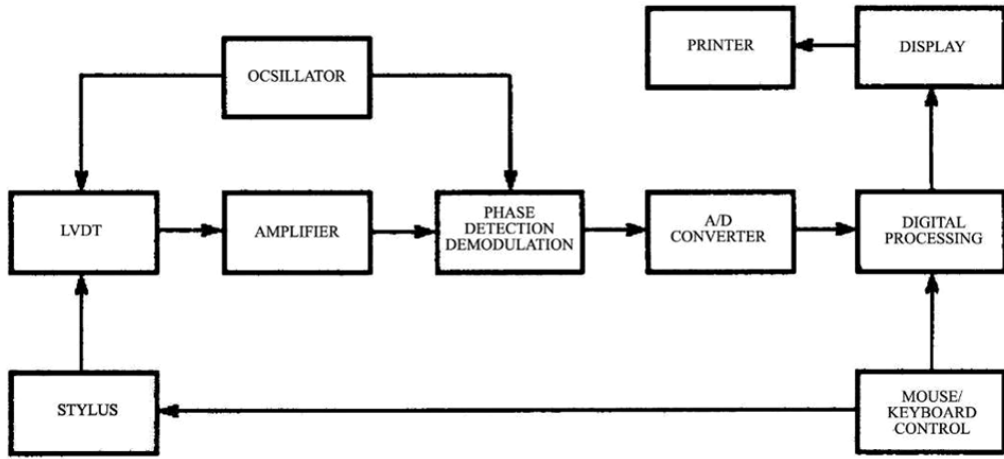
Fig. 3.6 Block diagram of Dektak[3] architecture[23].
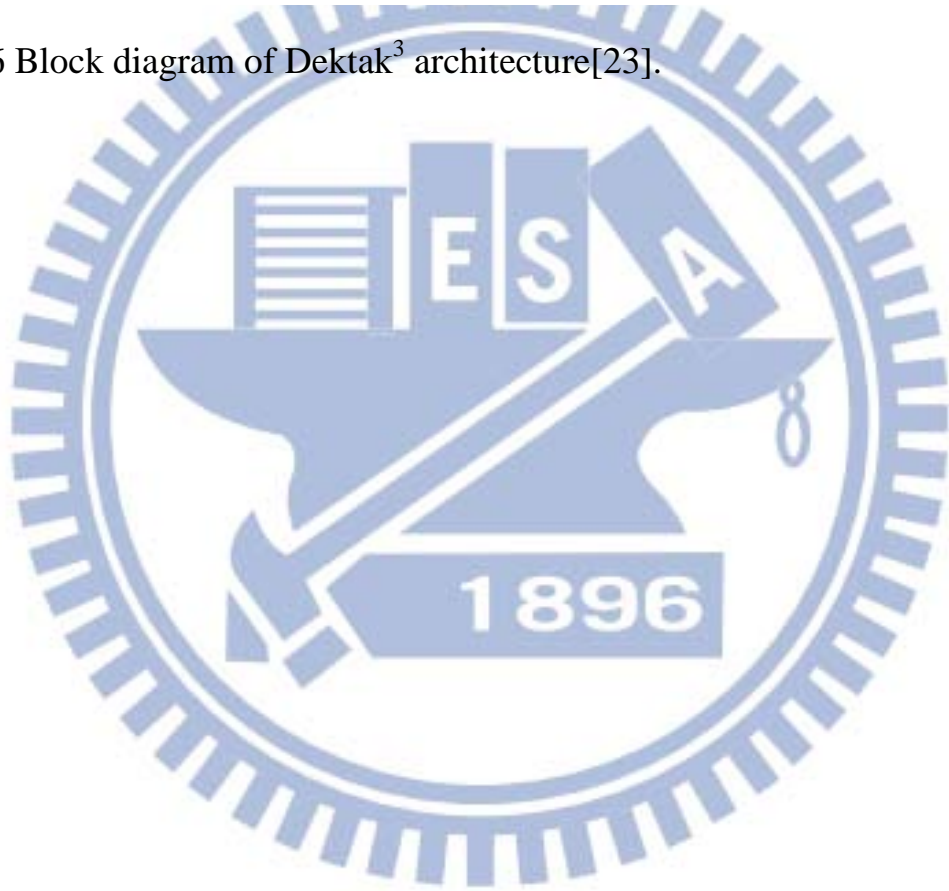
3.5 X-ray diffraction (XRD)

Fig. 3.7 shows the incoming beam let each scatterer to re-radiate a small portion of its intensity as a wave. Then scatterers are arranged symmetrically with distance d, these waves will be in sync (add constructively) only in directions where their path-length difference $2d\sin\theta=n\lambda$, called Bragg's law[26].

In this study, the structural properties were characterized by the X-ray diffraction (XRD) using CuKα1 line ($\lambda = 1.5405$ Å). There are shown typical x-ray diffraction patterns in Fig. 3.8 and Fig. 3.9, and other results are shown in chapter 7 appendix.

$\lambda = 1.5405$ Å
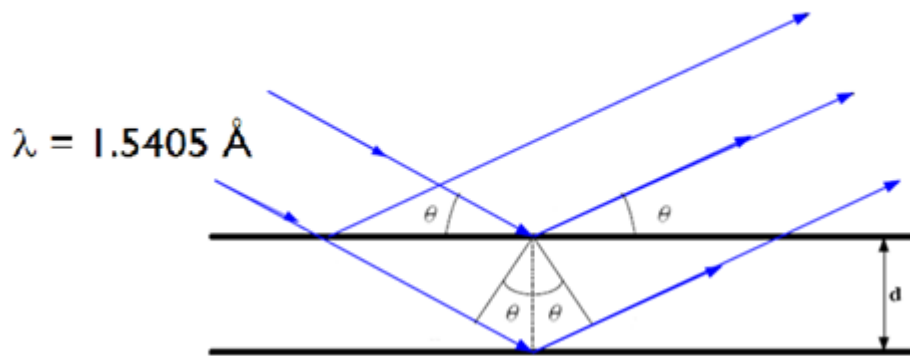
Fig. 3.7 The schematic illustration of Bragg's law.
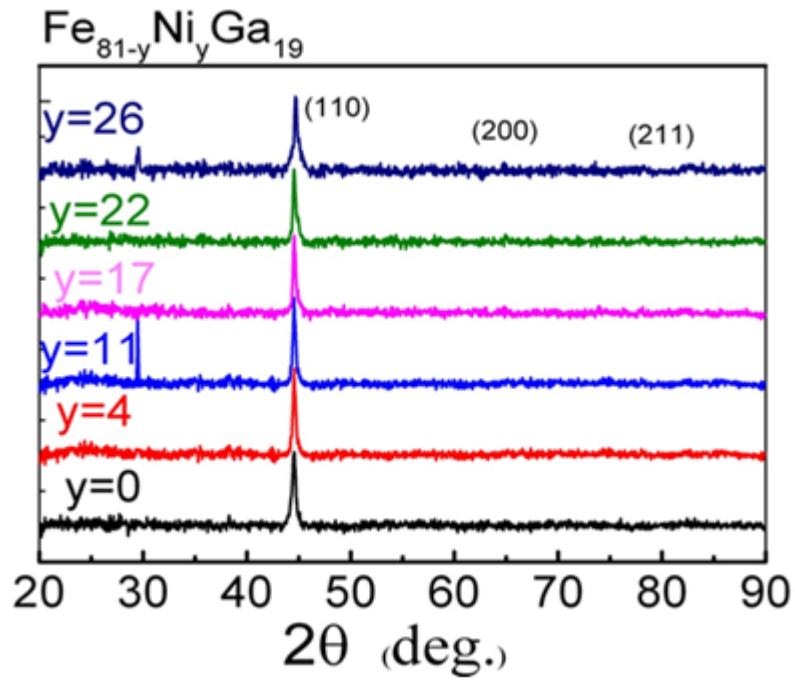
Fig. 3.8 The X-ray diffraction figure on series of $Fe_{81-y}Ni_yGa_{19}$/glass films.
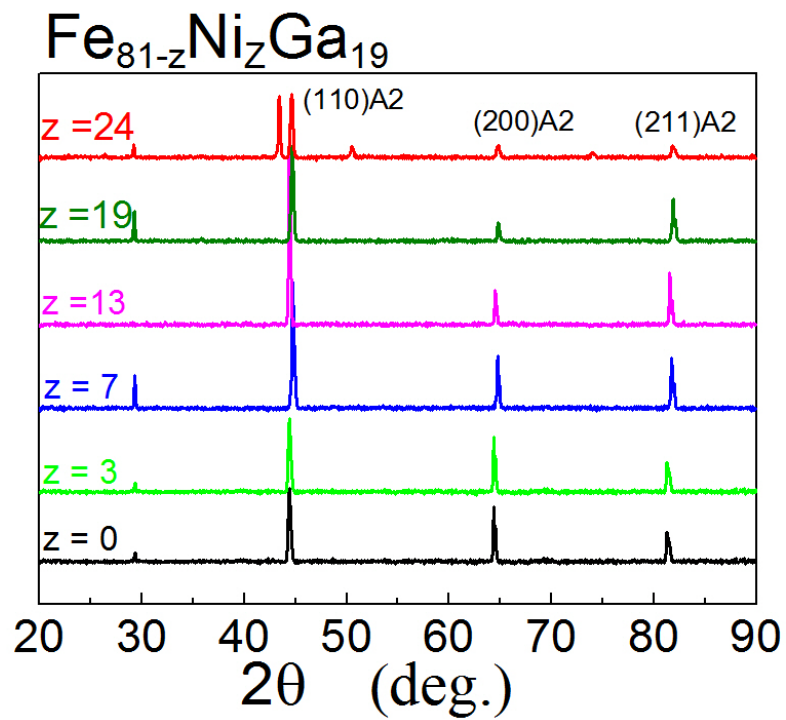
Fig. 3.9 The X-ray diffraction figure on series of $Fe_{81-z}Ni_zGa_{19}$ ribbons.

3.6 Nano-indentation system measure

The Young's modulus (E_f) of the each film was obtained from the nano-indentation system, which is shown in Fig. 3.10. From each indentation cycle, the depth of circle of contact (h_p) is obtained. For details of the h_p measurement, please refer to Ref. [24]. From a series of indenting tests (i.e., from heavy to light loadings) we can plot the measured E as a function of h_p. Usually, E_f is taken in the h_p range, where $h_p = t_f/15$ to $t_f/10$. Alternatively, the following empirical equation is used for fitting [25, 27]:

$$E = E_s + (E_f - E_s)e^{-\frac{h_p}{t^*}} ,$$
(3.1)

where E_S is the Young's modulus of the substrate, and t* is a fitting parameter. The solid curves in Fig. 3.11 show the best-fit results, by using Eq. 3.1, for all the $Fe_{81-y}Ni_yGa_{19}$/glass films. When $h_p > 0.05$ μm in Fig. 3.11, E tends to approach a fixed value, i.e., $E_S \cong 76$ GPa [8], of the 0211 Corning glass substrate. The E vs. h_p fitting plots for the $Fe_{81-x}Ni_xGa_{19}$/Si(100) films look similar to Fig. 3.11, except that all the plots are shifted upward, with $E_S \cong 130$ GPa for the Si(100) substrate[27].

Fig. 3.10 Nano-indentation system.
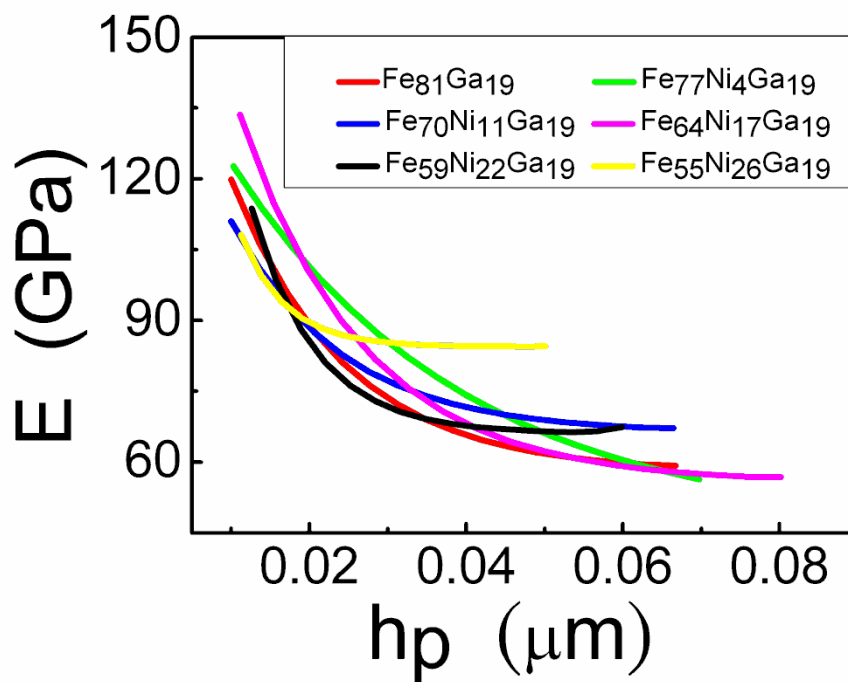
Fig. 3.11 Solid curves represent the best-fit results of E vs. h_P, where E is the Young's modulus and h_p is the depth of circle of contact, obtained from the nano-indentation measurements, for the Fe-Ni-Ga/glass films[27].

3.7　Electrical resistivity measurement

In this study, we measured the electrical resistivity (ρ) by the collinear four-probe array, which is shown in Fig. 3.12.　ρ is calculated by the equation as,

$$\rho = \frac{\frac{1}{2} \times (V_+ - V_-)}{I} \times \frac{tW}{L} \times C \qquad (3.2)$$

where V_+ means V_2-V_1 for +I, V_- means V_2-V_1 for -I, ρ is in unit of $\mu\Omega$-cm, and C is a correction factor, dependent on both the ratios W/L and ℓ/W[28].　Table 3.2 shows the calculated dependence of the correction factor C on W/L and ℓ/W. In our case, C $\fallingdotseq$ 1.
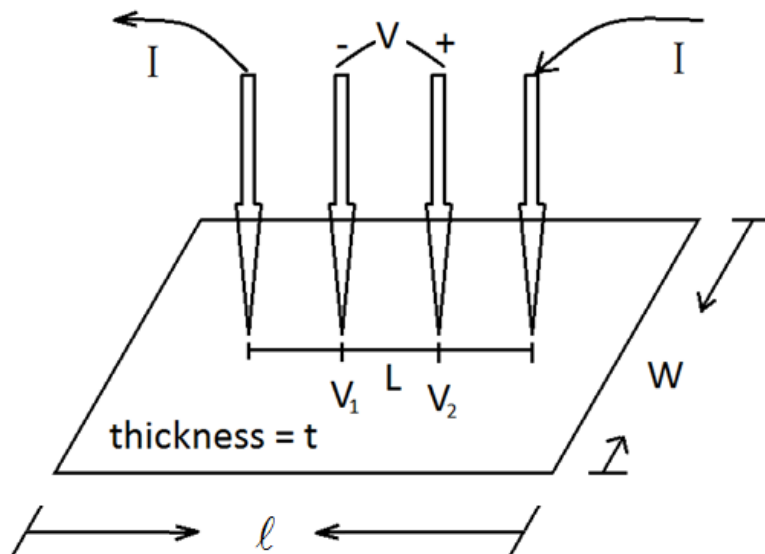
Fig. 3.12 The resistivity measured by the collinear four-probe array.

Table 3.2 Correction factor C for the calculation of the resistivity measured with collinear four-point probes placed on a symmetry axis[28].

W/L	Circle	Square	Rectangle	Rectangle	Rectangle
	C for dia. d	C for $\ell/W=1$	C for $\ell/W=2$	C for $\ell/W=3$	C for $\ell/W=4$
1.0				0.9988	0.9994
1.5			1.4788	1.4893	1.4893
2.0			1.9454	1.9475	1.9475
3.0	2.2662	2.4575	2.7000	2.7005	2.7005
4.0	2.98289	3.1137	3.2246	3.2248	3.2248
5.0	3.3625	3.5098	3.5749	3.5750	3.5750
10.0	4.1716	4.2209	4.2357	4.2357	4.2357
20.0	4.4364	4.4516	4.4553	4.4553	4.4553
∞	4.5324	4.5324	4.5324	4.5324	4.5324

3.8　Ferromagnetic resonance (FMR) experiments

　　The cavity used was a Bruker ER41025ST X-band resonator which was tuned at f_R = 9.6 GHz.　The films were oriented such that EA//$\vec{H}_z$ and EA $\perp \vec{h}_{rf}$. The EA means easy-axis.　Where $\vec{H}_z$ was an in-plane external field, which varied from 0 to 2 kOe, and $\vec{h}_{rf}$ was the microwave field, ω is angle velocity for z-axis, and z-axis is EA of the film.　Configuration is depicted schematically in Fig. 3.13.　A typical FMR absorption spectrum of the $Fe_{59}Ni_{22}Ga_{19}$/glass film is shown in Fig. 3.14, where we can spot an FMR event manifested by an absorption peak at H = H_R and define the half-peak width $(\Delta H)_{exp}$.　In this case, H_R = 671.4 Oe and $(\Delta H)_{exp}$ = 133.9 Oe were obtained[29].
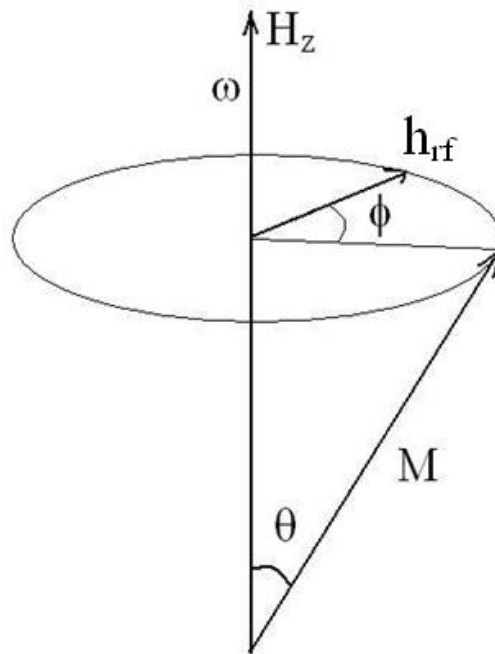
Fig. 3.13 Ferromagnetic resonance model.
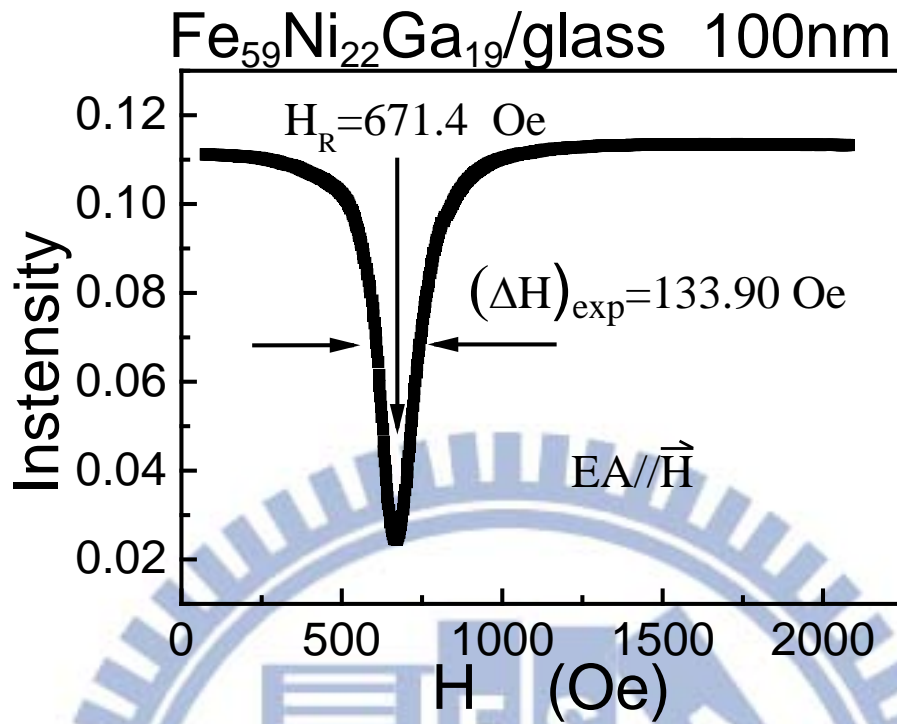
Fig. 3.14 A typical FMR absorption spectrum of the $Fe_{59}Ni_{22}Ga_{19}$/Glass film at the microwave frequency f = 9.6 GHz.

3.9 Vibrating-Sample Magnetometer (VSM)

Fig. 3.15 shows the vibrating sample magnetometer used for measuring the magnetization as a function of applied field.   It is based on the flux change in a coil when a magnetized sample is vibrating nearby.   The sample, commonly a small disk, is attached to the end of a nonmagnetic rod, the other end of which is fixed to a loudspeaker cone or to some other kind of mechanical vibrator.   The oscillating magnetic field of the moving sample induces an alternating emf in detection coils, whose magnitude is proportional to the magnetic moment of the sample.   The alternating emf is amplified, usually with a lock-in amplifier which is sensitive only to signals at the vibration frequency.   The lock-in amplifier must be provided with a reference signal at the frequency of vibration, which can come from an optical, magnetic, or capacitive sensor coupled to the driving system.   The detection-coil arrangement usually involves balanced pairs of coils to cancel signals due to variations in the applied field.   The apparatus is calibrated with a specimen of known magnetic moment, which must be of the same size and shape as that of the sample to be measured, and should also be of similar permeability[3].

The driving system may be mechanical, through a cam or crank and a small synchronous motor, or in a recent commercial instrument, with a linear motor. In our case, shown in Fig. 3.16, the vibration frequency is generally below 85 Hz, and the vibration amplitude is a few millimeters.   The amplitude is fixed by the geometry of the mechanical system or by the drive signal delivered to the linear motor.   The amplitude may vary, depending on the mass of the sample and/or the frequency of vibration.   One method is to and a second set of

sensing coils. Then the signal from these coils can be used in the feedback loop to maintain constant amplitude of vibration. Alternatively, a portion of the signal from the permanent magnet can be balanced against the signal from the unknown sample, making the method a null method[30].

Extreme care is necessary to minimize vibration of the sensing coils in the field, and to prevent the measuring field from influencing other parts of the system. Note that the VSM measures the magnetic moment m of the sample, and therefore the magnetization M can be obtained.
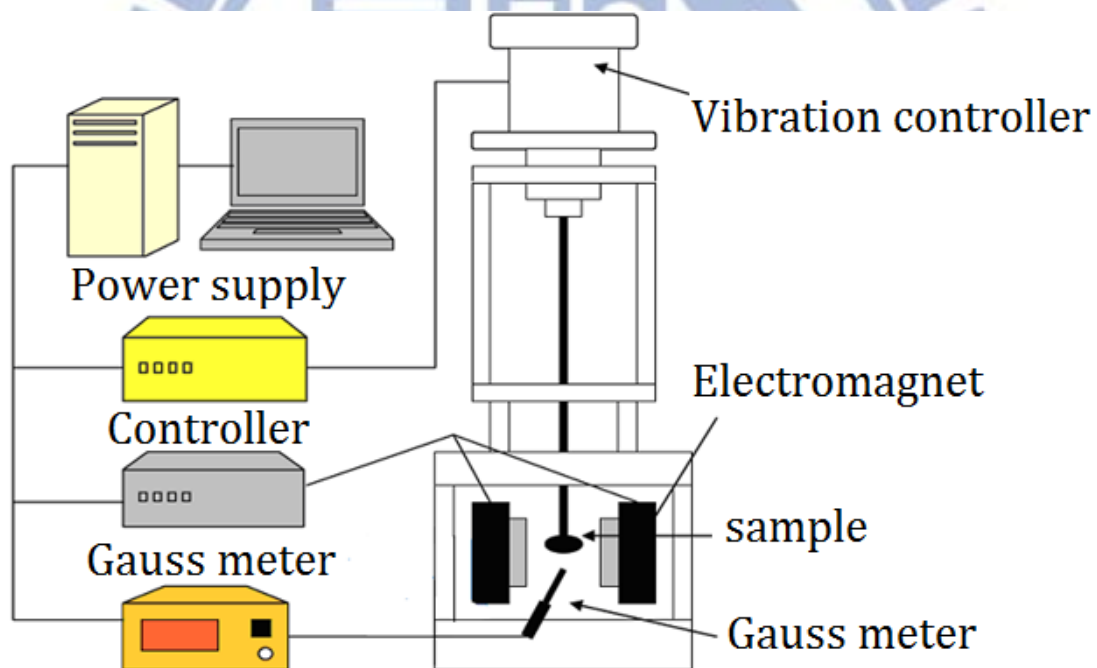
Fig. 3.15 Vibrating sample magnetometer (VSM) model.
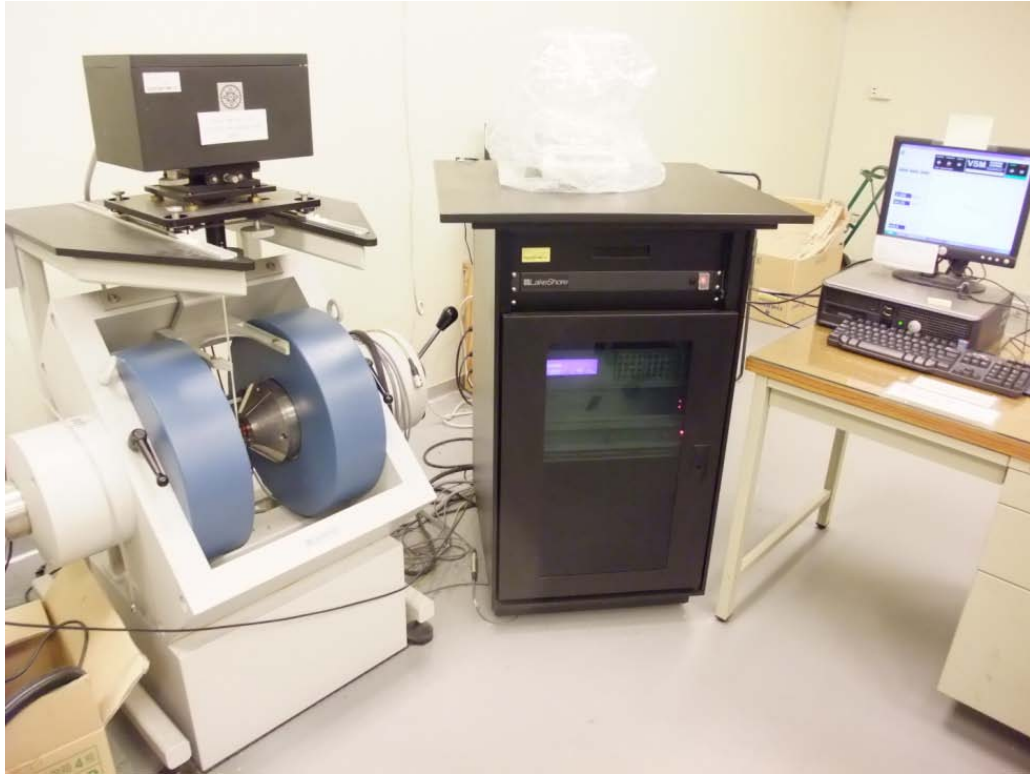
Fig. 3.16 Vibrating-Sample Magnetometer (VSM). Courtesy Lake Shore Cryotronics, Inc.

3.9.1 Measuring hysteresis loops

The field-in-plane magnetic hysteresis loops were obtained by varying sample orientation with respect to the applied field in the vibrating sample magnetometer (VSM) measurements to indentity the easy-axis (EA) and hard-axis(HA)[29]. When the squareness ratio (SQR $\equiv M_r/M_S$) is the largest, the corresponding orientation is defined the EA. Similarly, the orientation with the smallest SQR is identified as the HA. A typical example is shown in Fig. 3.17. In most cases, the angular dependence of SQR is roughly sinusoidal with a period of 180°. For the more, the HA hysteresis loop of the

Fe$_{55}$Ni$_{26}$Ga$_{19}$/glass film in Fig. 3.18(a) shows that (SQR)$_{HA}$ = 0.72, H_S = 20 Oe, and the anisotropy field ($H_K \equiv (1/2)(H_{K1} + H_{K2}) \approx 6.3$ Oe). For the same film, its EA hysteresis loop in Fig. 3.18(b) shows that the saturation magnetization ($4\pi M_S \approx 15.8$ KG), (SQR)$_{EA}$ = 0.99, and coercivity ($H_C \approx 13.8$ Oe). Here, it is interesting to note that since $H_K \leqq H_C$ for all the films, they may be classified as the "inverted" films[31]. A brief summary is listed below: as x or y increases from 0 to 26, $4\pi M_S$ remains almost constant, 16.8–15.8 KG, and H_C decreases, 34.4–13.8 Oe, and the reasons would be discussed in next chapter.
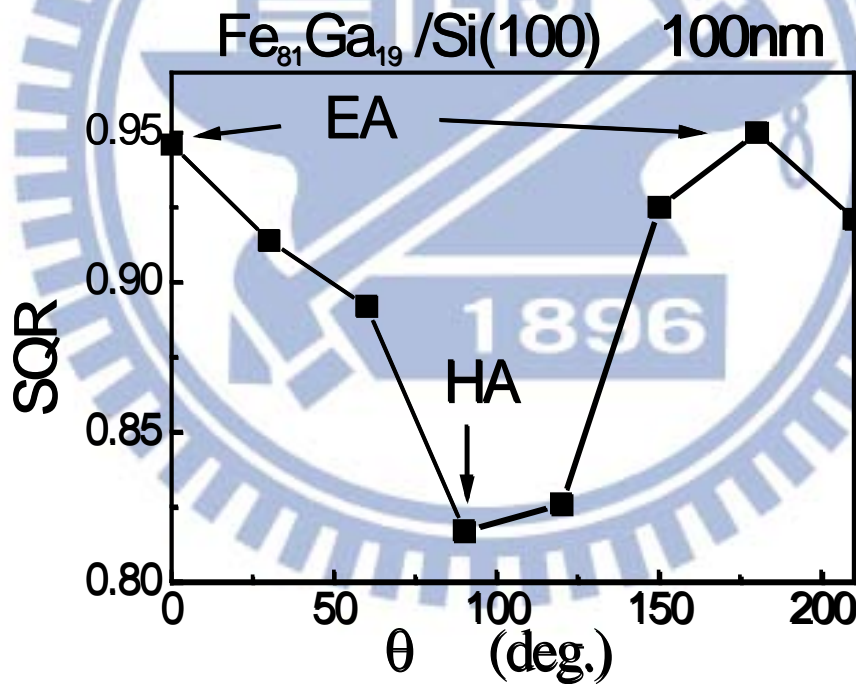
Fig. 3.17 The in-plane rotation SQR data of the Fe$_{81}$Ga$_{19}$/Si film.
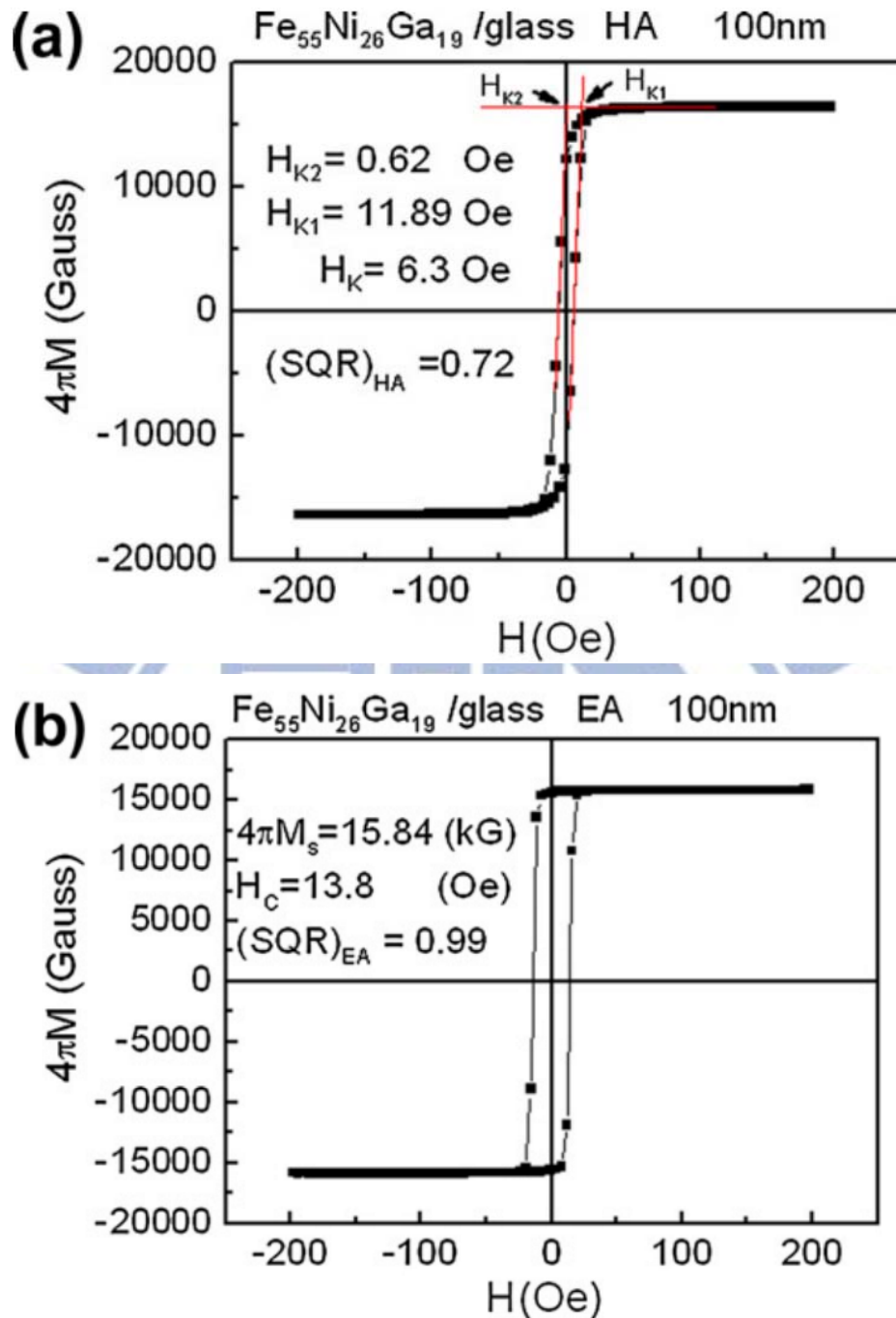
Fig. 3.18 (a) The hard-axis (HA) and (b) the easy-axis (EA) magnetic hysteresis loop of the $Fe_{55}Ni_{26}Ga_{19}$ film deposited on a glass substrate. HK is the anisotropy field, $4\pi M_S$ is the saturation magnetization, H_C is the coercivity, and $(SQR)_{HA}$ and $(SQR)_{EA}$ are the squareness ratio along HA and EA, respectively.

3.10 Magnetostrictions

3.10.1 Optical-cantilever magnetostriction experiment for films

The longitudinal and transverse magnetostrictions ($\lambda_\parallel$ and $\lambda_\perp$) were measured in an optical-cantilever system[32], as depicted schematically in Fig. 3.19 and Fig. 3.20. The light source was a helium-neon laser. The laser beam was reflected from the sample tip and re-directed on to the position sensitive detector (PSD). Such that the magnetostriction induced are measured[29]. We used the x-direction and y-direction Helmholtz coils to generate the external fields. The obtained data are substituted into the following expression Ref. [33] to calculate the magnetostriction λ_s:

$$\lambda_s = \frac{2}{9}\left[\frac{\Delta_{\parallel S} - \Delta_{\perp S}}{L^2}\right]\left(\frac{E_s}{E_f}\right)\left(\frac{t_s^2}{t_f}\right)\left(\frac{1+\nu_s}{1+\nu_f}\right), \tag{3.3}$$

where L is the sample (or cantilever) length, ν_S is the Poisson ratio of the substrate, and ν_f is the Poisson ratio of the films, $\Delta_{\parallel S}$ or $\Delta_{\perp S}$ is the deflection, $\Delta_\parallel$ or $\Delta_\perp$, of the free end of the cantilever, when the in-plane longitudinal ($H_\parallel$) or transverse field ($H_\perp$) is above H_S. Here, ν_S is 0.23 for glass, 0.40 for Si(100), $\nu_f = 0.22$ for all the metallic Fe-Ni-Ga films, and t_S of double-side polished Si(100) or glass is particularly thin, about 110 μm. Typical magnetostriction hysteresis loops of the $Fe_{59}Ni_{22}Ga_{19}$/Glass film (with $t_f = 110$ nm) are shown in Fig. 3.21, giving $\lambda_S \approx 27$ ppm and $H_S \approx 15$ Oe in the case, respectively.
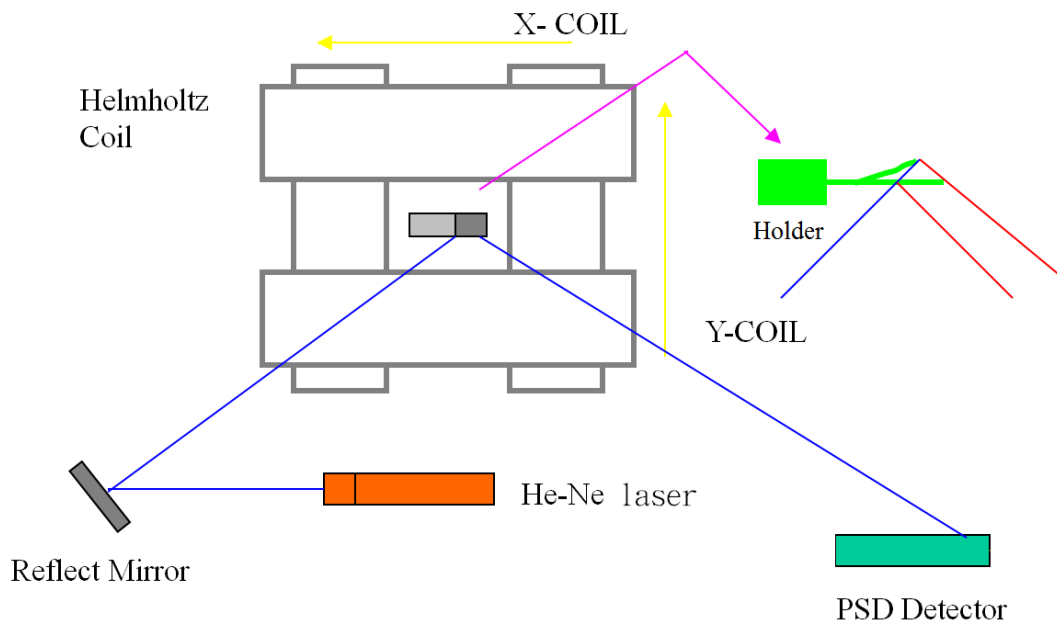
Fig. 3.19 Optical-cantilever magnetostriction experiment system.

1、 horizontal plate

2、X- COIL

3、Y-COIL

4、holder

5、foothold
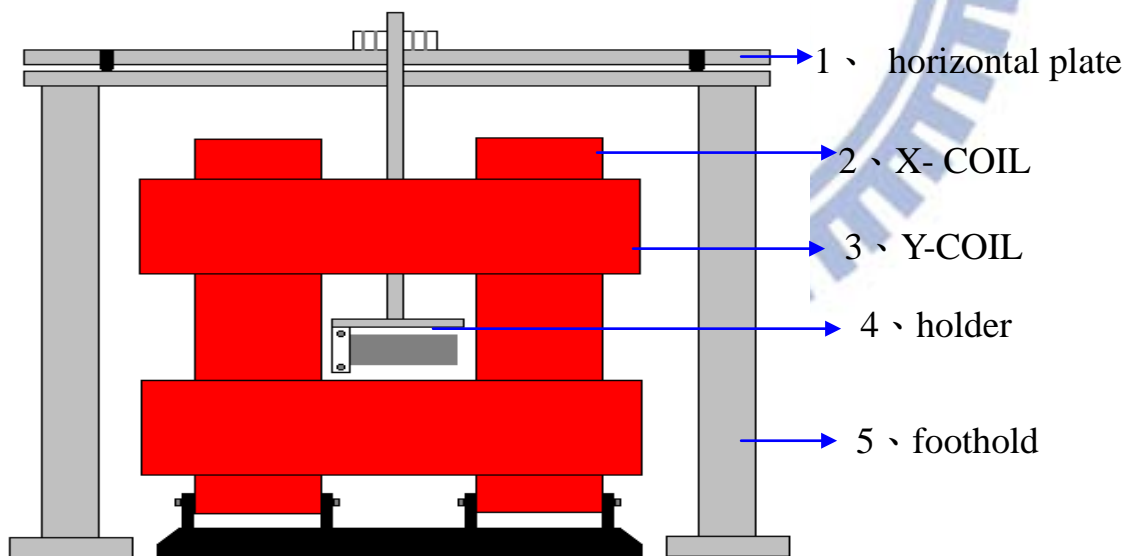
Fig. 3.20 The x-direction and y- direction Helmholtz coils.
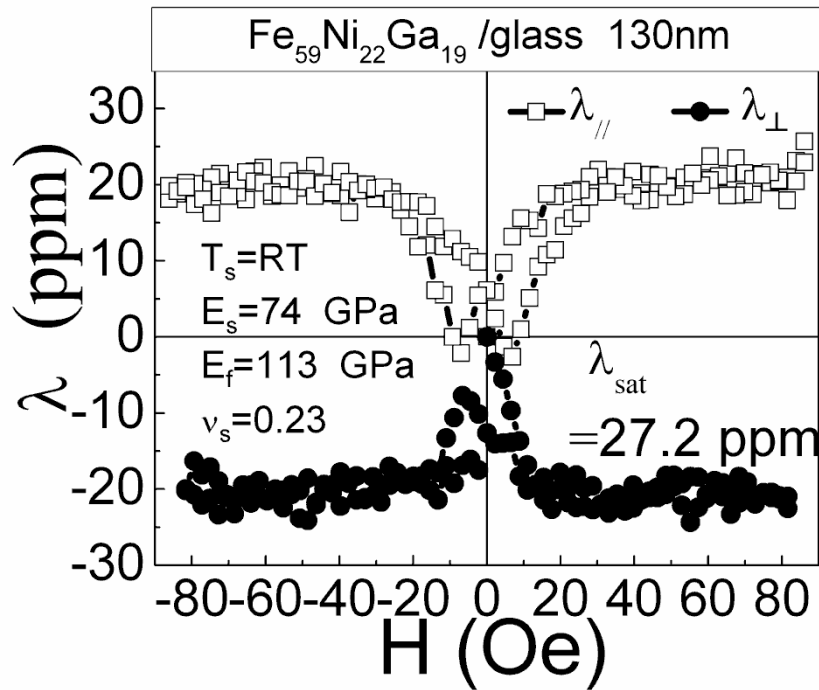
Fig. 3.21 Typical hysteresis loops for longitudinal and transverse magnetostrictions ($\lambda_{\parallel}$ and $\lambda_{\perp}$) of the $Fe_{59}Ni_{22}Ga_{19}$/glass film plotted as a function of the external field H.

3.10.2 Magnetostriction experiment for a ferromagnetic ribbon sample

In this study, we measured the saturation magnetostriction of a thin ribbon by the strain gauge method was used for our λ measurements[22, 34-36].   The gauge is cemented directly onto the surface of the ribbon sample under test, so that a small change in length are detected the change in the resistance (R) of the gauge.   Bearing these considerations in mind, we used the experimental set-up shown in Fig. 3.22, which is similar to that used in Ref. 37.   The ribbon sample was clamped by both ends on a brass sample holder; the xy-plane was parallel to

the ribbon. A horizontal in-plane field H_E was applied along the $\pm$ x directions from an electromagnet. The lower-end clamp could slide freely downward or along the y direction by hooking various standard weights over the aluminum ring. Thus, while the ribbon sample was stretched by the weight, it was also guided by two vertical brass rods alongside the ribbon. In this way, we could minimize the twisting and/or bending effects, which can cause spurious signals during the λ_S measurements. The gauge sensitivity is defined as the relative change in resistance per relative change in length, or the gauge factor, K= $(\Delta R/R)/(\Delta L/L)$. The gauge factor is given by

$$K = 1 + \nu + L\frac{d\rho}{dL} \qquad (3.4)$$

where L is the total length of the metal or semi-conductor wire the gauge, ΔR is the resistance change, due to the length ΔL, ν is Poisson's ratio for the wire material, ρ is the resistivity. The strain gauge used was a CEA-13-125UN-120 type with K=2.0-2.2, purchased from Vishay Intertechnology, Inc. When H_E=0, we could measure the external stress strain (σ-$\Delta\varepsilon$) curve plot for each ribbon sample. From the obtained σ-$\Delta\varepsilon$ curves, it is easy to obtain the E_S and $\Delta E/E_0$, where $\Delta E = E_S - E_0$, E_S is the Young's modulus of the sample in the magnetically saturated state, and E_0 is that in the demagnetized state[3, 38].
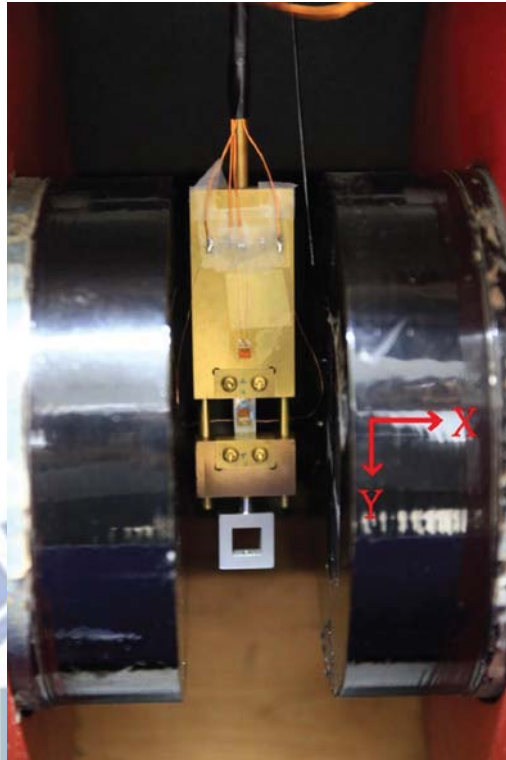
Fig. 3.22 A photo of the experimental set-up for the stress-strain (σ-Δε) and magnetostriction (λ) measurements.

4. Results and discussion for films

4.1 XRD data

Table 4.1 lists the x-ray structure data of the $(FeNi)_{81}Ga_{19}$ films deposited on glass substrates.   Briefly speaking, when y = 22 at.%Ni, there is only one single A2 phase, and when y =0, 4, 11, and 17 at.%Ni, there are mixed phases with A2 (major) and $D0_{19}$ and/or $L1_2$ phases (minor).   It is evident that all the FeNiGa films are highly (110) textured.

Table 4.1 Structural properties, the x-ray diffraction peaks, of the $Fe_{81-y}Ni_yGa_{19}$/glass films. I/I_{max} is the peak intensity ratio.   a is the lattice constant.

y (at.%Ni)	2θ (deg.)	phase (hkl)	d (Å)	a (Å)	I/I_{max} (%)
	38.3	$D0_{19}(200)$	2.348	----	14.5
0	44.57	A2(110)	2.031	2.873	100
	82.421	A2(211)	1.169	----	10.6
	38.234	$D0_{19}(200)$	2.352	----	10.4
4	44.537	A2(110)	2.033	2.875	100
	82.124	A2(211)	1.173	----	5.6
11	24.374	$L1_2(100)$	3.649	3.649	17
	44.57	A2(110)	2.031	2.873	100
17	24.011	$L1_2(100)$	3.703	3.703	17
	44.57	A2(110)	2.031	2.873	100
22	44.537	A2(110)	2.033	2.875	100
26	44.669	A2(110)	2.027	2.867	100

4.2 FMR data

Fig. 4.1 shows the main resonance field (H_R) at $f_R = 9.6$ GHz as a function of the Ni concentration (x or y) for the two series of $(FeNi)_{81}Ga_{19}$ films, respectively. From this figure, we find that H_R increases as x or y increases. In general, addition Ni replace Fe at.% in alloys to be caused reduced magnetic in rich-Fe alloys. Then needs higher resonance field at the same f_R as x or y increases.

When at the Kittel mode resonance, the relationship among H_R, H_K, f_R, and $4\pi M_s$ for a flat film can be written as[16, 39],

$$(f_R/v)^2 = H_R{}^2 + (2H_K + 4\pi M_S) H_R + H_K (H_K + 4\pi M_S). \qquad (4.1)$$

where $g = f_R/(1.40*x) = v/1.40$ represents the g-factor of the material, and $v = \gamma/2\pi$ is the gyromagnetic ratio. Hence, based on Eq. 4.1, the natural (or FMR-K) resonance (at H=0) would occur at $f_{FMR} = v[H_K(H_K + 4\pi M_S)]^{1/2} \fallingdotseq v[H_K 4\pi M_S]^{1/2}$ with $H_K \ll 4\pi M_S$. The addition of Ni into $Fe_{81}Ga_{19}$ alloys causes reduced the magnetic anisotropy energy which let the H_K decreases, leads to decreases in H_K is evident from Fig. 4.2(a). The plot of f_{FMR} vs. x or y is shown in Fig. 4.2(b), which exhibits similar trend of $H_K(x,y)$ shown in Fig. 4.2(a). Because $4\pi M_S$ of the FeNiGa films is almost independent of x or y, it implies that the f_{FMR} of the FeNiGa films depend solely on H_K as suggested by the equation $f_{FMR} \fallingdotseq v[H_K 4\pi M_S]^{1/2}$. The fact that both have the same trend with the variations of Ni concentration is consistent with this conjecture. As

other discussed in next paragraph, f_{FMR} should serve as the cut-off (or limiting) frequency (f_C) for these series of ferromagnetic films.

In general, the complex permeability, $\mu = \mu_R - i\mu_I$, has an anomalous behavior, with the real part, μ_R, drops off and the imaginary part, μ_I, exhibits an absorption peak at a certain high frequency, e.g. f_C. For a non-metallic ferromagnet, f_C is mainly determined by FMR. For a metallic ferromagnet, according to Fig. 4.17 of Ref. [1], f_C should depend on the dimensions, e.g., t_f, of the sample. For example, if $t_f < \delta$, where δ is the skin depth, f_C, the μ_R or μ_I anomaly at f_C is related the FMR effect in the μ vs. f spectrum. On the other hand, if $t_f > \delta$, f_C, will be dominated by the eddy-current effect[1]. In our case, t_f =100 nm $< \delta \approx 650$ nm (at f ~ 1 GHz), thus we expect $f_C = f_{FMR}$ for all the FeNiGa films. However, since the FeNiGa films are in each metallic, the eddy-current effect might also play a role and should be considered in the resonance cases. We will come back to this point later.

At low frequencies, the definition of rotation permeability for an un-plane uniaxial film, such as the FeNiGa film studied has, is $\mu \sim \mu_R = 4\pi M_S/H_K$. Fig. 4.3(a) shows the calculated μ_R of the FeNiGa films for variance Ni concentrations. It is evident that in both series of FeNiGa film μ_R increases with increasing Ni concentrations. This general tendency can be understood as follows. The Snoek's law derived from the Landau-Lifshitz equation, gives[2, 3],

$$(\mu_R - 1)f_{FMR}^2 = (\nu 4\pi M_s)^2. \tag{4.2}$$

In Eq. 4.2, $4\pi M_S$ of the FeNiGa films is almost independent of x or y; i.e. it only decreases by 5%, as x or y increases from 0 to 26 at.%Ni. However, based on

Fig. 4.2, $(f_{FMR})^2$ decreases by 64%, as x or y increases similarly. From Eq. 4.2, there should be a trade-off between μ_R and f_{FMR} for the two series of FeNiGa films. Indeed, as can be seen from Fig 4.3(b), the value of $\mu_R \times (f_{FMR})^2$ remains nearly constant over the range of Ni concentration for FeNiGa films investigated in this study.

For a ferromagnetic film, high speed magnetization switching means low Gilbert damping parameter (α). From Landau-Lifshitz-Gilbert (LLG) equation, the magnetic damping parameter (α) can be written as[40],

$$\alpha = \frac{\Delta f_{1/2}}{\nu 4\pi M_S} \ , \tag{4.3}$$

where $\Delta f_{1/2}$ is the full width at half maximum for the absorption peak of μ_I at resonance. The form is used in a shorted microstrip transmission line perturbation experiment. Alternatively, Eq. 4.3 can also be written as[16],

$$\alpha = \nu (\Delta H)_S / 2 f_{FMR} \ , \tag{4.4}$$

where $(\Delta H)_S$ is the *theoretical* full width at half maximum of the absorption peak around the main resonance field (H_R). Notice that the subscript "s" of ΔH in Eq. 4.4 means that this *theoretical* ΔH should be, in principle, symmetric with respect to the central peak, H_R. In the following, we shall give a reason for this argument. The LLG equation with Kittel mode can obtain the equation[2, 3, 41],

$$\tan\phi = \frac{4\pi\lambda\mu_0}{\nu M_S}\frac{H}{H-H_R} \qquad (4.5)$$

where the angle ϕ is the rotating field vector $\vec{h}_{rf}$ made a finite azimuthal angle with the magnetization vector $\vec{M}_S$, $\lambda \equiv (\alpha\nu M_S)/(4\pi\mu_o)$, and $\vec{H}$ is an in-plane field with EA//$\vec{H}$. From Eq. 4.5, tan(ϕ) reaches the maximum value, when H=H_R or $\phi = 90^o$.

That we can write down the real and imaginary parts of the susceptibility as

$$\mu_R \sim \chi' = \frac{M_S}{h_{rf}}\sin\theta\cos\phi$$

$$\qquad (4.6)$$

$$\mu_I \sim \chi'' = \frac{M_S}{h_{rf}}\sin\theta\sin\phi$$

or,

$$\chi' = \frac{M_S}{\alpha H_z}\sin\phi\cos\phi$$

$$\qquad (4.7)$$

$$\chi'' = \frac{M_S}{\alpha H_z}\sin^2\phi$$

Similarly, from Eq. 4.7, the maximum χ'' also occurred at $\phi = 90^o$,

Fig 4.4 shows the result in representation. The width of the absorption curve at half the maximum value or a half-value width can be calculated by putting $\phi= 45^o$, which makes the value of χ'' in half of its maximum value.

In other words, if Eqs. 4.5 and 4.6 are combined, we obtain,

$$\mu_I \propto \sin^2\phi \propto \frac{H^2}{H^2+(\frac{1}{\alpha})^2(H-H_R)^2} \qquad (4.8)$$

In Eq. (4.8), μ_I is a Lorentzian function of H, which means that μ_I must be symmetric with respect to H_R, and by definition the symmetric width $(\Delta H)_S \equiv 2\alpha H_R$, i.e. Eq. 4.4.   However, in reality, as shown in Fig. 3.13, the *experimental* width $(\Delta H)_{exp}$ is not always ideally symmetric.   Thus, we consider that $(\Delta H)_{exp}=(\Delta H)_S+(\Delta H)_A$, where $(\Delta H)_A$ is the asymmetric parts in $(\Delta H)_{exp}$.   In general, there are three sources which may make contribution to $(\Delta H)_A$: one is from the structural inhomogeneity, and the other two are from the magnetic inhomogeneites[41].   As discussed previously, Table 4.2 shows that if y = 0, 22, and 26 at.%Ni (range A), the films are structurally homogenous (i.e., containing only one A2 phase) and if y = 4 – 17 at.%Ni (range B), they are structurally inhomogenous (i.e., containing mixed phases).   Thus, we expect for the former films thei0r $(\Delta H)_A$'s are smaller, while for the latter films their $(\Delta H)_A$'s are larger.   It is in agreement with the experimental data from FMR experiments that for films in range A, the degree of asymmetry of the peak width, $(\Delta H)_A/(\Delta H)_{exp} = 0 – 5.5\%$, is smaller, while for those in range B, the degree of asymmetry, $(\Delta H)_A/(\Delta H)_{exp} = 8.8 – 20.2\%$, is larger.   As to the magnetic inhomogeneity, one mechanism is due to the asymmetric distributions of the magnitude and/or angle dispersion of $\vec{H}_K$.   The other is associated with the local inhomogenous demagnetizing field (H_d) near edges of the film sample.   Here, we are unable to assess how much the magnetic-inhomogeneity

mechanisms would affect $(\Delta H)_A/(\Delta H)_{exp}$ quantitatively.

Fig. 4.5 shows that as y increases, α decreases from 0.076 to 0.018 for the FeNiGa films deposited on glass substrates, and as x increases, α first decreases from 0.051 to 0.018 and then increases from 0.018 to 0.053 for the FeNiGa films deposited on Si(100) substrates. Yager, Galt, and Merritt had pointed out that ΔH is related to H_K. They argued that the anisotropy forces magnetization to rotate parallel to the direction of easy magnetization, and, for the same reason, rotation of magnetization may cause a change in the arrangement of two kinds of ions such as to rotate the easy direction toward the direction of magnetization[2]. In addition, we also find the addition of Ni into $Fe_{81}Ga_{19}$ alloy films on glass substrates to reduce the $D0_{19}$ phase and $L1_2$ phase in XRD results. Briefly speaking, when y = 22 at.%Ni, there is only one single A2 phase. That centralized the H_R and narrow ΔH in the alloys. Notice that in equation 4.4, α of the FeNiGa alloy is calculated from ΔH; α decreases, as ΔH decreases. Another one may notice that there is discrepancy between α data of the x- and y-series films in the range $17 \leq x$ or $y \leq 26$ at.%Ni. In the following, we shall explain why the α data from the y-series ($Fe_{81-y}Ni_yGa_{19}$/glass) films should be more reliable. The p-doped Si(100) semiconductor is conducting with electrical resistivity (ρ), about 5-10 Ωcm. On the other hand, ρ is about 120 - 150 $\mu\Omega$cm for FeNiGa films deposited on insulating glass, it is shown in Fig. 4.6. Further, the ratio of t_{Si}/t_f is about 10^3. A simple calculation would show that the electrical resistance ratio, R_{Si}/R_f, for the x-series ($Fe_{81-x}Ni_xGa_{19}$/Si(100)) films is of the order of one. Thus, the current shunting effect must be significant in the case of FeNiGa films deposited on Si(100). As observed, the (apparent) ρ of the x-series films is general smaller than that of the

y-series films.   In an FMR situation, the eddy current, i_{ac} induced by $\vec{h}_{rf}$, must be at least flowing in the conducting FeNiGa film.   For the y-series film, because glass is an insulator, i_{ac} is mainly limited inside the film region. However, for the x-series films, due to the current shunting effect, i_{ac} will flow across the film/Si interface.   Moreover, the spin injection across the interface indicates that the proximity region on the Si side, which is partially magnetized, will also absorb microwave, and make an extra contribution to the main FMR signal from the film.   As a result, for the x-series ($Fe_{81-x}Ni_xGa_{19}/Si(100)$) films, there is an additional broadening of the FMR peak width due to the extraneous eddy-current effect[41].   Thus, in general α of the $Fe_{81-x}Ni_xGa_{19}/Si(100)$ films, as shown in Fig. 4.4, may be less accurate than that of the $Fe_{81-y}Ni_yGa_{19}/glass$ films.
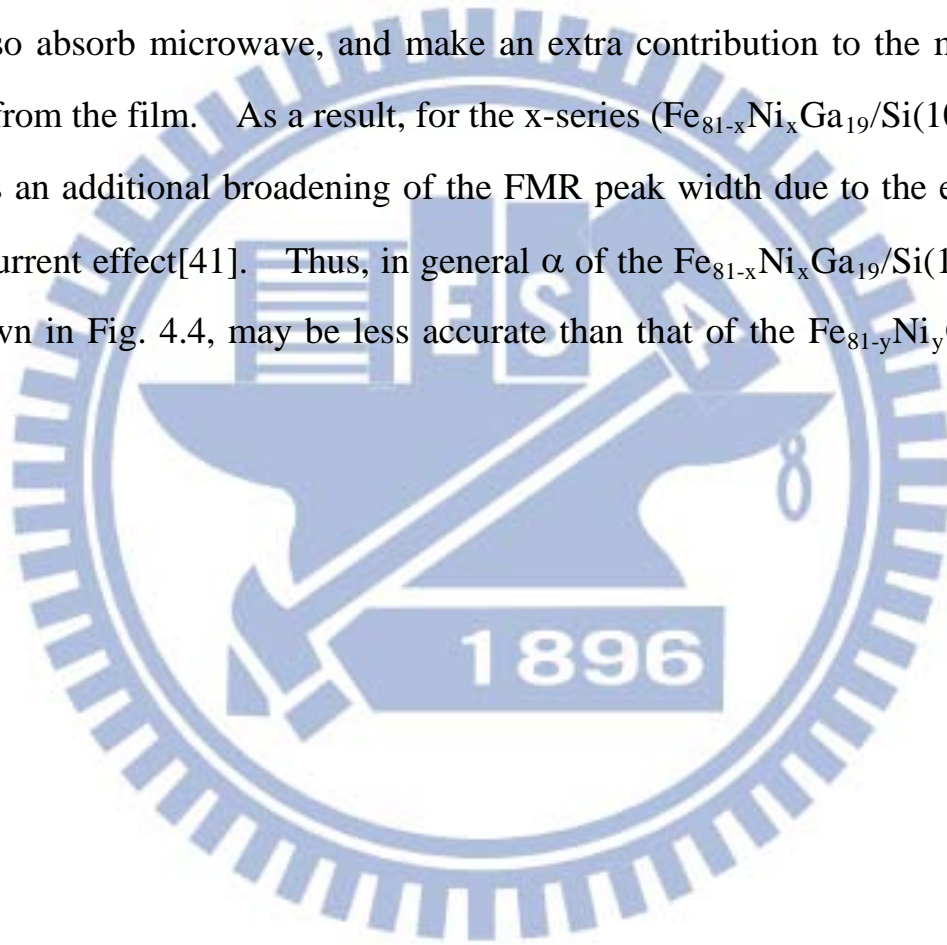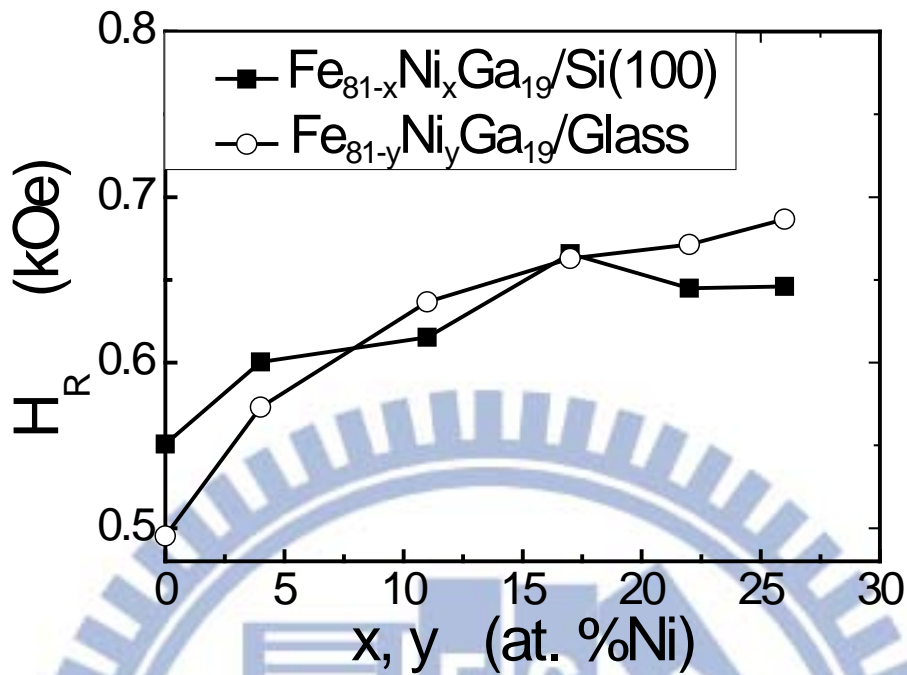
Fig. 4.1 The main resonance field (H_R), at f = 9.6 GHz, the various FeNiGa films.
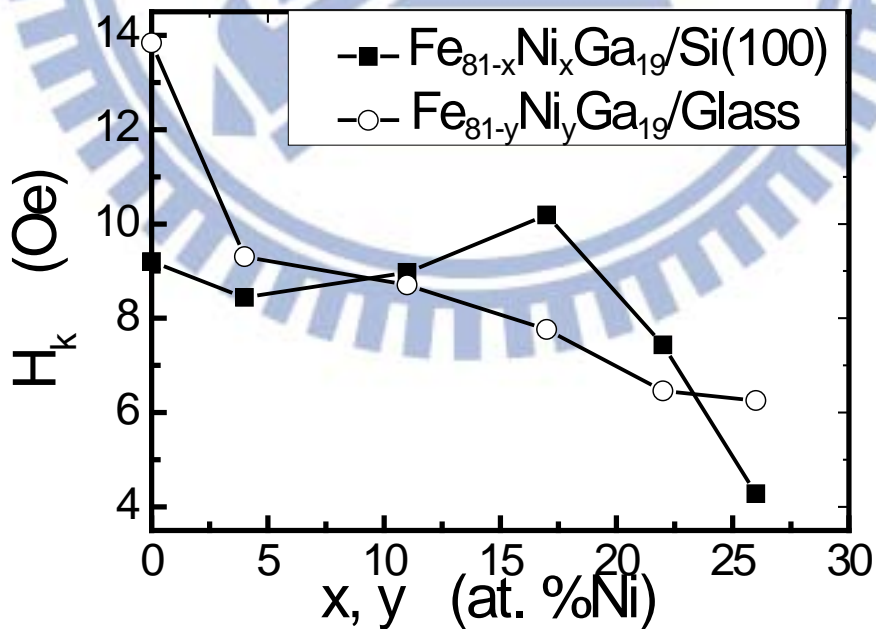
Fig. 4.2(a) Magnetic anisotropy field (H_K) decreases, as at% Ni increases of the FeNiGa (x or y).
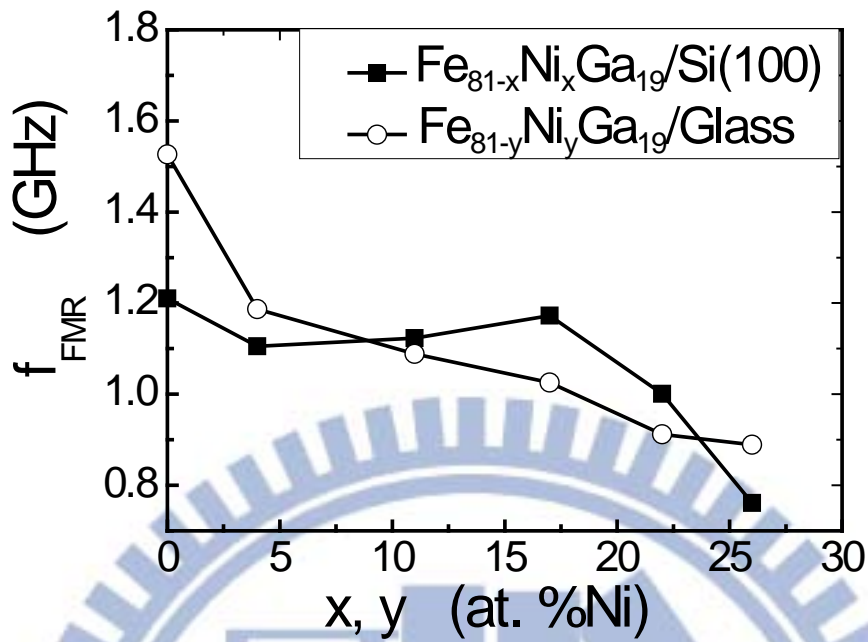
Fig. 4.2(b) Natural resonance frequency (f_{FMR}) of the FeNiGa films plotted vs. the Ni concentration (x or y).
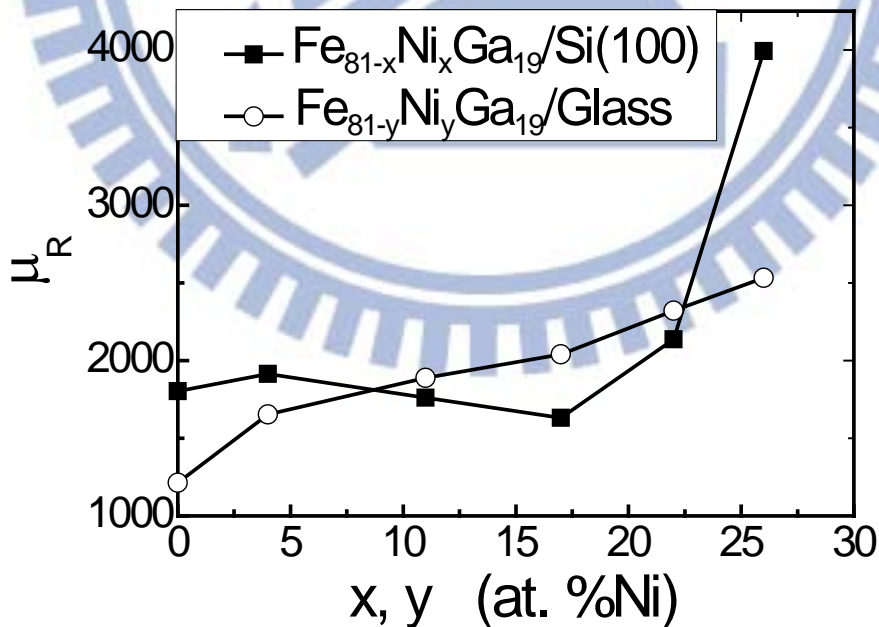
Fig. 4.3(a) Static rotational permeability (μ_R) increases, x or y increases in the FeNiGa films.
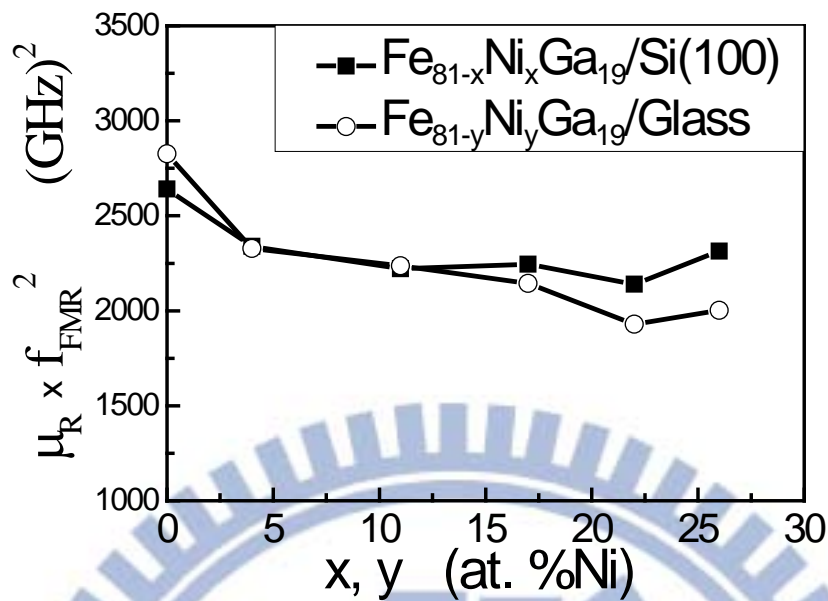
Fig. 4.3(b) The products, $\mu_R \times (f_{FMR})^2 \doteq$ constant, x or y increases in the FeNiGa films.
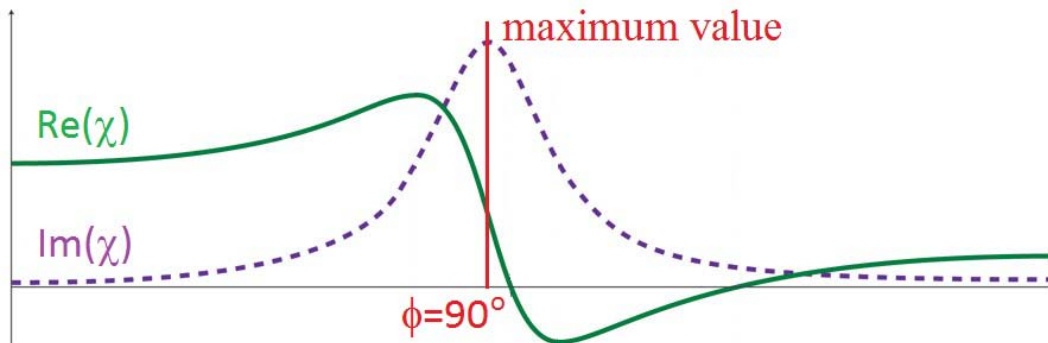
Fig 4.4 shows dependence of the real and imaginary part of the rotational susceptibility on the intensity of the dc field about the resonance field. The maximum χ'' occurred at $\phi = 90^o$, and the width of the absorption curve at half the maximum value or a half-value width correspond at $\phi = 45^o$.

Table 4.2 $(\Delta H)_A/(\Delta H)_{exp}$ is the degree of asymmetry of the FMR linewidth.

	x or y (at% Ni)	0	3	11	17	22	26
x:	$(\Delta H)_A/(\Delta H)_{exp}$ (%)	9.4	8.8	5.1	18.7	5.1	2.0
y:	$(\Delta H)_A/(\Delta H)_{exp}$ (%)	1.4	4.7	13.8	20.2	5.5	~ 0
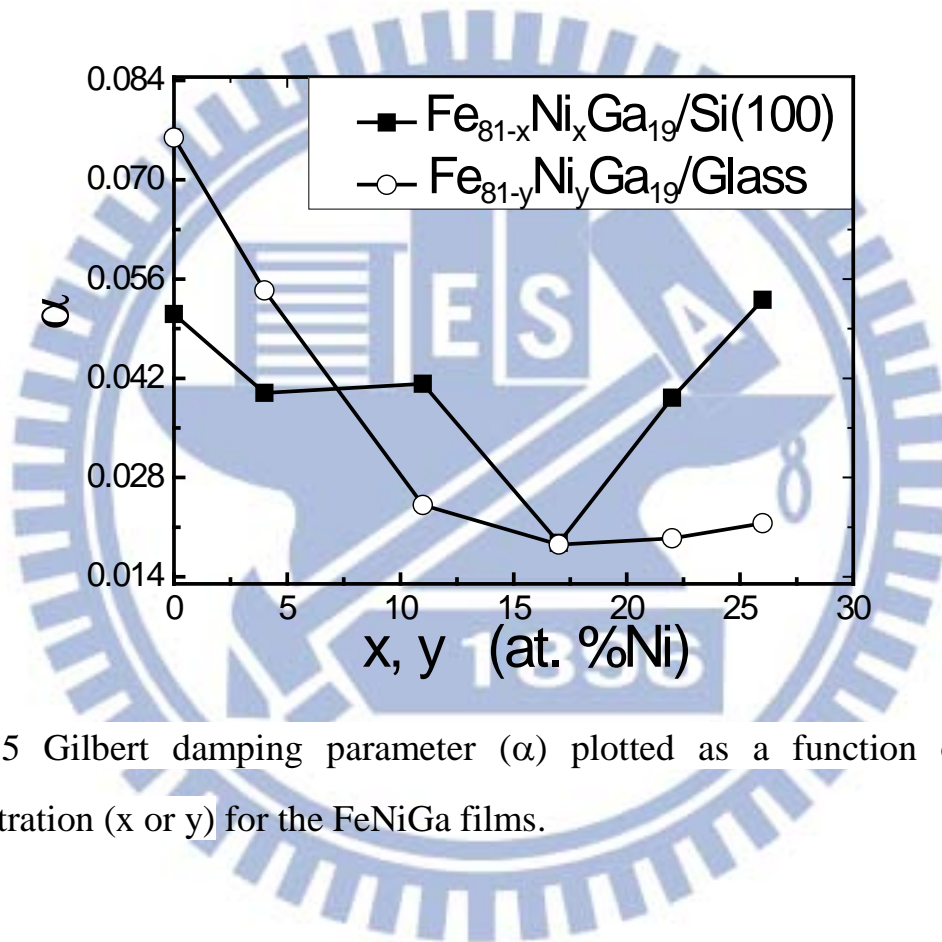
Fig. 4.5 Gilbert damping parameter (α) plotted as a function of the Ni concentration (x or y) for the FeNiGa films.
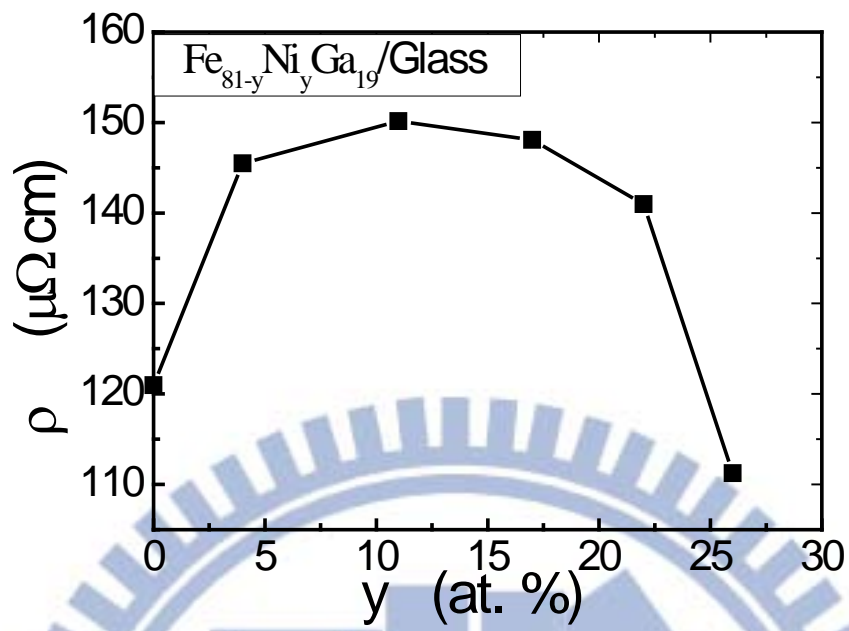
Fig. 4.6 Electrical resistivity (ρ) is about 120 - 150 $\mu\Omega$cm for FeNiGa films deposited on insulating glass.

4.3 Magnetostrictions data

4.3.1 Young′s modulus (E_f) data

Fig. 4.7 shows that for the $Fe_{81-y}Ni_yGa_{19}$/glass films, as y increases, E_f is almost constant, 120 GPa, except when y = 17, the E_f is up to 133 GPa, and for the $Fe_{81-x}Ni_xGa_{19}$/Si(100) films, as x increases from 0 to 17, E_f first increases from 170 to 182 GPa, then decreases from 182 to 154 GPa, and finally when x > 17, E_f increases again.   Different film-growth mechanisms, due to uses of different substrates, cause the former being less denser than the latter. Thus, even under the same film composition condition (i.e., x = y), E_f of the x-film is stiffer than that of the y-film.
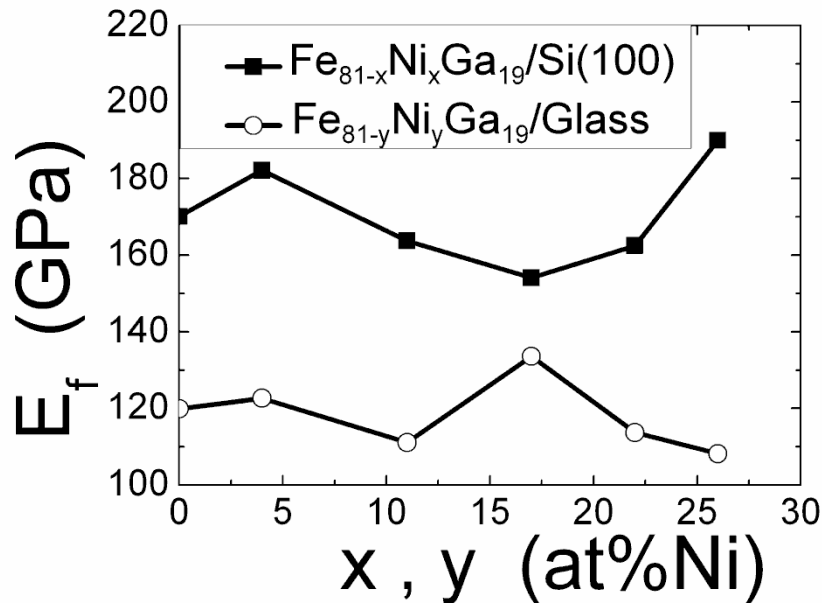
Fig. 4.7 This is Young′s modulus of the two series of $Fe_{81-x}Ni_xGa_{19}$/Si(100) and $Fe_{81-y}Ni_yGa_{19}$/glass films, respectively.

4.3.2 Main data

Fig. 4.7 shows λ_S of the x- and y-series FeNiGa films as function of the Ni concentration (x or y). The general trend in Fig. 4.8 is that as x or y increases, λ_S increases, and λ_S reaches maximum when x and/or y = 22 at.%Ni. For $Fe_{59}Ni_{22}Ga_{19}$/Si(100), λ_S = 28 ppm, and for $Fe_{59}Ni_{22}Ga_{19}$/glass , λ_S = 21 ppm. According to Ref. 22, the $D0_{19}$ phase and $L1_2$ phase are detrimental to saturation magnetostriction. In this study, we found the addition of Ni into $Fe_{81}Ga_{19}$ alloy films oppresses the formation of $D0_{19}$ and $L1_2$ phases. Even when y = 22 at.%Ni, there is only one single A2 phase. So we get magnetostriction constants in the FeNiGa ternary alloys higher than those of the $Fe_{81}Ga_{19}$ binary alloys. In addition, notice that the saturation field of these films is very low, about 15 Oe. Hence, their magnetostriction sensitivity can be quite high, about 1.9 – 2.7 ppm/Oe, which is suitable for the low field and high frequency application.

The t_f dependence of λ_S of $Fe_{59}Ni_{22}Ga_{19}$/Si(100) and $Fe_{59}Ni_{22}Ga_{19}$/glass films is shown in Fig. 4.9. The trend for $Fe_{59}Ni_{22}Ga_{19}$/Si(100) films is that as t_f increases from 65 to 195 nm, λ_S increases from 25 to 30 ppm and, and as 195 < t_f ≤ 260 nm, λ_S remains constant. The trend for $Fe_{59}Ni_{22}Ga_{19}$/glass films is similar. These results can be explained by the surface oxidation and/or the film/substrate interface effects [42].

Fig. 4.8 Saturation magnetostriction (λ_S) reaches maximum, when x or y = 22 at.%Ni.
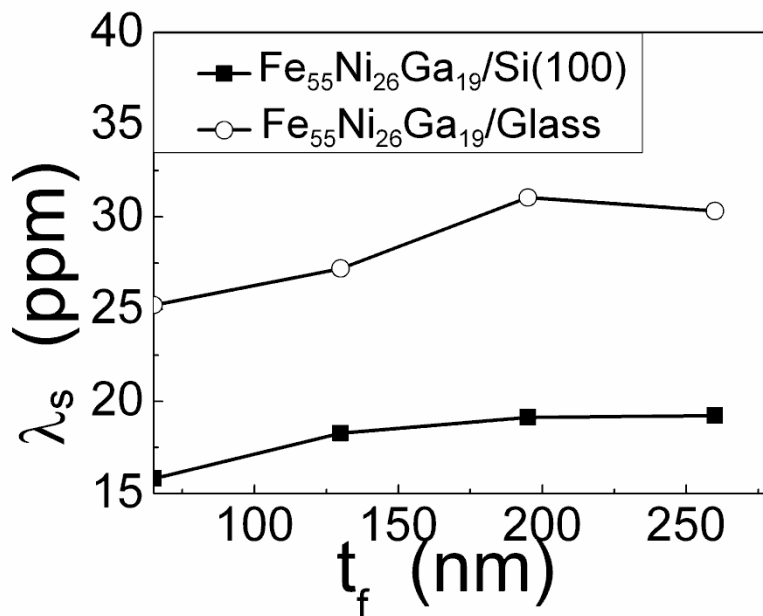
Fig. 4.9 The t_f dependence of λ_S of the $Fe_{59}Ni_{22}Ga_{19}$/Si(100) and $Fe_{59}Ni_{22}Ga_{19}$/glass films.

5. Results and discussion for ribbons

5.1 XRD data

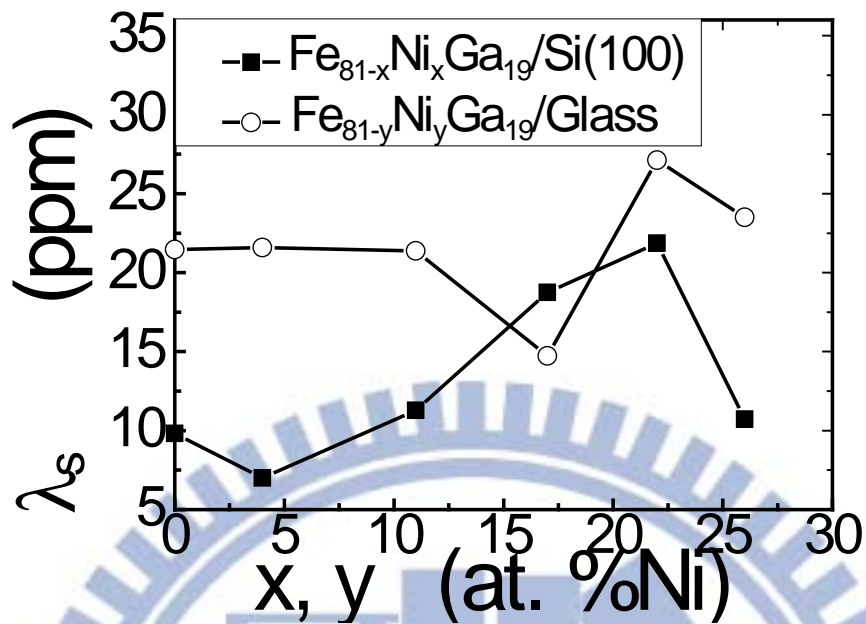According to the x-ray diffraction patterns (Table 5.1) of the melt-spun $Fe_{81-z}Ni_zGa_{19}$ and the JCPD information[43], we can identify the A2(110), A2(200), and A2(211) diffraction peaks.   From these findings, lattice constant (a_0) of melt-spun $Fe_{81-z}Ni_zGa_{19}$ can be calculated respectively[44].   For example, Fig. 5.1 shows the information of θ angle and the corresponded lattice of the melt-spun $Fe_{81}Ga_{19}$ x-ray diffraction pattern peaks of A2(110), A2(200), and A2(211).   From these three points, the value of a_0 can be found by plotting a_{hkl} (lattice) against ($\cos^2\theta/\sin\theta+\cos^2\theta/\theta$), which approaches zero as θ approaches 90°; a fitting line runs through three points and crosses the a-axis[45]. That can make sure the lattice constant of the melt-spun $Fe_{81}Ga_{19}$ ribbon. Each melt-spun $Fe_{81-z}Ni_zGa_{19}$ ribbon samples are shown in Fig. 5.2.   The lattice constant first increases from 2.925 Å to 2.931 Å, then decreases to 2.900 Å finally then stabilizes around 2.900 Å, as z of the FeNiGa ribbons increases. The radii of atomic Fe, Ni are about 1.23Å, 1.23Å, and the radii of ion Fe^{2+}, Ni^{2+} are about 0.74Å, 0.69Å, respectively[46].   Thus, the lattice constants of these ribbons showed dependence on z.   Furtherance exhibited the similar trends in z-dependence, as the lattice constant and electrical resistivity, shown in section 5.3.   However, for z=24 at.% Ni, the diffraction peaks are not all identified, indicating these might exist some other phases at in these ribbon.   We will come back on this in chapter 7.

Table 5.1 Structural properties, the x-ray diffraction peaks, of the Fe81-zNizGa19 ribbons. I/Imax is the peak intensity ratio. a_0 is the lattice constant.

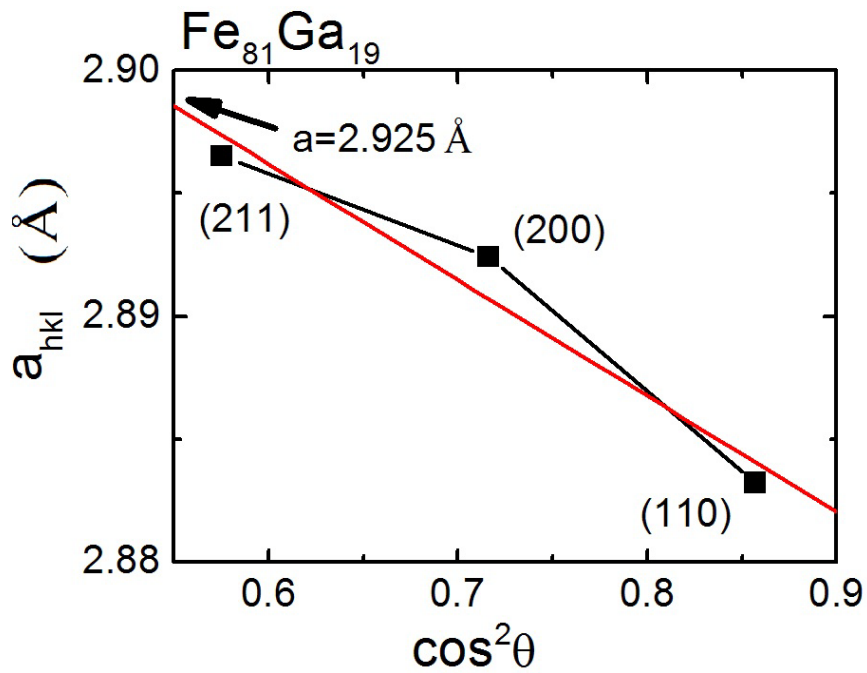| z (at. %Ni)	2θ (deg.)	phase (hkl)	d (Å)	a_0 (Å)	I/I$_{max}$ (%)
	44.4	A2(110)	2.039		100
0	64.37	A2(200)	1.446	2.925	75
	81.3	A2(211)	1.183		40.4
	44.57	A2(110)	2.031		100
3	64.53	A2(200)	1.443	2.931	35.1
	81.46	A2(211)	1.181		32.7
	44.7	A2(110)	2.026		100
7	64.77	A2(200)	1.438	2.921	41.6
	81.76	A2(211)	1.177		40.3
	44.4	A2(110)	2.039		100
13	64.5	A2(200)	1.444	2.9	19.6
	81.56	A2(211)	1.179		29.2
	44.7	A2(110)	2.026		100
19	64.8	A2(200)	1.438	2.909	20.2
	81.89	A2(211)	1.175		45.6
	44.64	A2(110)	2.028		100
24	64.8	A2(200)	1.438	2.906	18.5
	81.83	A2(211)	1.176		19.2

Fig. 5.1 The lattices constant of melt-spun $Fe_{81}Ga_{19}$ be calculated by the red line cross y-axis.   The lattice constant of this ribbon is 2.925 Å.
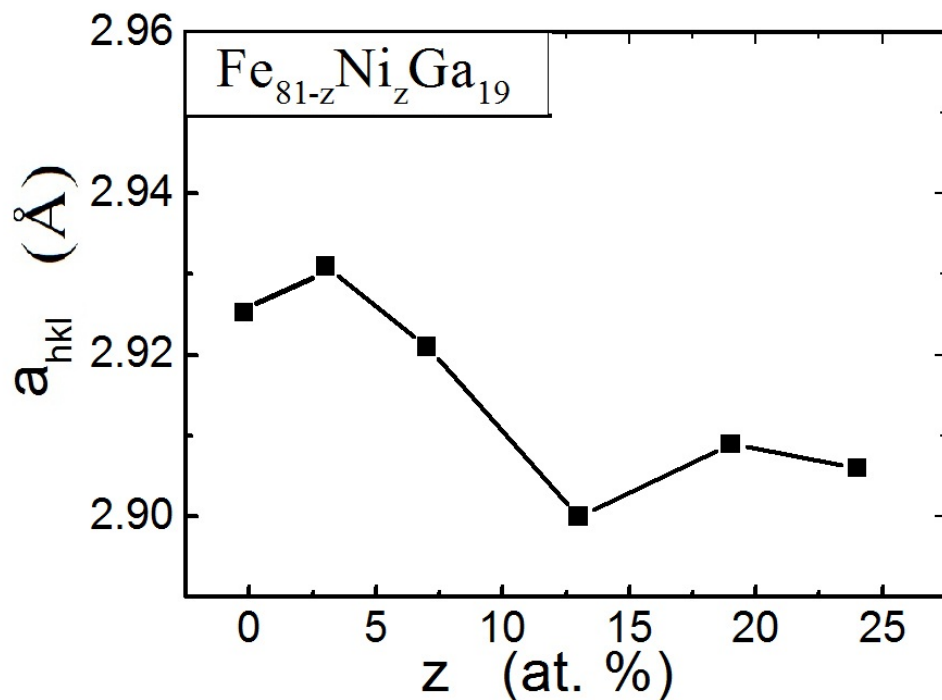

Fig. 5.2.   The lattice constant first decreases from 2.925 Å to 2.900 Å and then stabilizes around 2.900 Å for the FeNiGa ribbons.

5.2 VSM results

In general, addition Ni replace Fe at.% in alloys to be caused refined magnetic in rich-Fe alloys. Especially in the magnetic anisotropy energy and saturation magnetization, there would be shown later. The VSM results of the $Fe_{81}Ga_{19}$ ribbon are shown in Fig. 5.3. When $\theta=0^\circ$, the in-plane external field H_E is parallel (//) to EA, and when $\theta=90^\circ$, H_E is perpendicular ($\perp$) to EA. We can obtain M_S, SQR, H_C, and H_s from these two plots. In addition, upon the addition of Ni in the series of $Fe_{81-z}Ni_zGa_{19}$ ribbon, the magnetic anisotropy energy disappeared completely. Namely, the magnetic anisotropy energy because isotropic for the series $Fe_{81-z}Ni_zGa_{19}$ ribbons, except when z is 0.

In soft ferromagnetic alloy devices, the basic requirements are that low coercivity (H_C), and high saturation magnetization (M_S). Fig. 5.4(a) shows M_S plotted as a function of z. As z increases from 0 to 24 in $Fe_{81-z}Ni_zGa_{19}$, M_S decreases from 170 emu/g to 116 emu/g. Fig. 5.4(b) indicates that H_C increases from 4.8 Oe not a lot, as z increases except z=24. As will be discussed later in Chap. 7, this implies that there are other phases in the $Fe_{57}Ni_{24}Ga_{19}$ alloy ribbon. At last, Fig. 5.4(c) shows that H_s does not change too much with increasing z.
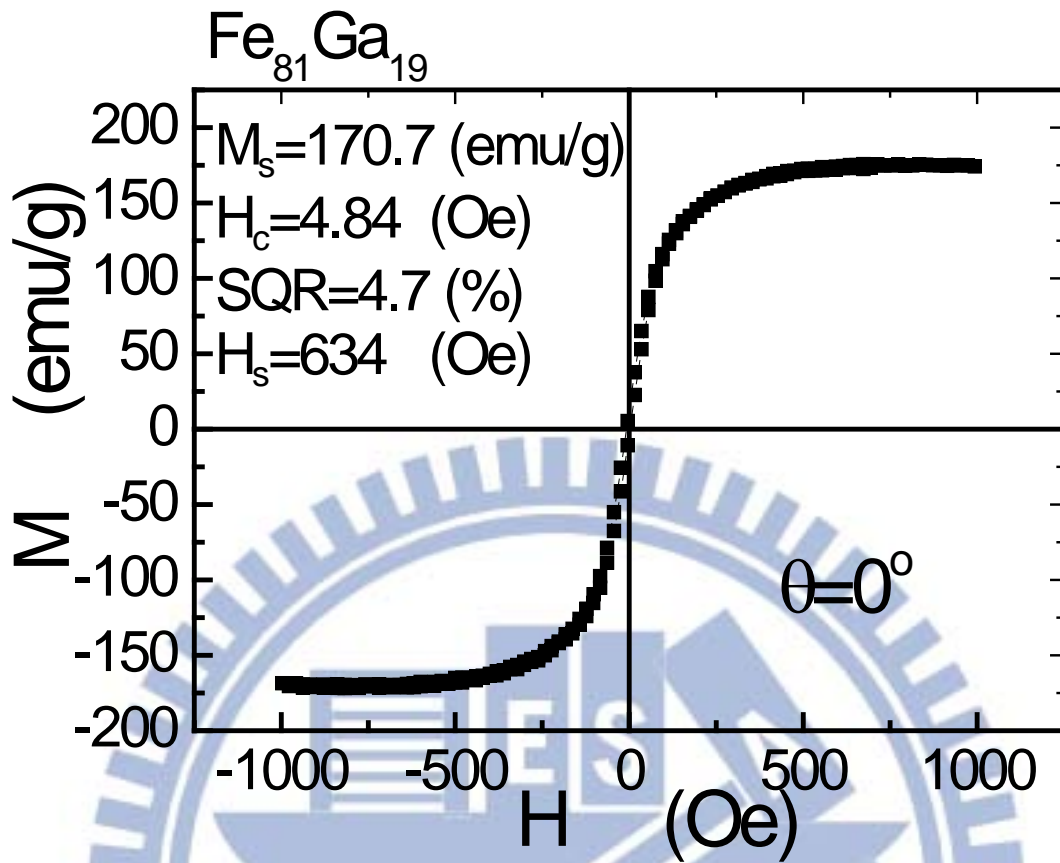
Fig. 5.3 The easy-axis ($\theta=0^\circ$) hysteresis loops of the melt-spun $Fe_{81}Ga_{19}$.

(a) $Fe_{81-z}Ni_zGa_{19}$

(b) $Fe_{81-z}Ni_zGa_{19}$

(c)
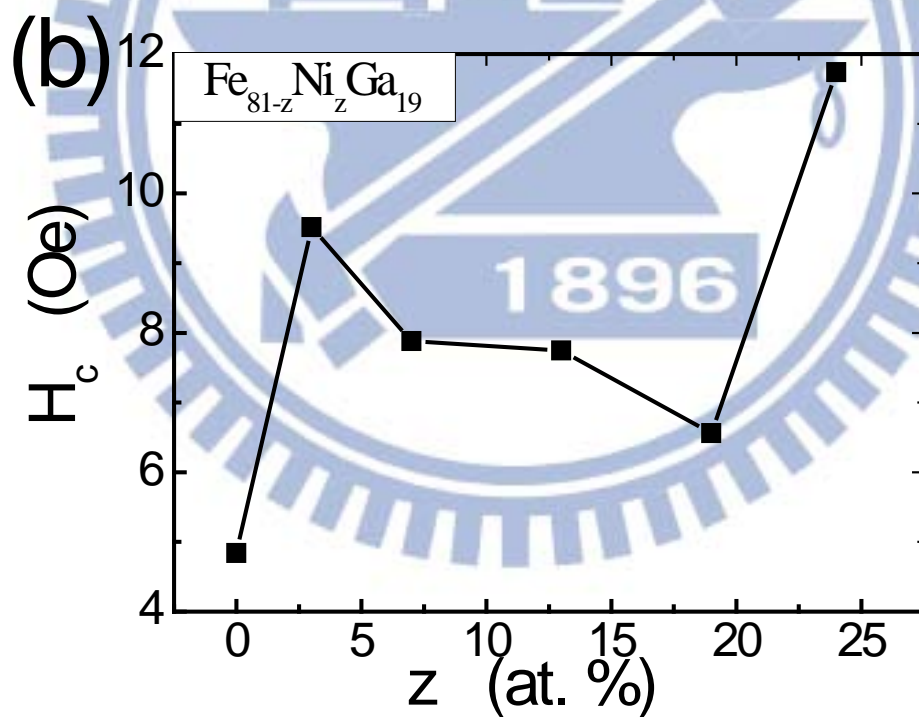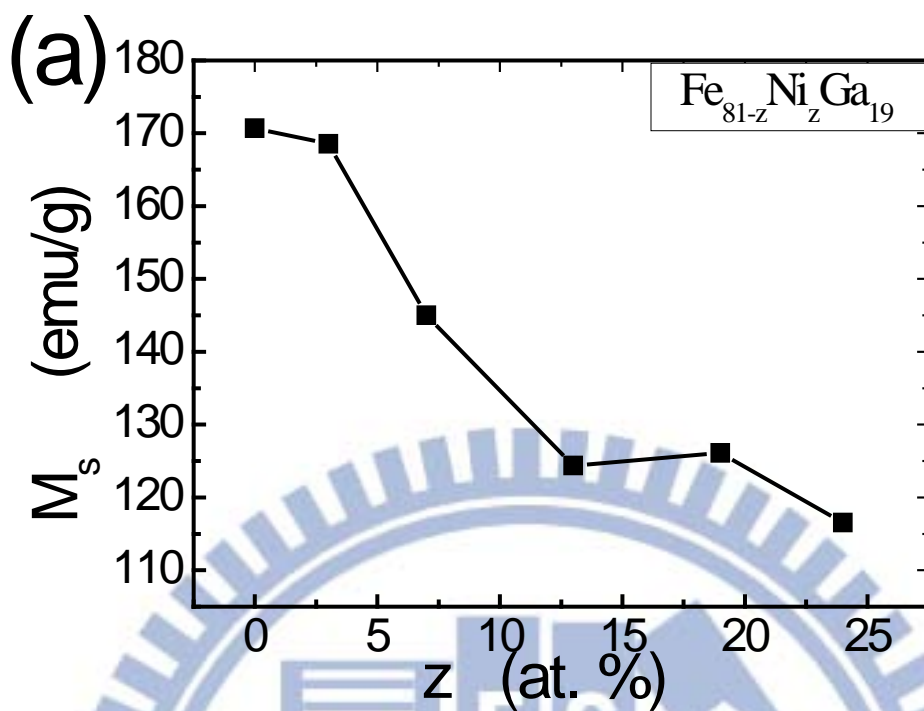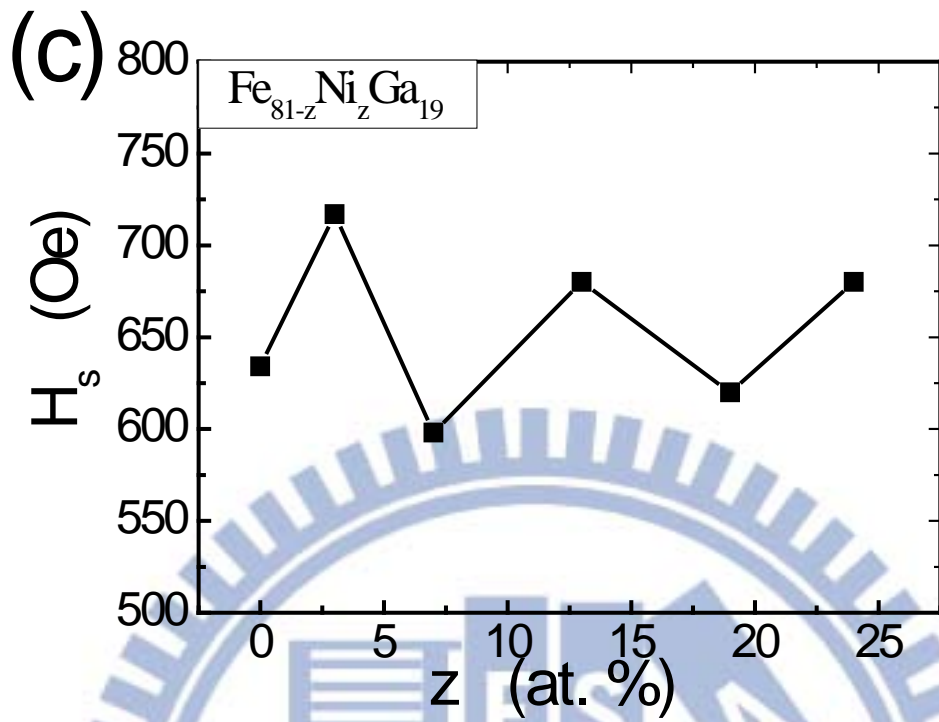
$Fe_{81-z}Ni_zGa_{19}$

Fig. 5.4 shows Saturation magnetization (M_s), coercivity (H_c), and saturation field (H_s) hysteresis of the melt-spun $Fe_{81-z}Ni_zGa_{19}$.

5.3 Electrical resistivity

Fig. 5.5 illustrates the ρ vs. x plot, as z increases from 0 to 13, ρ of the melt-spun $Fe_{81-z}Ni_zGa_{19}$ decreases little from 111 $\mu\Omega$cm to 95 $\mu\Omega$cm, as z increases from 0 to 13, ρ of the melt-spun $Fe_{81-z}Ni_zGa_{19}$ increases little from 95 $\mu\Omega$cm to 108 $\mu\Omega$cm. The resistivity and lattice constants reaches minimum simultaneously for the melt-spun $Fe_{68}Ni_{13}Ga_{19}$, indicating that substituting larger Fe^{2+} with smalls Ni^{2+} may introduced more carriers. The rapid increase of ρ of the $Fe_{57}Ni_{24}Ga_{19}$, however, might be due to the existence of other phases arising from the excessive doping of Ni.
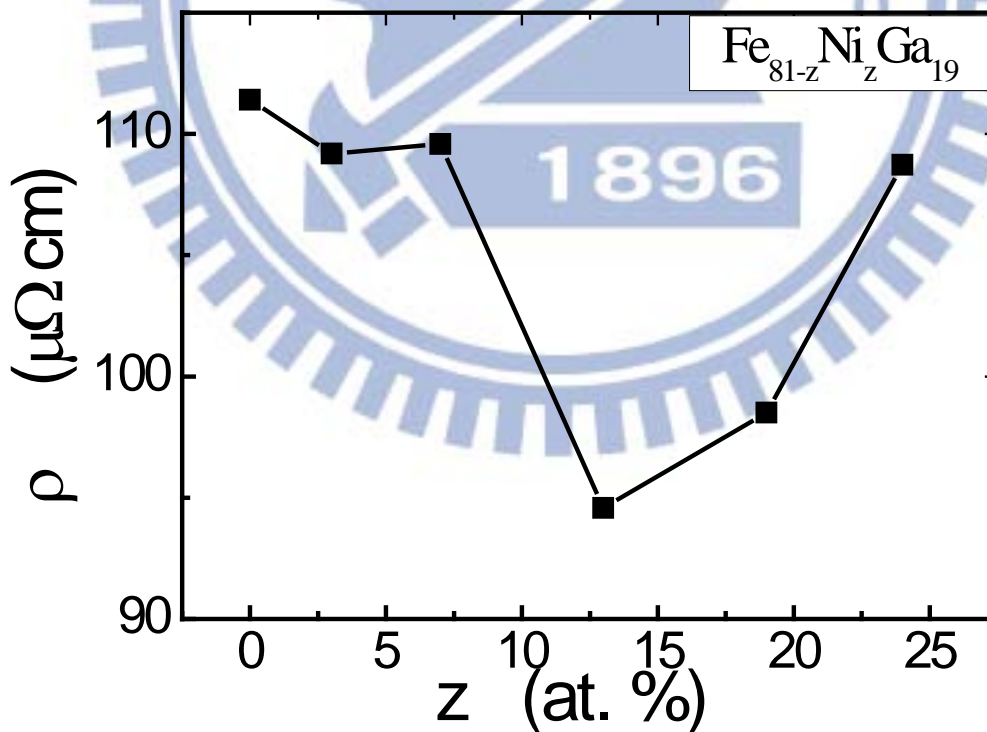
Fig. 5.5 Electrical resistivity (ρ) of the melt-spun $Fe_{81-z}Ni_zGa_{19}$.

5.4 Young's modulus of the ribbon

The magnetostriction is a dependence of Young's modulus E of a magnetic material on its state of magnetization. When an originally demagnetized specimen is saturated, its modulus increases by an amount ΔE. The value of $\Delta E/E_0$ depends greatly on the way in which it is measured, as will be explained below[2].

Fig. 5.6 shows the normal σ vs. $\Delta\varepsilon$ plot, which plot is called normal, because it is concave up, as shown in Refs. 2, 3, and 38. That is, the slope of the dotted fitting line (slope I) is smaller than that of the solid fitting line (slopeII). At the intersection of the slopes I and II lines, we can define the critical internal stress (σ_{ic}) of the ribbon[3,38]. The physical meaning of σ_{ic} can be considered as the critical transition point for the ribbon sample from the demagnetized state to the saturation state through the magneto-elastic mechanism; e.g., Fig. 8.26 of Ref. 14. Moreover, from slope II, we can determine the Young's modulus (E_S) in the saturated state. Also, from slope II and the intercept of the solid fitting line, we can find the elastic strain $\Delta\varepsilon_{el}$ and magneto-elastic strain $\Delta\varepsilon_{me}$[14, 22]. As a result of these two kinds of strain, the modulus in the demagnetized state is[2]

$$E_0 = \frac{\sigma}{\Delta\varepsilon_{el} + \Delta\varepsilon_{me}} \qquad (5.1)$$

and the modulus in the saturated state is

$$E_s = \frac{\sigma}{\Delta\varepsilon_{el}} \qquad\qquad (5.2)$$

These two relations lead to

$$\frac{\Delta E}{E_0} = \frac{E_s - E_0}{E_0} = \frac{\Delta\varepsilon_{me}}{\Delta\varepsilon_{el}} \qquad\qquad (5.3)$$

For sample of the $Fe_{81}Ga_{19}$ ribbon, we fixed $\sigma = 25$ Mpa to calculate E_S and $\Delta E/E_0$ by Eq. 5.2 and Eq. 5.3. In Fig. 5.7, we find E_S of the $Fe_{81-z}Ni_zGa_{19}$ ribbons is in the range 115 to 52 GPa. In Fig. 5.8, we find $\Delta E/E_0$ is in the range 14% to 115%. In Fig. 5.9, σ_{ic} not change a lot between $Fe_{81}Ga_{19}$ and $Fe_{78}Ni_3Ga_{19}$, as z increases from 3 to 19 in $Fe_{81-z}Ni_zGa_{19}$, σ_{ic} increases, and σ_{ic} decreases at z = 24. There are two points to be noted here. Firstly, the $Fe_{57}Ni_{24}Ga_{19}$ has phases other than A2 phase existing in the ribbon, which may account for the deviation of the general trend in this series of ribbon. (As can be seen in Fig. 5.7- 5.9 and Fig. 5.12 in the next section.) Secondly, we were unable to obtain reliable data from $Fe_{68}Ni_{13}Ga_{19}$ ribbon. The reason is not clear at present, and further investigations are need.
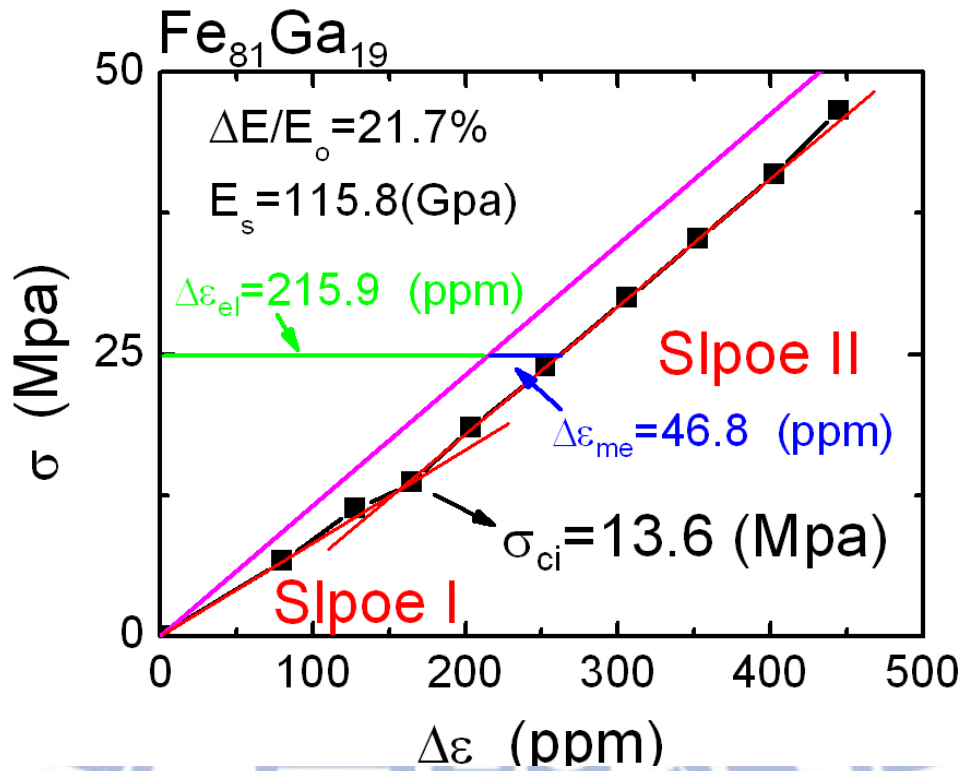
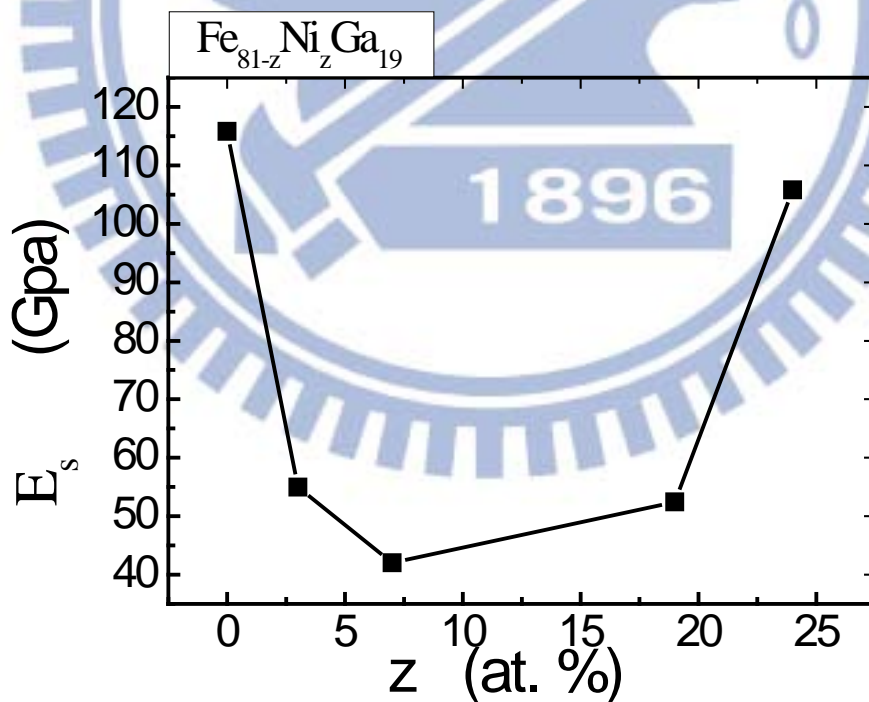Fig. 5.6 The stress (σ) vs. strain ($\Delta\varepsilon$) curves of the as-spun $Fe_{81}Ga_{19}$ ribbon.

Fig. 5.7 The Young's modulus in the saturated state (E_s) plotted as a function of z.

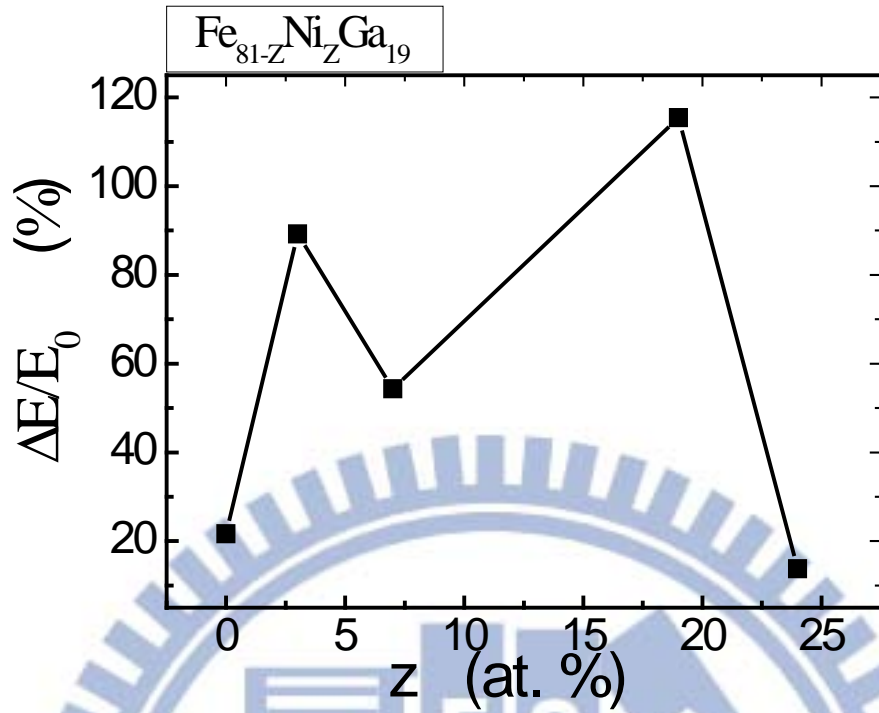Fig. 5.8 The ΔE effects of the melt-spun $Fe_{81-z}Ni_zGa_{19}$.
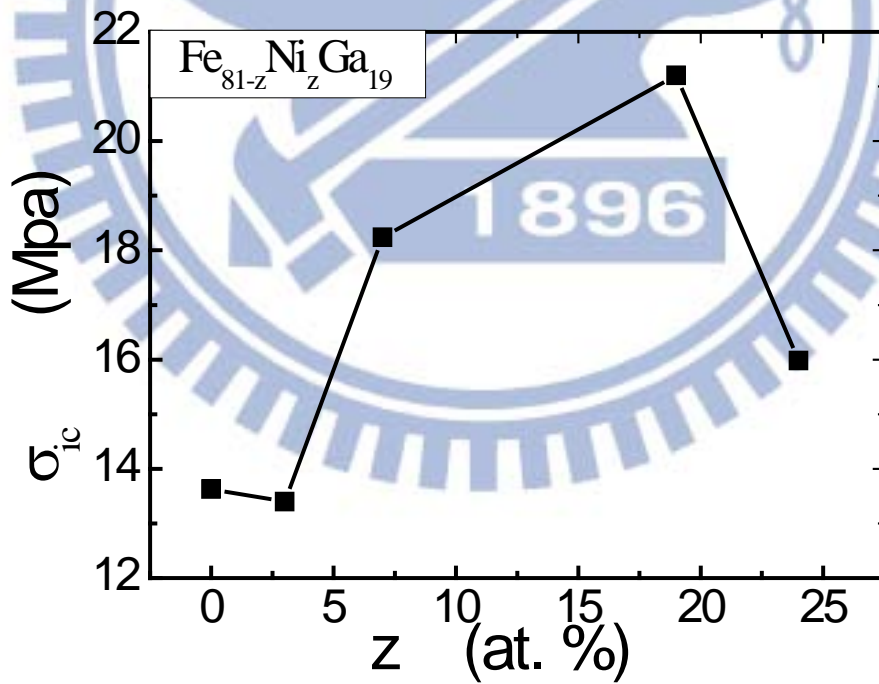

Fig. 5.9 The critical internal stress (σ_{ic}) of the melt-spun $Fe_{81-z}Ni_zGa_{19}$.

5.5 Magnetostriction data

The magnetostriction (λ) hysteresis curve of the $Fe_{81}Ni_3Ga_{19}$ ribbon, under an external weight w = 208.6 g, which means the external stress σ= 25.7 MPa, is shown in Fig. 5.10.   By applying a horizontal field H_E, up to $\pm$ 6 kOe, we tried to turn $\vec{M}_S$ toward the transverse (or $\pm$ x) directions, by 90°.   Due to the reason of stress anisotropy, we could not support enough external field to saturate λ. As expected, the λ vs. H_E plot in Fig. 5.10 is symmetric, and $\Delta\lambda$ decreases from zero to -95 ppm for the as-spun $Fe_{81}Ni_3Ga_{19}$ ribbon.

In Fig. 5.11, we still summarize all the values under the varied external weight and the same external field (6000 Oe) for the series of the melt-spun $Fe_{81-z}Ni_zGa_{19}$ ribbons.   According to Ref. 13, they found that for the rapidly quenched $Fe_{78}Ni_7Ga_{15}$ ribbon, its $\lambda < 200$ ppm under 6 kOe external field, which is roughly in agreement with our finding.   In this study, that is the largest magnetostriction in the $Fe_{74}Ni_7Ga_{19}$ ribbon.

Although we could not provide enough external field to saturate the sample, λ_s could be calculated from the ΔE effect.   This effect since the applied stress causes a deformation through the change in domain magnetization in addition to the elastic deformation.   In general, the deformation ($\Delta\varepsilon_{me}$) is caused by rotation magnetization or a displacement of 90° walls, but no deformation can be induced by 180° wall displacement.   The relation of the $\Delta\varepsilon_{me}$ and λ_s in polycrystalline can be written as[2, 3]

$$\Delta\varepsilon_{me} = \frac{3\lambda_s{}^2}{5K_u}\Delta\varepsilon_{el}. \qquad (5.4)$$

Since this gives the additional elongation,

$$\frac{3\lambda_s{}^2}{5K_u} = \frac{1}{E_0} - \frac{1}{E_s} \doteqdot \frac{\Delta E}{E_0 E_s}. \qquad (5.5)$$

where $K_u = (3/2)\,\lambda_s\sigma_{ic}$. Thus, Eq. (5.5) can be written as[22]

$$\frac{\Delta E}{E_0} = \frac{2\lambda_s E_s}{5\sigma_{ic}} \qquad (5.6)$$

By Eq. (5.6), λ_s can be calculated. The results are shown in Fig. 5.12.

There needs to be some discussion between Fig. 5.11 and 5.12. Fig. 5.11 shows the sample of the $\Delta\lambda$ which is not saturated by external field, while Fig. 5.12 shows the sample of the λ_s which was calculated from the ΔE effect. In this study, we found that the values of $|\Delta\lambda|$ in Fig. 5.11 are larger than the values of λ_s in Fig. 5.12. Since the Ni addition in $Fe_{81}Ga_{19}$ let the ribbons become more isotropic in magnetic anisotropy. When $K_u \doteqdot 0$, ΔE effect would diverge. This reason makes the ΔE effect not be ideally used to calculate λ_s. But the ΔE effect model still shows that reducing K_u is good for the magnetic material.
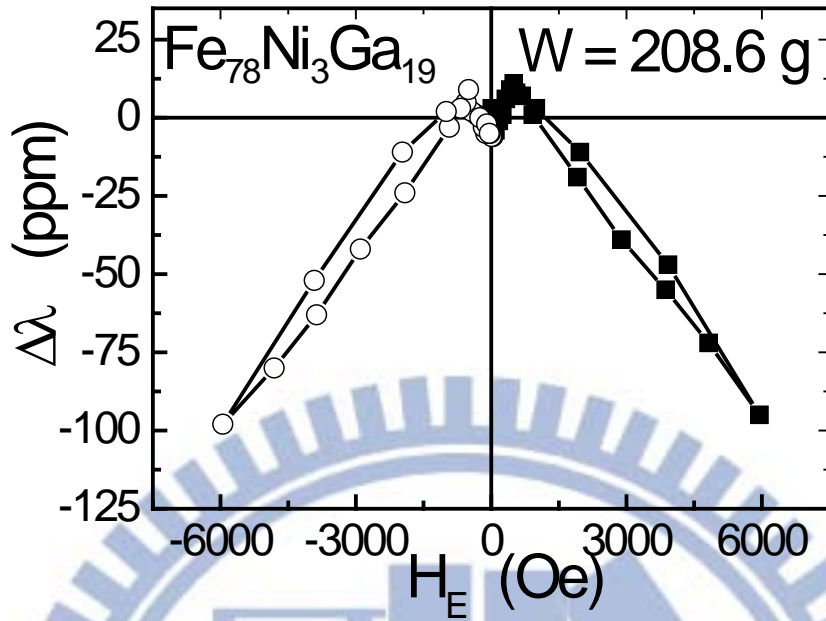
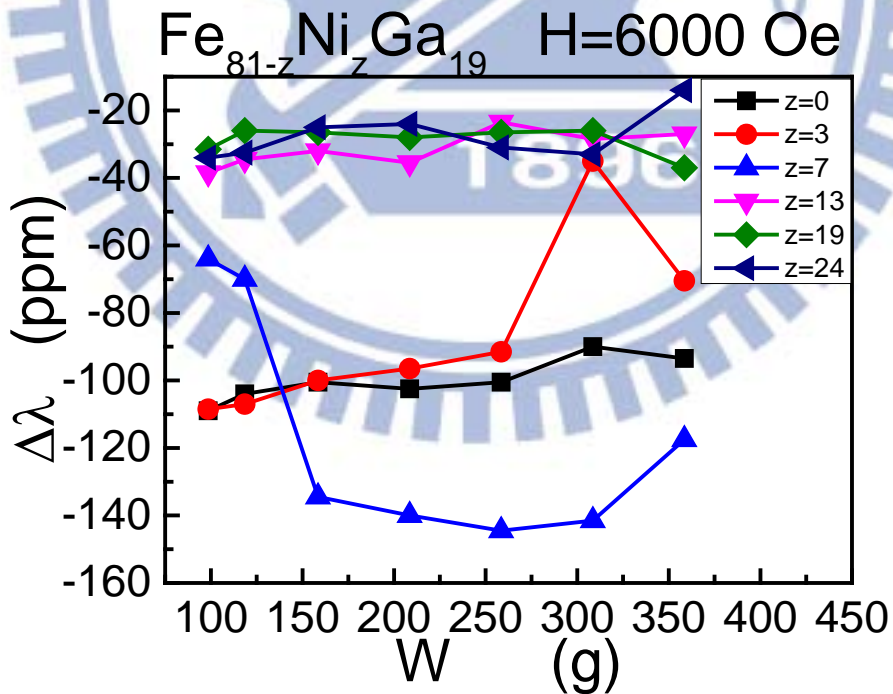Fig. 5.10 Magnetostriction of the $Fe_{81}Ni_3Ga_{19}$ ribbon plotted as a function of a horizontal in-plane field under an external weight w = 208.6 g.

Fig. 5.11 Under the 6 kOe external field, plotted the $\Delta\lambda$ VS. w for the series of the melt-spun $Fe_{81-z}Ni_zGa_{19}$ ribbons.

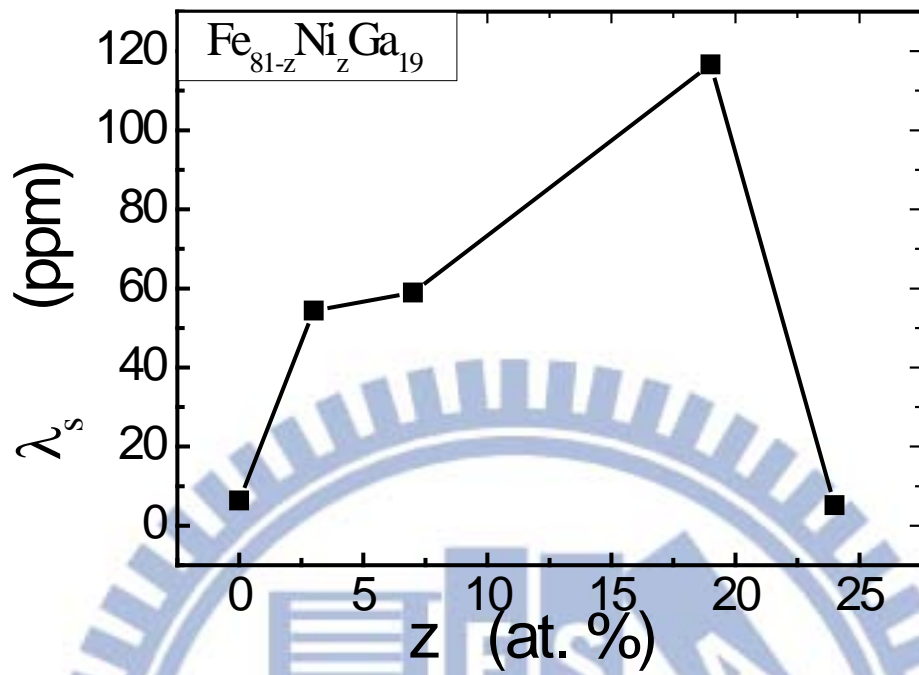Fig. 5.12 The melt-spun $Fe_{81-z}Ni_zGa_{19}$ saturation magnetostriction (λ_s) is calculated by $\Delta E/E_0$, E_s and σ_{ic}.

6 Conclusions

6.1 For Films

We have made series of $Fe_{81-x}Ni_xGa_{19}/Si(100)$ and $Fe_{81-y}Ni_yGa_{19}/glass$ films, with 0 x or y 26 at.%Ni, at room temperature by the magnetron sputtering method. Magnetic hysteresis loop, magnetostriction, and FMR measurements were performed on these films. Line width mechanisms of ΔH have been studied by many investigators. The most comprehensive channel of the dissipation of the energy from the precessing spin system is that through the eddy-currents induced by the precessing magnetization. Besides the effect of eddy currents, the hopping motion of electrons causes another route of energy dissipation, as first pointed out by Verwey[47]. Yager, Galt, and Merritt find the anisotropy forces the magnetization to rotate parallel to the direction of easy magnetization, and, for the same reason, rotation of magnetization may cause a change in the arrangement of two kinds of ions such as to rotate the easy direction toward the direction of magnetization[2, 48]. Thus the precession motion the magnetization is expected to cause a hopping of electrons, which is accompanied by loss of energy. In this study, we find the addition of Ni into $Fe_{81}Ga_{19}$ films that causes refined the magnetic anisotropy energy which let the H_K decreases, 13.8 – 6.3 Oe, as at% Ni increases. On the other hand, we observed that $(\Delta H)_{exp}$ of each film is in general asymmetric. Hence, $(\Delta H)_{exp}$ is composed of two parts: $(\Delta H)_{exp} = (\Delta H)_S + (\Delta H)_A$, where $(\Delta H)_A$ and $(\Delta H)_A$ are the symmetric and asymmetric parts. The explanation for this asymmetry is

believed to be related to the degrees of the structural and/or magnetic inhomogeneities in each film.

From Ref. 22, λ_s is 132 ppm for A2, -7 ppm for $D0_{19}$, and -32 ppm for $L1_2$, such that the $D0_{19}$ phase and $L1_2$ phase are detrimental to saturation magnetostriction. In this study, when y = 22 at.%Ni, there is only one single A2 phase, and when y =0, 4, 11, and 17 at.%Ni, there are mixed phases with A2 (major) and $D0_{19}$ and/or $L1_2$ phases (minor), λ_s reaches a maximum at x or y = 22 at.%Ni

As x or y increases, we found that [I] $4\pi M_s$ just decreases a little, 16.6 – 15.0 KG, [II] H_C is small, 34.4 – 13.8 Oe, [III] λ_s first increases and reaches a maximum at x or y = 22 at.%Ni, [IV] f_{FMR} decreases, 1.6 – 0.8 GHz, [V] μ_R increases, 1212 – 3993, and [VI] α decreases, 0.076 – 0.018. Thus, from this study we conclude that the $Fe_{59}Ni_{22}Ga_{19}$/glass film should be most suitable for the magneto-electric microwave device application.

6.2 For Ribbons

We have made a series of $Fe_{81-z}Ni_zGa_{19}$ ribbons by the rapidly quenching method. From XRD, these ribbons change the lattices constants which depend on number of z.　From VSM studies, we found that the magnetic anisotropy K_u decreases, as at%. Ni added in.　As z increases from 0 to 24 in $Fe_{81-z}Ni_zGa_{19}$, M_s decreases in general from 170 emu/g to 125 emu/g, and H_c inceases from 4.8 Oe to 11.7 Oe.　We also discovered that as z increases from 0 to 19, $\Delta E/E_0$ increases.　The most important, λ increases at z = 7 at.%Ni.

In Ref. 4 and 22, there were added B in FeGa allays, one of the purposes is reduced K_u.　This way also reduces a lot the magnetization.　The Ni addition in in FeGa allays not reduced too much magnetization, but reduced K_u.

Thus, from this study we conclude that the $Fe_{74}Ni_7Ga_{19}$ ribbon should be most suitable for the magneto-electric device application.

7. Appendix

7.1 XRD discussion

In this study, we were unable to identity all diffraction peaks.   Fig. 7.1 shows the XRD pattern of the $Fe_{81}Ga_{19}$ alloy film on Si(100) substrate.   There are too many phases in the sample; however, it appears that film samples on the glass substrate are better than these deposited on the Si substrate.   As result, our discussions were focused on film samples deposited on the glass substrate.   Fig. 7.2 shows the XRD pattern of the $Fe_{57}Ni_{24}Ga_{19}$ ribbon.   Peak I is the peak with the same 2θ angle also in the XRD patterns of the films $Fe_{70}Ni_{11}Ga_{19}$ and $Fe_{55}Ni_{26}Ga_{19}$ on glass.   But we still could not identify Peak I.

According to Ref. 49 and 50, the $Fe_{57}Ni_{24}Ga_{19}$ ribbon maybe consists of two phases, A2 and γ structure.   The tree peaks look like the tree γ peaks respective. Peak II correspondence γ(111), Peak III correspondence γ(200), and Peak II correspondence γ(220).

Another disbelieving proof is the Curie temperature which was obtained from magnetic thermal gravimetric (MTG) scan up to 900°C with a heating rate of 20°C/min.   Fig. 7.3 shows MTG result of the $Fe_{57}Ni_{24}Ga_{19}$ ribbon.   From this plot, we can identify two Curie points, T_{c1} = 463.7 ^{o}C and T_{c2}= 633.0 ^{o}C.   Ref. 51-53 reported for the Fe-Ga alloys, that T_c of A2 phase is around 650 ^{o}C, which is closed T_{c2} of the $Fe_{57}Ni_{24}Ga_{19}$ ribbon.   But the T_c of γ phase is only around 200 ^{o}C[50], which is not correspondence T_{c1}.   So we have not identified all diffraction peaks, and needs further investigation.
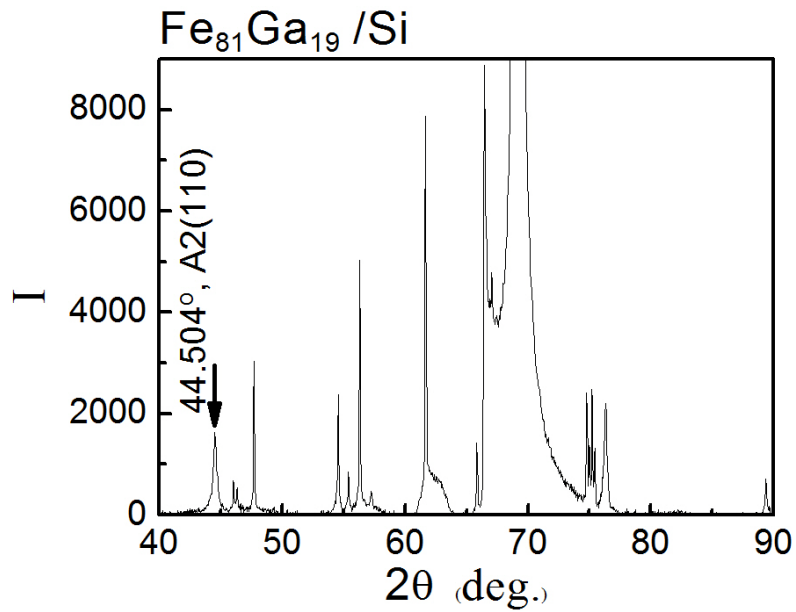
Fig. 7.1 XRD pattern of the FeGa alloy film on Si(100) substrate.
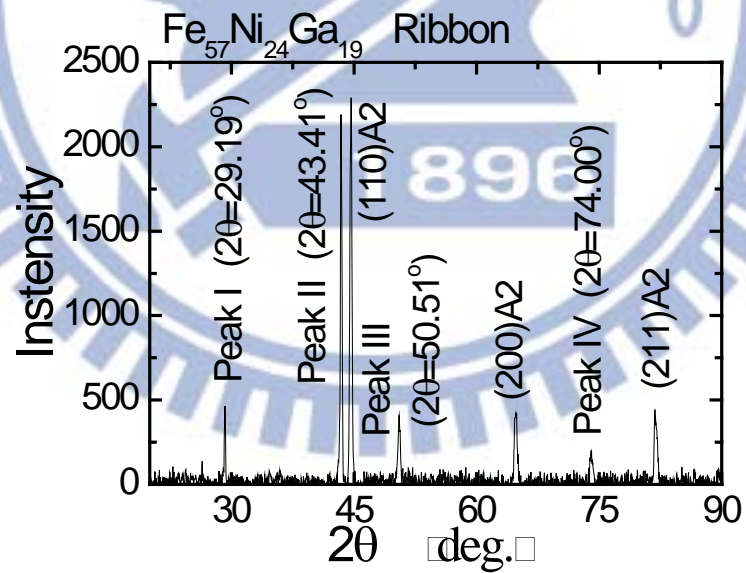
Fig. 7.2 XRD pattern of the $Fe_{57}Ni_{24}Ga_{19}$ ribbon with the quenching rate

(rotating copper wheel speed) was about 15m/s.
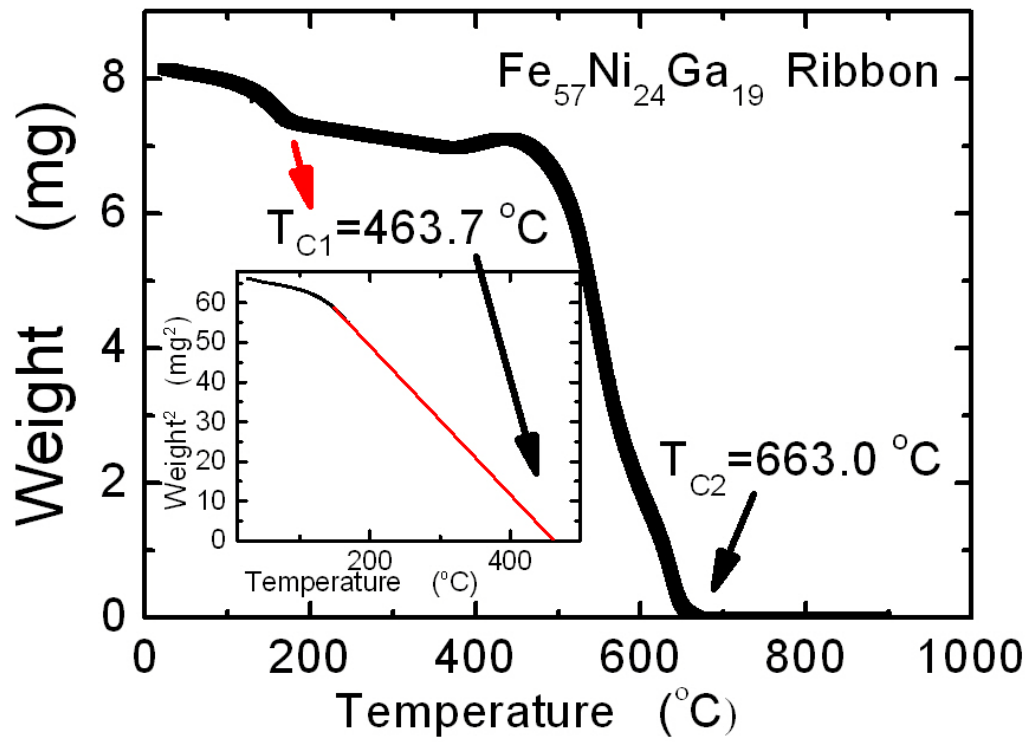
Fig. 7.3 MTG scans of the $Fe_{57}Ni_{24}Ga_{19}$ ribbon.

7.2 TEM photo for the $Fe_{70}Ni_{11}Ga_{19}$/Si(100) film

The cross-section transmission electron microscopy photo of the $Fe_{70}Ni_{11}Ga_{19}$/Si(100) film is shown in Fig. 7.4. In Fig. 7.4(a), we find that the $Fe_{70}Ni_{11}Ga_{19}$ alloys deposited on Si(100) substrate similar pillars, and the width of a pillar is quite large, about 25 nm. Fig. 7.4(b) shows the $Fe_{70}Ni_{11}Ga_{19}$ film with some nano-crystals. Fig. 7.4(c) shows the *Fourier* transform pattern, which means crystal and amorphous in this film.
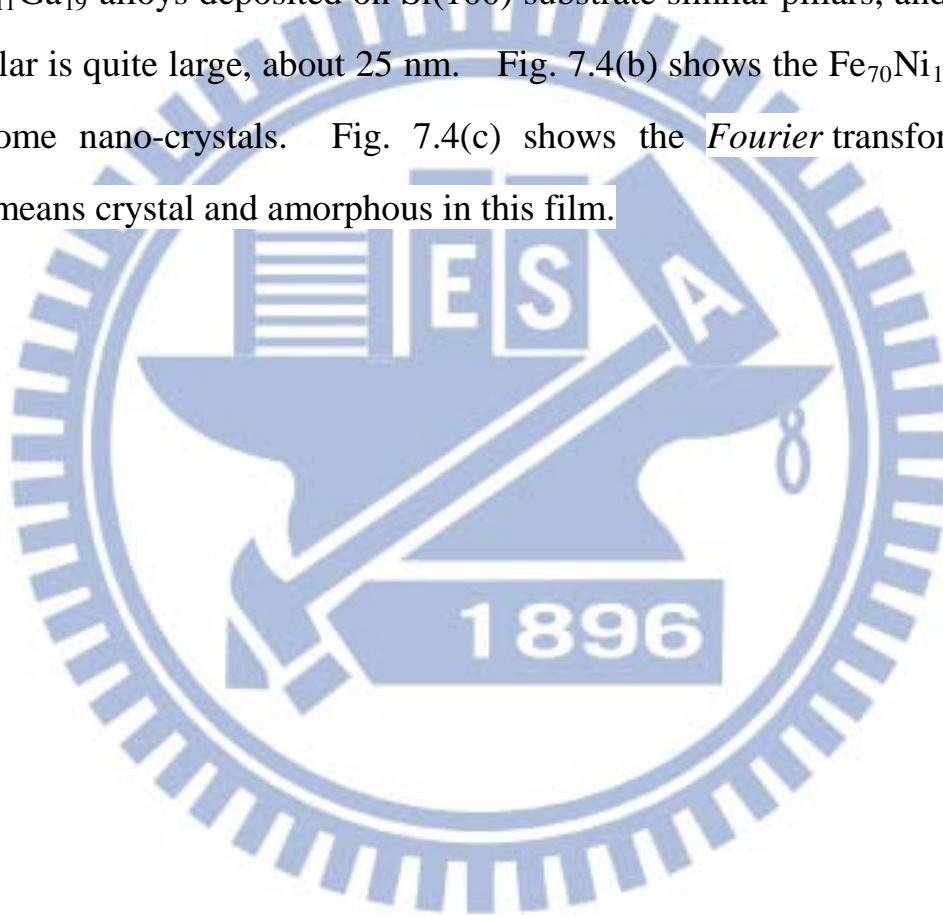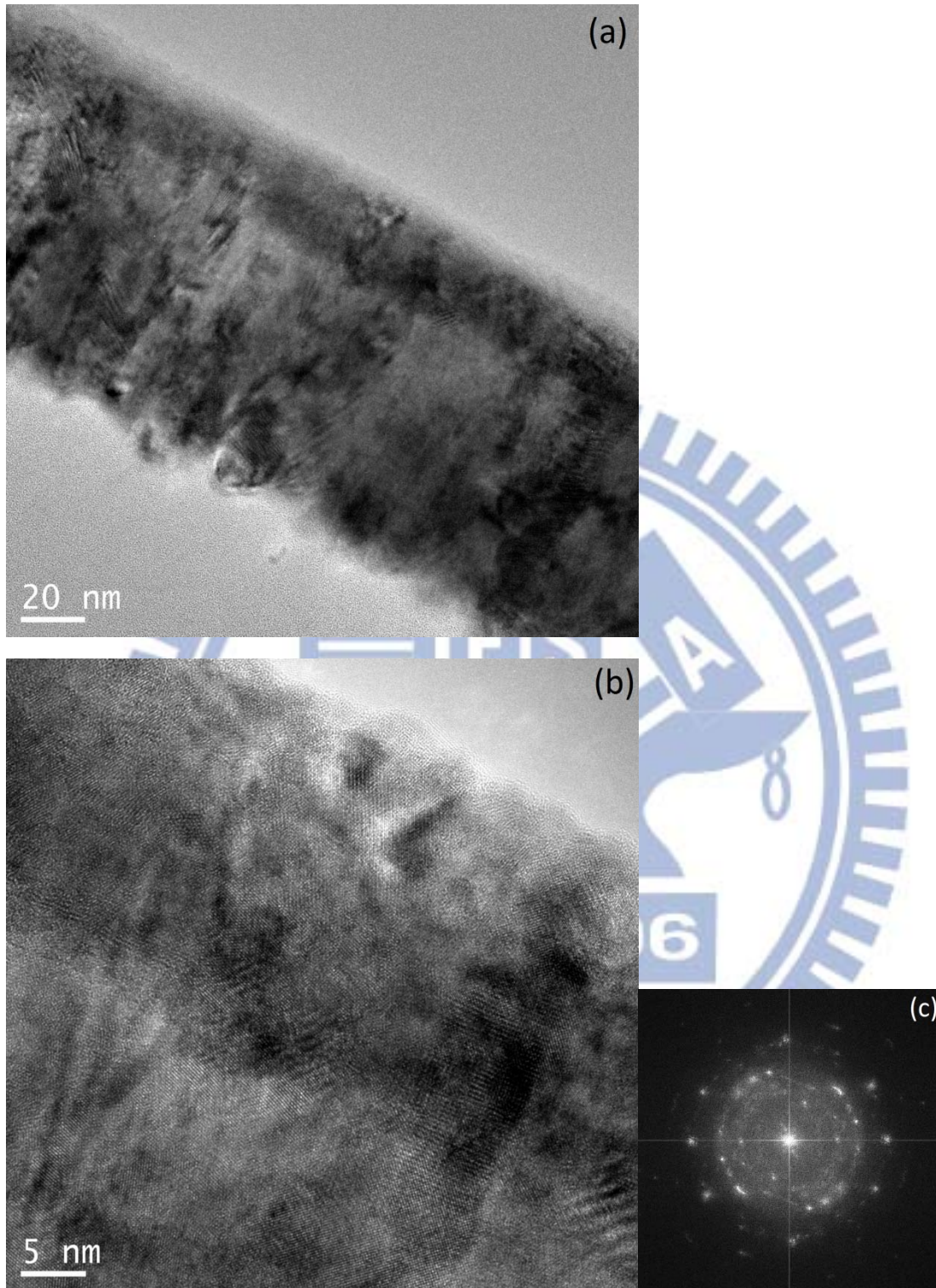
Fig. 7.4 The cross-section transmission electron microscopy photo of the $Fe_{70}Ni_{11}Ga_{19}/Si(100)$ film. (a) The $Fe_{70}Ni_{11}Ga_{19}$ alloys deposited on Si(100) substrate similar pillars. (b) This shows the polycrystal substrate. (c) Shows the *Fourier* transform pattern.

7.3 σ vs. Δε of the $Fe_{68}Ni_{13}Ga_{19}$ ribbon

We could not obtain reasonable E_s, ΔE and σ_{ic} in the Fig. 7.5.   The strain (Δε) are to small too let the E_s unreasonable larger than 900 MPa.
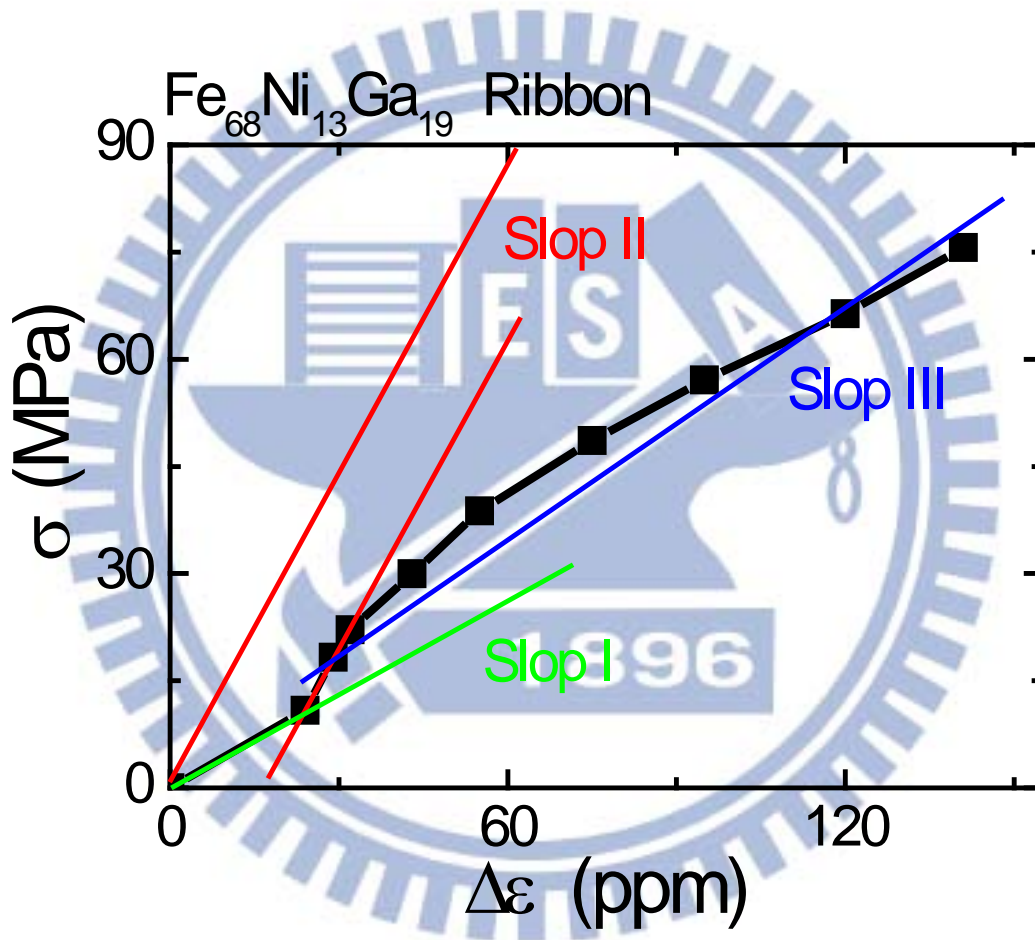
Fig. 7.5 The stress (σ) vs. strain (Δε) curves of the as-spun $Fe_{68}Ni_{13}Ga_{19}$ ribbon.

Reference:

[1] R. Boll, <u>Soft Magnetic Materials</u>, Heyden & Son, Hanau, 1979.

[2] S. Chikazumi, <u>Physics of Magnetism</u>, Krieger, New York, 1978.

[3] B. D. Cullity and C. D. Graham, <u>Introduction to Magnetic Materials</u>, John Wiley & Sons, New York, 2009.

[4] J. Lou, R. E. Insignares, Z. Cai, K. S. Ziemer, M. Liu, N. X. Sun, <u>Appl. Phys. Lett.</u>, 91, pp. 182504, 2007.

[5] A. E. Clark, J. B. Restorff, M. Wun-Fogle, T. A. Lograsso, D. L. Schlagel, <u>IEEE Trans. Mang.</u>, 36, pp. 3238, 2000.

[6] S. U. Jen, T. L. Tsai, <u>J. Appl. Phys.</u>, 111, pp. 07A939, 2012.

[7] A. E. Clark, M. Wun-Fogle, J. B. Restorff, and T. A. Lograsso, <u>Mater. Trans., JIM</u>, 43, pp. 881, 2002 .

[8] N. Srisukhumbowornchai, S. Guruswamy, <u>J. Appl. Phys.</u>, 9, pp. 5680, 2001.

[9] A. Butera, J. Gómez, J. L. Weston, J. A. Barnard, <u>J. Appl. Phys.</u>, 98, pp. 033901, 2005.

[10] Y. Gong, C. Jiang, H. Xu, <u>Acta Metall. Sin.</u>, 42, pp. 830, 2006.

[11] T. Kubota, A. Inoue, <u>Mater. Trans.</u>, 45, pp. 199, 2004.

[12] K. Fukamichi, T. Satoh, T. Masumoto, <u>J. Magn. Magn. Mater.</u>, 1589, pp. 31–34, 1983.

[13] C. Bormio-Nunes, R. Sato Turtelli, R. Grossinger , H. Muller, H. Sassik, <u>J. Magn. Magn. Mater.</u>, 322, pp. 1605, 2010.

[14] C. Bormio-Nunes, R. Sato Turtelli, H. Mueller, R. Grossinger, H. Sassik, M.A. Tirelli <u>J. Magn. Magn. Mater.</u>, 820, pp. 290–291, 2005.

[15] J. B. Restorf, M. Wun-Fogle, A.E. Clark, T.A. Lograsso, A.R. Ross, D.L. Schlagel, J. Appl. Phys. 91, pp.8225, 2002.

[16] A. H. Morrish, The Physical Principles of Magnetism, John Wiley & Sons, New York 1965.

[17] D. K. Cheng, Field and Wave Electromagnetics, Addison Wesley, New York 1989.

[18] S. U. Jen, T. L. Tsai, and C. C. Liu, J. Appl. Phys., 106, pp. 013901, 2009.

[19] 金原粲，薄膜製做工藝學，賴耿陽，復漢出版社，1990。

[20] 李正中，薄膜光學與鍍膜技術，藝軒圖書出版社，2002。

[21] Russell J. Hill, Physical Vapor Deposition, Temescal, 1986.

[22] S. U. Jen, S. P. Wang, W. C. Chang, and H. W. Chang, J. Appl. Phys., 112, pp. 053904, 2012.

[23] Dektak[3] user's manual, Sloan Technology, 1991.

[24] S. U. Jen and T. C. Wu, Thin Solid Films, 492, pp. 166, 2005.

[25] A. C. Fischer-Cripps, Nanoindentation, Springer, New York, 2002

[26] Charles Kittel, Introduction to Solid State Physics, 8th Edition, John Wiley & Sons, New York 2005.

[27] Shien-Uang Jen, Chi-Ching Liu, Jenh-Yih Juamg, Adv. Mater. Res., 705, pp. 66, 2013.

[28] H. H. Wieder, Laboratory Notes on Electrical and Galvano-Magnetic Measurements, Elsevier, New York, 1979.

[29] Liu, Chi-Ching, Jen, Shien-Uang, Juang, Jenh-Yih, Lo, Chi-Kuen, J. Alloys Compd., 562, pp. 111, 2013.

[30] 陳元宗,「銥錳交換耦合之(鈷鐵硼/氧化鋁/鈷)磁穿隧元件的機械性質,電性及磁性研究」,國立清華大學,博士論文,2006.

[31] S. Middelhoek, <u>Ferromagnetic Domains in Thin Ni–Fe Films</u>, Drukkerij Wed. G. Van Soest N.V, Amsterdam 1961.

[32] S. U. Jen and C. C. Lin, <u>Thin Solid Films,</u> 471, pp. 218, 2005.

[33] E. Du Trémolet de Lacheisserie, and J. C. Peuzin, <u>J. Magn. Magn. Mater.,</u> 136, pp. 189, 1994.

[34] C. Bormio-Nunes, C. T. dos Santos, I. F. Leandro, R. S. Turtelli, R. Grössinger, and M. Atif, <u>J. Appl. Phys.</u>, **109**, pp. 07A934, 2011.

[35] R. Grossinger, R. S. Turtelli, N. Mehmood, S. Heiss, H. Muller, and C. Bormio-Nunes, <u>J. Magn. Magn. Mater.</u>, 320, pp. 2457, 2008.

[36] T. Saito and K. Sudo, <u>J. Appl. Phys.</u>, **109**, pp. 07A925, 2011.

[37] S. F. Cheng, B. N. Das, M. Wun-Fogle, P. Lubitz, and A. E. Clark, <u>IEEE Trans. Magn.</u>, 38, pp. 2838, 2002.

[38] R. M. Bozorth, <u>Ferromagnetism</u>, IEEE, New York 1993.

[39] S. U. Jen, T. Y. Chou, C. K. Lo, <u>Nanoscale Res. Lett.</u>, 6, pp. 468-473, 2011.

[40] J. S. Liao, Z. K. Feng, J. Qiu, Y. Q. Tong, <u>Acta Metall. Sin.</u>, 21, pp. 419-424, 2008.

[41] S. V. Vonsovskii, <u>Ferromagnetic Resonance</u>, Pergamon Press, Oxford, 1966.

[42] S. U. Jen, T. L. Tsai, M. S. Li, P. C. Kuo, and M. Y. Lin, <u>J. Appl. Phys.</u>, 109, pp. 07A920, 2011.

[43] T. A. Lograsso, A. R. Ross, D. L. Schlagel, A. E. Clark, and M. WunFogle,<u>J. Alloys Compd.</u>, 350, pp. 95, 2003.

[44] C. Kittel, <u>Introduction to Solid State Physics</u>, 8th Edition, John Wiley & Sons, 2005

[45] B. D. Cullity, Elements of X-Ray diffraction, John Wiley & Sons, New York, 1956.

[46] Klein, C. and C. S. Hurlburt Jr., Manual of Mineralogy, 20th edition, John Wiley & Sons, 1985.

[47] E. J. W. Verwey, Nature, 144, pp. 327, 1939.

[48] W. A. Yager, J. K. Galt, and F. R. Merritt, Phys. Rev., 99, pp. 1203, 1955.

[49] N. V. Rama Rao, R. Gopalan, M. Manivel Raja, V. Chandrasekaran, and K. G. Suresh, Appl. Phys. Lett., 93, pp. 202503, 2008.

[50] R. Ducher, R. Kainuma, K. Ishida, J. Alloys Compd., 463, pp. 213, 2008.

[51] T. Saito and K. Sudo, J. Appl. phys., 109, pp. 07A925, 2011.

[52] O. Ikeda, R. Kainuma, I. Ohnuma, K. Fukamichi, K. Ishida, J. Alloys Compd., 347, pp. 198, 2002.

[53] N. Kawamiya, K. Adachi, and Y. Nakamura, J. Phys. Soc. Jpn., 33, 1318, 1972.

Biographical Notes

Chi-Ching Liu（劉奇青）

Sex : Male
Date of Birth : September 23, 1982

E-mail: ccliu@phys.sinica.edu.tw

Education:

2001- 2005:	B. Sc., Physics, Fu Jen Catholic University
2005- 2008:	M. Sc., Institute of Optoelectronic Sciences, National Taiwan Ocean University
2010-2013:	Ph. D., Dept. of Electrophysics, National Chiao Tung Univ.

Research interests:

Magnetostriction and application; Magnetic domains and domain walls;
Ferromagnetic resonance

Selected Publications:

1. Magnetic properties of Fe-rich Fe-V alloy films

   (*Journal of Applied Physics 106, (2009) 013901)*

2. Effects of Substrate Temperature on Magnetostriction of $Fe_{62}Co_{19}Ga_{19}$/Si(100) Films

   (ICCE-20 Conference)

3. Ferromagnetic resonance properties of $Fe_{81-x}Ni_xGa_{19}$/Si(100) and $Fe_{81-y}Ni_yGa_{19}$/glass

   films   (Journal of Alloys and Compounds 562, 111 (2013))

4. Magneto-elastic and mechanical properties of Fe81-xNixGa$_{19}$/Si(100) and

   $Fe_{81-y}Ni_yGa_{19}$/glass films   (MEMSM 2013 Conference)

5. Magnetic domain studies of $La_{0.7}Sr_{0.3}$MnO3 film deposited on $SrLaAlO_3$(001) substrate

   (J. Phys. D: Appl. Phys., 46, (May 2013), 255001)